Technische Universität München

Fakultät für Elektrotechnik und Informationstechnik

Lehrstuhl für Biologische Bildgebung

Development of Real-Time Hybrid Focus Optoacoustic Microscopy for Multi-Scale Imaging in Scattering Tissues

Jake Berry Turner

Vollständiger Abdruck der von der Fakultät für Elektrotechnik und Informationstechnik der Technischen Universität München zur Erlangung des akademischen Grades eines

Doktor-Ingenieurs (Dr.-Ing.)

genehmigten Dissertation.

Vorsitzender:	Prof.-Ing. Dr. Bernhard U. Seeber
Prüfer der Dissertation:	1. Prof. Dr. Vasilis Ntziachristos
	2. Prof. Dr.-Ing. Erwin Biebl

Die Dissertation wurde am 09.02.2017 bei der Technischen Universität München eingereicht und durch die Fakultät für Elektrotechnik und Informationstechnik am 18.08.2017 angenommen.

Contents

1 Background & Theory **1**
- 1.1 Optical Imaging 1
- 1.2 Ultrasonography 2
- 1.3 Optoacoustics 8

I Microscope System Development
Development of a Real-Time Optical- and Acoustic-Resolution Optoacoustic and Ultrasound Microscopy System **11**

2 Background **13**

3 Raster Scanning System **15**
- 3.1 System Overview 15
- 3.2 Ultrasound Transducers 19
- 3.3 Optical Fibre 23
- 3.4 Control of the system and operation 26
- 3.5 Experimentation 27
- 3.6 Discussions 31

4 Fast Scanning System **33**
- 4.1 System Overview 33
- 4.2 Power Limitation and Spatial averaging 37
- 4.3 Amplitude Criterion and Fibre-Motion artefact correction . . 38
- 4.4 Experimentation 40
- 4.5 Discussion 42

5 Pulse Echo Ultrasound Microscopy **43**
- 5.1 Motivation 43
- 5.2 Ultrasound Generation and Acquisition 44
- 5.3 Dual-Mode Acquisition 45
- 5.4 Hybrid PE-OAM 45
- 5.5 Experimentation 47
- 5.6 Discussion 50

II Effects of acoustic mismatches of the skull
The challenges of imaging through intact mouse skull and approaches to correction for its presence. **53**

6 Acoustic Effects of Murine Skull 55
6.1 Introduction . . . 55
6.2 Experimentation . . . 55
6.3 Results . . . 57
6.4 Discussion and Conclusions . . . 62

7 Broadband Acoustic Properties of a Murine Skull 63
7.1 Introduction . . . 63
7.2 Theory . . . 65
  7.2.1 Transmission through a fluid-loaded solid layer . . . 65
  7.2.2 The angular spectrum method . . . 67
7.3 Materials and methods . . . 68
  7.3.1 Experimental Setup . . . 68
  7.3.2 Numerical calculations . . . 69
7.4 Results . . . 69
  7.4.1 Glass plate measurements . . . 69
  7.4.2 Mouse skull measurements . . . 71
7.5 Discussion . . . 73
7.6 Conclusion . . . 76

III Algorithms for synthetic aperture focusing in scanning microscopy
Improving Ultrasound Images from a Hybrid-Focus Optoacoustic and Ultrasonic Microscope **77**

8 Background 79

9 SIR-SAFT 81
9.1 Introduction . . . 81
9.2 Theory . . . 81
9.3 Methods . . . 83
9.4 Results . . . 83
9.5 Discussion & Conclusion . . . 87

10 WSAFT 89
10.1 Introduction . . . 90
10.2 Theory . . . 91
  10.2.1 Background . . . 91
  10.2.2 The W-SAFT Algorithm . . . 93
10.3 Methods . . . 97

- 10.3.1 Simulated Scan 97
- 10.3.2 Phantom Scan 98
- 10.3.3 Biological Scan 99
- 10.4 Results 99
  - 10.4.1 Numerical Simulations 99
  - 10.4.2 Phantom Scan 100
  - 10.4.3 Zebrafish Imaging 101
- 10.5 Discussion 102
- 10.6 Conclusions 105

IV Discussions and Future Directions
Developments Towards High-Resolution Optoacoustic In-Vivo Neuroimaging at Depth **107**

11 Future Work 109
- 11.1 Illumination 109
- 11.2 Skull Correction 110
- 11.3 W-SAFT 110

Appendices 115

A List of Publications 117

Chapter 1

Background & Theory

Neuroimaging is a vital tool in understanding biological processes within the brain. From endeavouring to understand in greater detail the workings therein, to observing and developing treatments for disease, current abilities to see into the brain are indispensable. As such, the motivation for the push to achieve greater resolution at greater depths is readily understandable. Furthermore, the development of functional imaging techniques that provide dynamic contrast for said biological processes is a rapidly advancing field of biomedical imaging. Experimental and clinical biomedical imaging today encompasses many different modalities, each with their own strengths and caveats. Optoacoustics is a developing field which shares both the benefits of being non-ionising, comparatively low-cost, and portable. In Chapter 1 of this thesis the necessary theoretical and historical background is presented.

1.1 Optical Imaging

Optical imaging is perhaps the most familiar imaging modality there is. The process of making images with conventional cameras is simple, cheap, and fast. When considering the application within biomedical imaging, the strengths of optical imaging are the very high resolution images which are achievable, and it's non-ionising nature. However, the major challenge is not resolution, but rather the scattering-limited penetration depth.

In conventional compound microscopy the imaging target is broadly illuminated with a bright light source, and images are acquired through a focusing objective. The lateral resolution achievable by such a system is dictated by the diffraction limit, d, which is defined as

$$d = \frac{\lambda}{2\mathrm{NA}}, \tag{1.1}$$

where λ is the wavelength of the illumination light, and NA is the numerical aperture of the objective. Commonly d is of an order of around 200 nm, though this can be reduced through careful wavelength selection and using oil as an objective-coupling media. Although this lateral resolution is very high, the depth-penetration capabilities of compound microscopy in scattering media is limited to the order of around 10 μm. To overcome the depth-limitations in microscopy, confocal and laser scanning confocal microscopy (LSCM) were developed. Here, instead of broad illumination, a spot is focused on the surface, or at a certain depth within, the target media. A pin-hole at the confocal point of the objective blocks incident light from elsewhere than the focal plane inside the imaging target, effectively spatially gating the target into a specific depth plane. In LCSM, the illumination point is a laser generated spot, which is iteratively moved voxel-wise through the target volume. Using the confocal technique images can effectively be made at depths up to around 100-500 μm. Commonly these techniques are implemented in fluorescence imaging for biological targets, where the illumination light of a specific wavelength will cause certain fluorophores to emit light of a different wavelength. This mechanism works by the electrons of a fluorophore being excited to a higher energy state upon absorption of the incident photon; this energy state is unstable, and when the electron drops back to the lower energy state, a photon of a different wavelength is emitted. Two-photon microscopy can achieve greater penetration depths still in the case of fluorescence imaging by altering the excitation illumination delivery. Here, instead of the electrons increasing their energy state as the result of a single absorption event of a higher energy photon of wavelength λ_i, 2 photons of wavelength $2\lambda_i$ are absorbed i.e. the illumination is red shifted and less scattered, thus permitting higher resolution and greater penetration depths. Using two-photon microscopy, imaging depths of up to 1 mm are achievable.

Systems achieving sub diffraction-limited resolution (super resolution) have also been developed in recent years. One noteworthy example being the fluorescence-based microscopy technique STimulated Emission Depletion (STED), which uses an annular illumination spot to deactivate fluorophores around a point [1], thus allowing very accurate localisation in the order or 1nm.

1.2 Ultrasonography

One modality commonplace in hospitals and clinics throughout the world is ultrasound imaging. This is due to it's low cost, robust nature, excellent depth penetration and largely absent risk in application. Two examples of commonplace use of ultrasonography are when checking for birth defects in prenatal imaging, and for the presence of cancer in breast imaging. Typically ultrasonography operates within a frequency range of between 1-20 MHz, and the frequency used is selected as a compromise between higher spatial resolution (higher frequencies) or greater depth penetration (lower frequencies), with typical limits of around 10 μm and 50 cm, respectively. This compromise is necessary due to the nature of acoustic propagation through the object being imaged.

In ultrasonography the majority of imaging is performed using pulse-echo based systems. This sees a transducer send an acoustic wave into a target media, and then detect the reflected portion of that wave from boundaries of impedance change. The equation for a plane wave propagating through a three-dimensional homogeneous media is given by

$$p_0(\mathbf{r}, t) = Ae^{i(k\mathbf{r}-\omega t+\phi)}, \tag{1.2}$$

where $\mathbf{r} = x\hat{\mathbf{x}} + y\hat{\mathbf{y}} + z\hat{\mathbf{z}}$ is a distance, t is time, A is a constant amplitude gain, $k = 2\pi/\lambda$ is the wavenumber (λ is the wavelength), w is the frequency and ϕ is a phase-gain term.

Consider a plane-wave p_0 in a media with an acoustic impedance $Z = \rho c$ incident on a media with a different acoustic impedance $Z' = \rho' c'$, where ρ is the density and c is the speed of sound. This wave will be partially reflected and transmitted, with both results constrained by energy conservation. The three waves present within the system of a single interface can be written as

$$p_0(\mathbf{r}, t) = p_T(\mathbf{r}, t) + p_R(\mathbf{r}, t), \tag{1.3}$$

where p_T and p_R are the transmitted and reflected acoustic waves, respectively. For a plane-wave incident at some angle θ to the normal the reflection and transmission coefficients $R(\theta)$ and $T(\theta)$ are given as

$$\begin{aligned} R(\theta) &= \frac{\cos\theta Z' - \cos\theta' Z}{\cos\theta Z' + \cos\theta' Z} \\ T(\theta) &= \frac{2Z'\cos\theta}{\cos\theta Z' + \cos\theta' Z}. \end{aligned} \tag{1.4}$$

The transmitted wave will continue to propagate in the direction of the incident wave and can be given as

$$p_T(\mathbf{r}, t) = T(\theta)Ae^{i(k\mathbf{r}-\omega t+\phi)}, \tag{1.5}$$

whereas the reflected wave will propagate in the opposite directions to the incident wave as $\mathbf{r} < 0$

$$p_R(\mathbf{r}, t) = R(\theta)Ae^{i(k\mathbf{r}-\omega t+\phi)}. \tag{1.6}$$

The depth at which the incident wave p_0 is able to reach is dictated by the extent to which it is absorbed, with the absorption coefficient α given as

$$\alpha = 1 - R. \tag{1.7}$$

In addition to impedance based reflections the propagation of acoustic waves in homogeneous media is effected by frequency dependant attenuation $\alpha(\omega)$. This attenuation is often expressed as a power-law of the form

$$\alpha(\omega) = \alpha_0 \omega^{\eta}, \tag{1.8}$$

where some pre-factor α_0 is the absorption at a known frequency ω from which the absorption at any frequency $\alpha(\omega)$ can be calculated once the exponential loss term η is known; this term is often an empirical value.

In reality the object being imaged is typically inhomogeneous, and the physics of propagation are somewhat more complicated. Firstly, although thus far only a single interface was used, it's a simple extension to consider the second media is of some thickness and has been inserted into the first media. In this heterogeneous scenario consider a normally incident plane wave and that it will transmit some energy as a plane wave into the second media. This transmitted wave can then be considered the incident wave on the second interface, which will both transmit some portion of itself back into the first media, with the rest being reflected. This process will reoccur, albeit in a spatially mirrored fashion, when the newly reflected wave is incident on the first boundary. Overall, this process will repeat until the energy of the wave has either been absorbed or propagated from the model. If this system was using a single pulse-echo transducer then the detected signals would be the initial reflection from the first interface, followed by the waves transmitted from the reflections within the second media. This is illustrated in Figure 1.1, where at t_0 a plane wave p_0 is incident on the left-most interface of a region with a different speed of sound, c_1. At the next time interval, t_1, the initial p_0 has split into a transmitted portion, p_1, and a reflected portion, p_2, as per (1.3). Similarly, at t_2 wave p_1 has split into p_3 and p_4, at t_3 wave p_4 has split into p_5 and p_6, and at t_4 wave p_5 has spilt into p_7 and p_8. It can readily be seen that an observer on the right-hand side of the inserted media would be able to detect both p_3 and p_7. Conversely, if p_0 was from a pulse-echo system said system would detect p_2 and p_6.

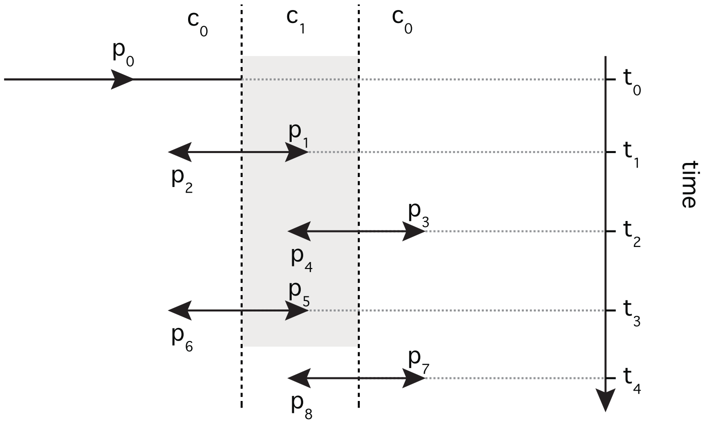

Figure 1.1: Illustration of an incident wave, p_0 on a finite-width region with a different acoustic impedance. The five interface interactions are illustrated at time points t_0-t_4.

Secondly, consider a similar system except in two dimensions, x and y, and where the rectangular impedance mismatch has been replaced by a circle of radius significantly larger than the wavelength of the incident wave. Here the scattering is within the geometric scattering regime i.e. the propagation of the scattered acoustic waves is described by an extension of the previously presented equations to account for the curvature of the surface. This concept is illustrated in Figure 1.2. The case where the wavelength is much larger than the scattering object is described by Rayleigh scattering. In this scenario the incident wave passes the object largely unaffected, though the object itself will act as a radiative acoustic source. If the object has a bulk modulus less than that of the surrounding media it will radiate as a monopole; if the bulk modulus is greater than the surrounding media the monopole is phase reversed. In the case that the density of the inhomogeneity is much greater than the surrounding media it will radiate as a dipole; again the reverse scenario gives a phase inversion. Thorough derivations for this can be found in [2].

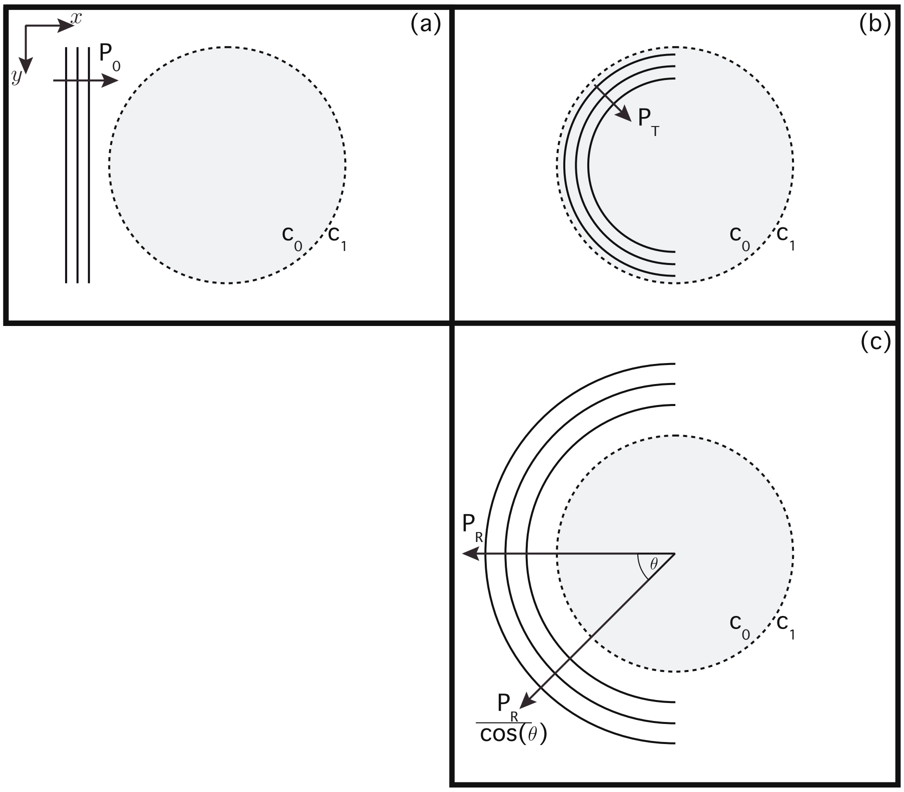
(a)
x
y
P_0
c_0
c_1
(b)
P_T
c_0
c_1
(c)
P_R
θ
c_0
c_1
$\frac{P_R}{\cos(\theta)}$

Figure 1.2: A qualitative illustration of (a) a plane wave incident on a circular speed of sound inhomogeneity and the resultant (b) transmission and (c) reflection.

Unfocused single-element ultrasound transducers are one of the simplest methods of ultrasound detection. Considering an incident plane-wave p_0 upon such an unfocused detector, then the signal recorded $p_m(t)$ will be a convolution of the acoustic wave and the electrical impulse response (EIR) $h(t)$ of the transducer

$$p_m(t) = p_0(t) * h(t). \tag{1.9}$$

This time-domain convolution is more readily interpretable as a frequency-domain multiplication i.e. as a colouring of the frequency content of p_0 by the properties of the transducer. If the EIR of the transducer is known, then analytically it is possible to remove this coloration through a deconvolution. As time-domain deconvolution is a non-trivial computational operation it is common to instead take both the recorded signal and the EIR to the frequency domain, perform a division to give an estimate of the real acoustic wave, then take that result back to the time domain

$$P_0(f) = \frac{P_m(f)}{H(f)}. \tag{1.10}$$

However, in the presence of system noise and imperfect data discretisation, the result of any deconvolution approach is an estimate of the real signal

$$\begin{aligned} p_m(t) &= p_0(t) * h(t) + \epsilon_n, \\ P_0(f) &= \frac{P_m(f) + E_n}{H(f)}, \\ p_{est}(t) &= \mathcal{F}^{-1}\Big[P_0(f)\Big] \simeq \mathcal{F}^-1\left[\frac{P_m(f)}{H(f)}\right], \end{aligned} \tag{1.11}$$

where ϵ_n is the noise added to the signal during acquisition.

In conventional ultrasonics the EIR is typically determined one of two ways. The first option is to excite the transducer with a signal that approximates a Dirac delta and to then measure the emitted ultrasound wave with a previously characterised transducer. The second is to excite the detector in the same manner, but to detect the emitted ultrasound wave with the same transducer after it has been reflected from a highly efficient reflective surface. The first method is more useful if the effects of the EIR on the emitted wave are of interest, and the latter is of greater use in pulse-echo applications due to, effectively, a double convolution. In optoacoustics it has, however, been shown that as the transducer is passive and any detected source is effectively only convolved with the receive-mode EIR then an alternative method need be employed. In this method, an optoacoustic source is excited that will generate a dominant frequency significantly above the centre frequency of the transducer, thus relatively approximating a Dirac delta [3]. The main methods of performing this measurement are presented in Part I.

Focused ultrasound detectors are commonly used where a high imaging resolution is necessary. This is because at the focus they are capable of resolving very small acoustic-scatterers or acoustic-sources in pulse-echo and passive operation, respectively. There exist several ways to achieve this focusing, such as through multi-element delay-based methods. In this method many transducer elements are either positioned discretely on a curved surface so as any in-focus incident acoustic wave arrives simultaneously across all the elements, or by applying appropriate delays to a flat element array so as to simulate geometrical focusing. The later of these two approaches has the advantage that the focus can be steered to wherever it is desired, whereas physical focusing is more constrained. Where many-element arrays are not practicable, single element focused detectors are often employed. The lateral -3dB (half-energy) contour of a geometrical spherically focused single element detector is approximated as

$$B_{3\mathrm{dB}} \simeq \lambda \frac{f_d}{D}, \tag{1.12}$$

where D is outer-diameter, λ is wavelength and f_d is focal-length [4]. Similarly to the focused arrays, these can be constructed in two ways. Firstly, either a detection geometry can be machined and an active surface overlaid. Secondly, a flat-faced active element is focused via an interstitial acoustic lens i.e. some matching-layer which defocuses the incident acoustic wave onto the element surface. The main drawback in the use of lensed transducers is the inherent signal-ringing of detected acoustic waves.

1.3 Optoacoustics

As mentioned previsouly the main advantage of optical imaging is the very high resolution that can be achieved, with the drawback of limited depth penetration and potentially only fluorescence imaging. Conversely, ultrasonography can reach incredible depths, though is incapable of the resolution achievable with optical imaging. Additionally, ultrasonography is only capable of detected changes of acoustic impedance. Optoacoustics, also referred to as photoacoustics, aims to combine the benefits of these two technologies through use of the optoacoustic effect. The optoacoustic effect is where an optically absorbing body is irradiated with a very short (ns) laser pulse, and the thermoelastic expansion and contraction of the body as a result of this irradiation generates an acoustic wave in the surrounding media.

The optoacoustic generation of acoustic pressure waves is give by [5] as

$$\frac{\partial^2 p(\boldsymbol{r},t)}{\partial t^2} - c^2 \rho \nabla \cdot \left(\frac{1}{\rho} \nabla p(\boldsymbol{r},t) \right) = \Gamma \frac{\partial H(\boldsymbol{r},t)}{\partial t} \tag{1.13}$$

where c is speed of sound, ρ is density of the media, Γ is the Grüneisen parameter, H is the energy absorbed per unit volume per unit time, t; and, $\boldsymbol{r}$ is a 3D position vector. For homogeneous media, this simplifies to

$$\frac{\partial^2 p(\boldsymbol{r},t)}{\partial t^2} - c^2\nabla^2 p(\boldsymbol{r},t) = \Gamma H_r(\boldsymbol{r})\frac{\partial H_t(t)}{\partial t}. \tag{1.14}$$

The Grüneisen parameter is a variable of the thermoelastic expandability of the volume, defined by [6] as

$$\Gamma = \frac{\beta}{\kappa\rho C_v}, \tag{1.15}$$

where β is thermal coefficient of expansion, κ isothermal compressibility and C_V is the specific heat capacity at constant volume.

One of the greatest strengths of optoacoustics is the intrinsic contrast it can achieve in biological targets. Similarly to fluorescence imaging optoacoustics uses single-wavelength laser light for illumination. However, it is independent on the presence on fluorophores. Instead, the illumination wavelength used needs only to match the wavelength of a peak in the absorption spectra of the desired compound to be imaged. For example, in the near infra-red wavelength range (700-900nm), where depth penetration is greater, deoxygenated haemoglobin (Hb) is dominantly absorptive towards 700nm, whereas oxygenated haemoglobin (HbO_2) is dominantly absorptive towards 900nm. Therefore two scans made at 700nm and 900nm of a vascularised region of an in-vivo imaging target can be combined to give a cumulative insight into oxygenation in the vasculature. Overall, combining the specificity of optical imaging and the low-scattering nature of ultrasound, optoacoustics is an exciting imaging modality in which many developments have been made in the last ten years. These systems range from small animal tomographic systems [7, 8, 9], to handheld scanners [10, 11], to microscopy systems [12, 13, 14].

The principle focus of this thesis is the development of a microscopy system. Consequently, the theory behind decisions made during said development are presented in the relevant chapters.

Part I

Microscope System Development

Development of a Real-Time Optical- and Acoustic-Resolution Optoacoustic and Ultrasound Microscopy System

Chapter 2

Background

As already shown, in optoacoustic imaging ultrasound is generated inside the imaged media as a result of laser-induced thermoelastic expansion. Due to the low acoustic scattering of soft biological tissues, optoacoustics non-invasively provides images with diffraction-limited ultrasonic spatial-resolution at depths of up to several centimetres. Furthermore, although there exist many studies demonstrating the prowess of optoacoustic tomography systems, for optoacoustics to reach it's full potential as a system for use in functional and developmental neuroimaging studies the temporal and spatial resolution needs pushing to the next level. Namely, real-time optoacoustic microscopy.

High resolution optoacoustic microscopy (OAM) comes in the two main variants of optical resolution (OR-OAM) [15], and acoustic resolution (AR-OAM) [16, 13]. In OR-OAM an unfocused ultrasound transducer is used, and lateral-resolution is dictated by the beam width of the focused illumination at a given depth. In an optically non-scattering imaged media with an illumination beam of low divergence, the achievable lateral resolution could theoretically be very high (several μm) at a depth of several centimetres. However, typically biomedical imaging targets are optically scattering, and after a few hundred micrometers the beam is approximately diffuse, thus limiting effectiveness of the modality to the superficial regime [17]. In AR-OAM a focused ultrasound transudcer is used and illumination is broad with respect to the field of view of the transducer. This variant of OAM is successful at imaging many centimetres deep in optically scattering media, though the limit of achievable resolution is dictated by the properties of the transducer e.g. numerical aperture, bandwidth, sensitivity. Overall OR-OAM is capable of achieving greater resolution than AR-OAM, though AR-OAM is the only valid approach for deep-tissue imaging.

In Part I the development is presented for a real-time microscopy system capable of OR and AR optoacoustic, and pulse-echo ultrasound imaging.

Chapter 3

Raster Scanning System

Raster scanning is the process of scanning in parallel lines over a defined grid. This scanning method is slow but simple and robust, as such is was a natural starting point for building the first version an optoacoustic microscope.

3.1 System Overview

The first version of the microscope system acquired optoacoustic data at each position within a set of predetermined positions above the imaging target; this is illustrated in Figure 3.1.

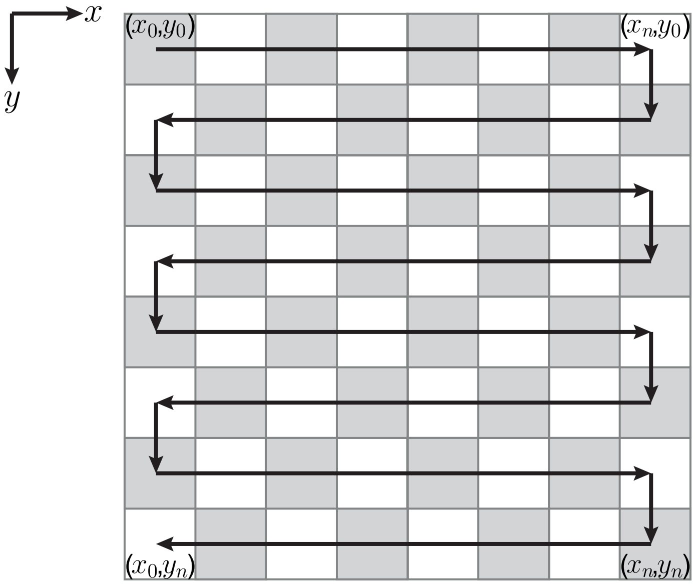

Figure 3.1: The geometry for a raster scanning acquisition locus.

The system initially used a spherically focused piezoelectric ultrasound transducer (InSensor, Kvistgaard, Denmark), with a centre frequency of

25 MHz, 60% available bandwidth, an outer diameter of 11 mm, and a focal length of 12.3 mm; this gives a numerical aperture in pure water of approximately 0.5. Through the centre of the transducer was a hole of 900 μm diameter. The purpose of this hole was to allow any fitting optical fibre to be inserted, giving illumination that would be coaxially aligned with the transducer focus. An illustration of the transducer-fibre assembly is presented in Figure 3.2.

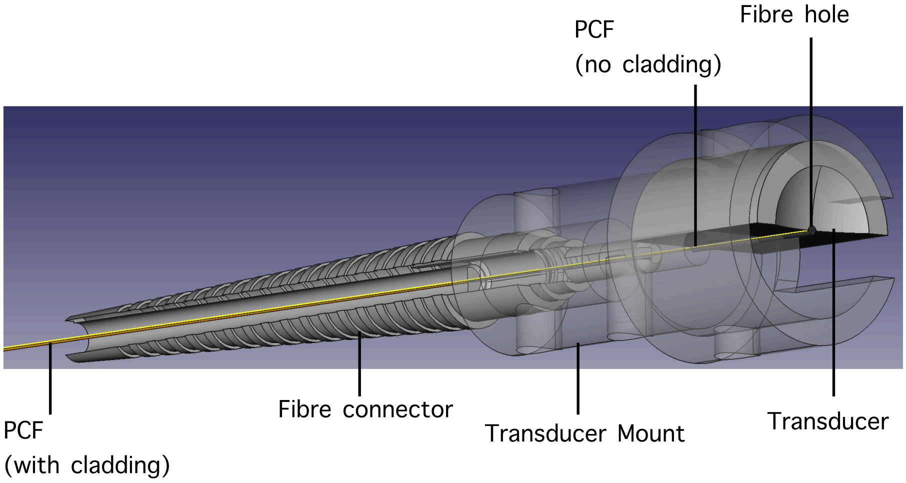

Figure 3.2: An ilustration of the 25 MHz piezo electric transducer and optical fibre assembly.

To scan the transducer-fibre assembly two motorised positioning stages were used. The x-scanning stage was a fast-scanning piezo stage (model M683; Physik Instrumente GmbH, Karlsruhe, Germany) and the y-scanning stage was a slow-scanning linear stage (model LTM 60F; Owis GmbH, Staufen, Germany); the scanning-head was attached to the piezo stage by an in-house manufactured plastic mount. The stage and scanning-head assembly were then attached to a non-motorised coarse-positioning linear stage for vertical translation (model: SLW-25120-AWM-500; Igus GmbH, Köln, Germany). This allowed the head to quickly be moved large vertical distances, which facilitated experimentation. To mount to the stage-head assembly to the vertical translation stage, a large, stiff and heavy (8 kg) aluminium block was machined in house. The importance of the weight and stiffness was to present a great inertia to the motorised stages, in view of the overall aim of real-time scanning, so as to minimise torque induced vibration-based errors in positioning when moving the stages quickly.

The illumination was provided by the combined use of an end pumped

Nd:YAG Q-switched laser (model IS8II-E, Edge- Wave GmbH, Wuüselen, Germany) combined with a dye laser (Credo, Sirah Lasertechnik GmbH, Grevenbroich, Germany). This combination was capable of a 10 kHz repetition rate and had a tunable wavelength of between 575 and 605 nm when using the dye Pyrromethene 597. The acoustic data was acquired using one channel of a 14 bit high-rate data acquisition card with a maximum sampling rate of 250 MSs^{-1} (model: M3i.4142, Spectrum Systementwicklung Microelectronic GmbH, Grosshansdorf, Germany). To sample the laser power per-shot the beam was sampled immediately prior to the optical fibre input (1%) and measured with a photodiode. The voltage from the photodiode was then recorded using a second channel of the high-rate data acquisition card. Both the illumination and acquisition were triggered by a signal generator. A complete schematic of the raster scanning system is shown in Figure 3.3.

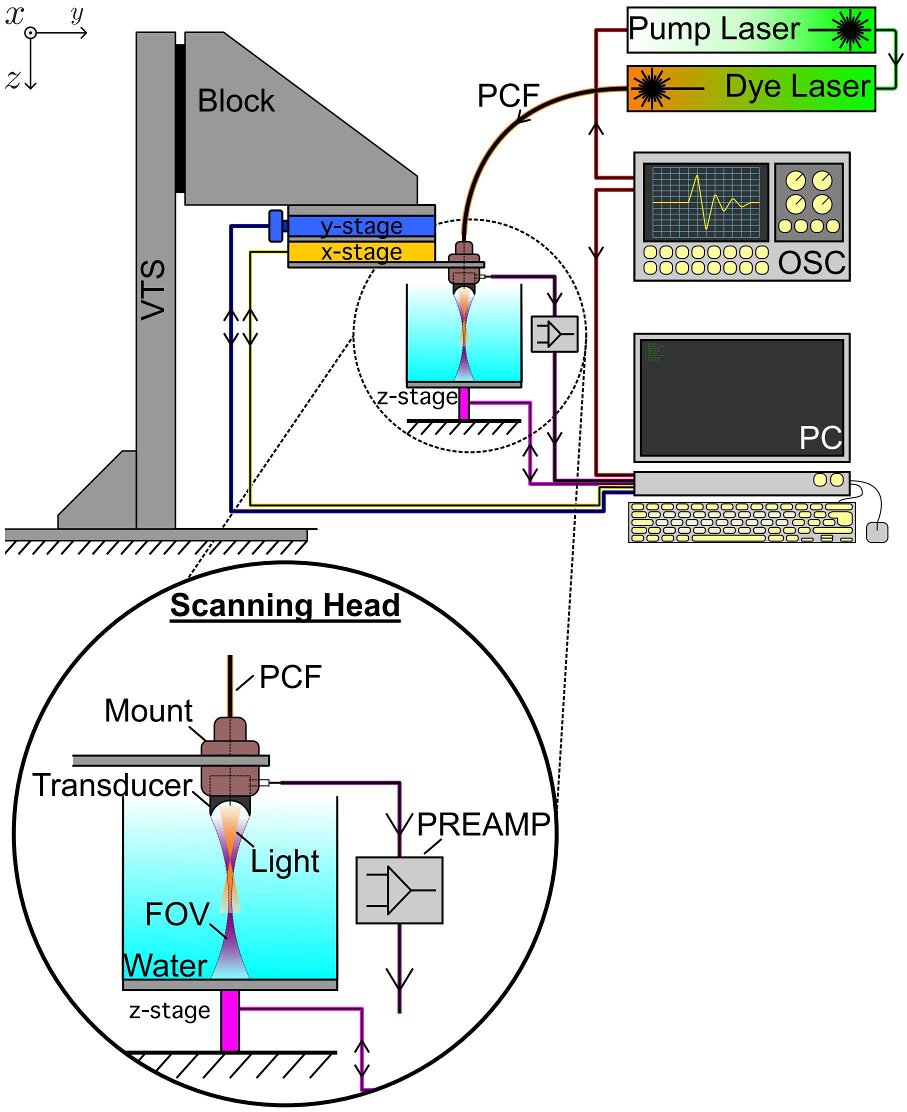
x
y
z
Block
VTS
y-stage
x-stage
PCF
Pump Laser
Dye Laser
OSC
PC
z-stage
Scanning Head
PCF
Mount
Transducer
Light
FOV
Water
PREAMP
z-stage

Figure 3.3: A schematic of the raster scanning optoacoustic microscope. VTS is the coarse large-range manual vertical position stage. The trigger signals from the oscilloscope (OSC - red) fired both the pump laser and started the data acquisition card on the PC. The $x-$, $y-$ and $z-$stages (red, yellow, pink) were controlled from inside the scanning routine on the PC. Detected ultrasound signals were passed to the PC via a preamplifier (purple). Water was necessary as the transducers are water-coupled. The inset figure shows how the field of view (FOV) of the transducer (purple) and a the excitation light emitted by, in this illustration, a photonic crystal fibre (PCF).

3.2 Ultrasound Transducers

The first transducer used in the system was a 25 MHz piezoelectric ultrasound transducer. With a focal length of 12.3 mm it was known from the outset that a very high fluence would be necessary to generate ultrasound both at and deep of the focus i.e. for full-depth scattering volume scans, such as a mouse brain. However, for thin biological targets placed at the focus (mouse ear, human palm, etc.), or for low-scattering phantom volumes, this problem would be avoided. Overall then it was decided to use this transducer while the system was in it's infancy to acquire simple data sets during testing. Though once the system began to come together and the needs of the project known, a new transducer would need to be purchased.

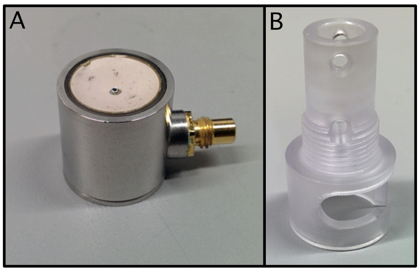

Figure 3.4: A: The 25 MHz piezoelectric transducer, with central 900 μm hole clearly visible; B: the custom plastic mount.

To asses the characteristics of the detector the electrical impulse response (EIR) was measured as per [3]. From this the frequency response function (FRF) was calculated via the fast-fourier transform, and the spatial impulse response (SIR) was modelled using the software package *Field II* [18].

Continuing from the introduction in Part I, the procedure for measuring the EIR of an optoacoustic system can be summarised as follows. The response of the detector would be best measured if a spherically propagating Dirac-delta acoustic wave were incident on its surface, originating at the exact focus. The practical method of best approximating this situation, is to put an optoacoustic source at the focus which will produce a peak centre frequency far above the nominal centre frequency of the detector. Thus, the incident acoustic wave is seen by the detector as a near-Dirac wave. The two main methods trialled for this process were to use a microsphere and broad illumination, or to use a very thin black layer (such as tape or a painted surface) and a very tightly focused optical spot. The advantage of the black-layer approach was that it was experimentally far more simplistic, whereas the advantage of the microsphere was spherical wave generation. The disadvantage of the black-layer method was ablation from the tight optical focusing, and the disadvantage of the spheres could be their inconsistent size and coating, and that they are difficult to locate. The results of the characterisation of the 25 MHz piezoelectric transducer by a microsphere are presented in Figure 3.5.

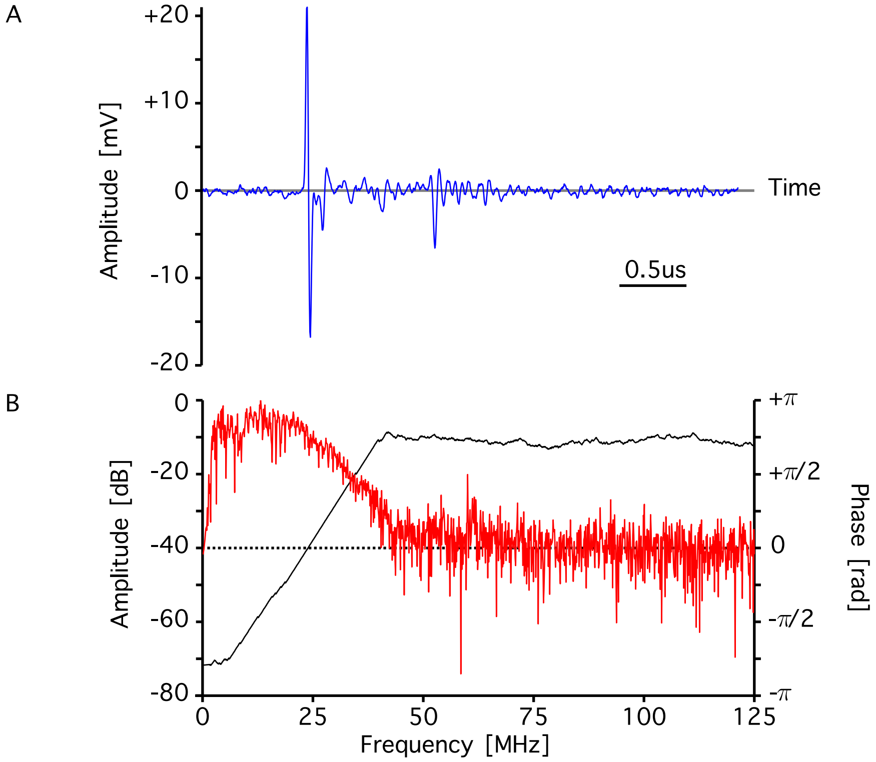

Figure 3.5: A: The electrical impulse response (EIR) of the 25 MHz piezoelectric detector, as measured with a 10 μm microsphere; B: the frequency response function (FRF) of the detector, as determined from the EIR, where red is the amplitude response and black is the phase.

From equation (1.12) the lateral focal width was estimated to be approximately 68 μm. The characterisation for the piezoelectric detector shows a peak sensitivity at around 15 MHz, lower than was expected. Through the region of spectral fidelity it has a linear phase response, which is lost above 40 MHz and below 10 MHz. The spatial impulse response (SIR) for this transducer, as modelled through Field II, is presented in Figure 3.6.

In view of the characterisation results, and the quality of optoacoustic images achieved through scanning with this transducer, the desired properties for the transducer to be ordered were decided upon. This transducer (Precision Acoustics, Dorchester, UK), presented in Figure 3.7, had a polyvinylidene fluoride (PVDF), rather than piezo-electric, active surface. The PVDF choice was made for two major reasons. Firstly, it can easily be laid onto a pre-machined spherical surface. Secondly, it has much wider and flatter frequency response i.e. it is practicably sensitive to a greater range of

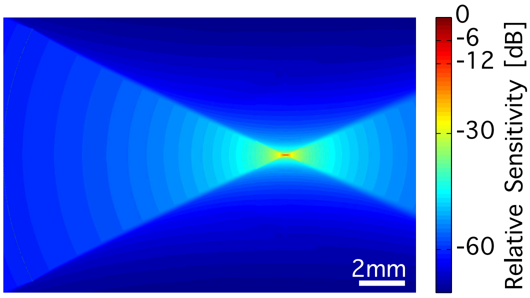

Figure 3.6: The modelled spatial impulse response for the 25 MHz piezoelectric detector.

frequencies. This detector was again spherically focused, with a focal length of 6.8 mm, a centre frequency of 30 MHz and an outer diameter of 6 mm; again the centre hole had a diameter of 900 μm. This shorter focal distance was selected based of a criterion of how deep the peak sensitivity should be inside a mouse brain when fluence was considered i.e. how deep of the illumination surface should the acoustic focus be.

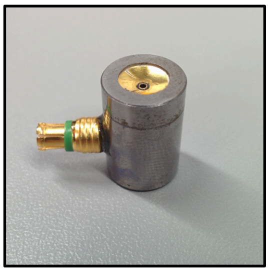

Figure 3.7: The PVDF transducer.

In the same fashion as for the 25 MHz piezoelectric transducer, characterisation tests were performed for the PVDF detector, and the SIR was modelled. The results of this are presented in Figure 3.8 and 3.9, respectively.

One stark difference in the EIR measures for the PVDF and 25 MHz piezoelectric detector is signals themselves. Both were measured following identical protocol and equipment. The PVDF signal was cropped about the non-noise response, which was possible due to the very high SNR i.e. easy observation of where the signal began and returned to the noise floor. The piezoelectric transducer, however, presented a much noisier signal, which made accurate temporal gating impossible. Additionally, the PVDF detector displayed the expected heavily-damped ringing signal characteristic of an ultrasound detector, whereas the piezoelectric response was far less expected with a strong reflection-like signal significantly after the first peak.

The FRF for the PVDF detector shows the -5dB crossings at approxim-

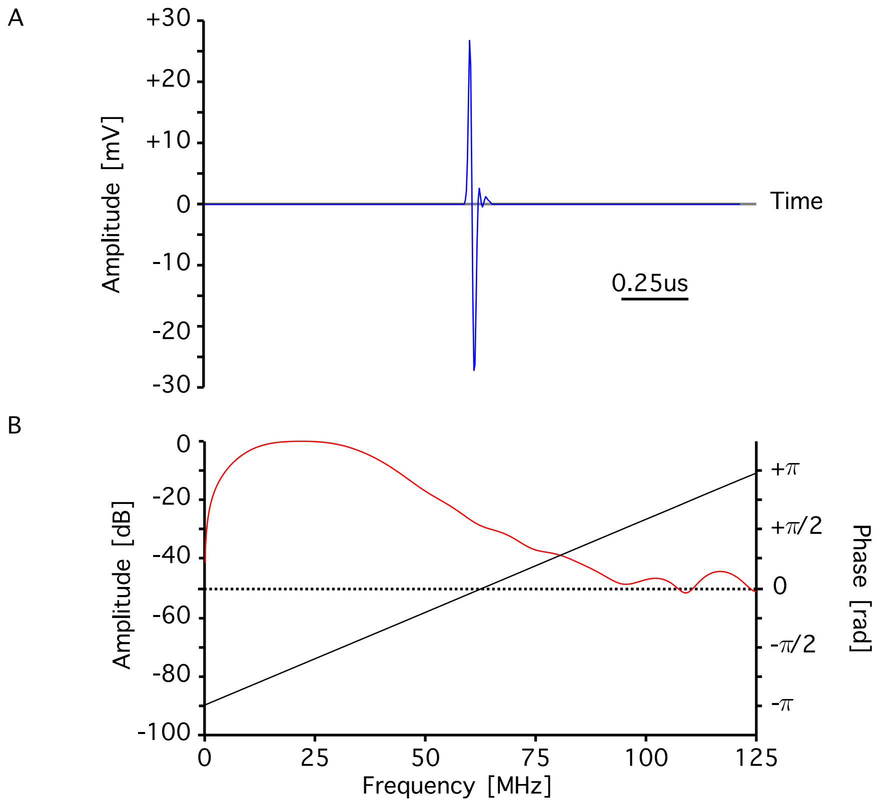

Figure 3.8: A: The electrical impulse response (EIR) of the PVDF detector, as measured from a 10 μm microsphere; B: the frequency response function (FRF) of the detector, as determined from the EIR, where red is the amplitude response and black is the phase.

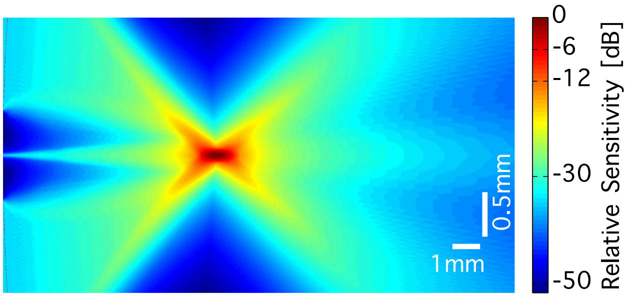

Figure 3.9: The modelled spatial impulse response for the PVDF transducer.

ately 8.2 MHz and 37.8 MHz. This is far more practicable for optoacoustic microscopy when compared to the heavy-ringing response for the piezoelectric detector, which has a peak sensitivity loosely between 10 and 20 MHz.

3.3 Optical Fibre

As mentioned previously, the design for the system was to situate an optical fibre in a hole at the centre of the ultrasound transducer, thus aligning the focus of the detector with the centre of the illumination. The simplest implementation of this is, hypothetically, to use a large numerical aperture multimode fibre with a broad diameter. This would ensure a large illumination spot (1-10 mm) whilst minimising any potential problems in coupling an input beam in terms of power and input spot-size. Such a fibre would, however, only ever be useful in an acoustic resolution system i.e. acoustic-focus dictated resolution. Conversely, using a very-low numerical aperture single-mode fibre with a small diameter would give a fluence dictated resolution i.e. an optical resolution system. Furthermore, the output of a single-mode fibre is possible to focus, which would increase lateral resolution further still. The problem with the latter would be coupling sufficient power into the single-mode small-diameter fibre to ensure fluence at depths. Thus, as can be seen, achieving a deep-penetrating fluence with a low numerical-aperture is by no means a trivial problem.

While the problem described above was considered and different solutions weighed, the first instance of the system implemented two fluence delivery methods. Both designed to provide acoustic resolution only, the initial target was to achieve acoustic resolution optoacoustic microscopy data sets, and to use information learned along the way to influence the design of the focused fluence delivery design. The first approach was to, as suggest previously, use a large numerical aperture multimode fibre; the second was to use a liquid light-guide. The multimode fibre (FT600UMT Thorlabs GmbH, DE) had a core diameter of 600 μm and cladding diameter of 630 μm , with a numerical aperture of 0.39. This broad core and comparatively high NA were selected to try and deliver maximum laser energy to the target with a broad surface spot. The liquid light-guide (Lumatec, Deisenhofen, DE) had a diameter of 3 mm, and as such was capable of carrying light of very high power. This in conjunction with the diameter of the output spot of the lightguide being very broad (1-3 cm) made for a very good broad-illumination source. Obviously this would only be useful for static-fluence scans however, as the light guide could not be positioned through the centre of the transducer.

To address the issue of needing a large diameter to couple sufficient power, wanting a low numerical aperture, and the possibility of focusing, it was decided to implement a photonic crystal fibre, PCF (model LMA20, NKT Photonics A/S, Birkerd, Denmark). A photograph of the tip of the PCF is shown in Figure 3.10.

Clearly visible in Figure 3.10 is the regular honeycomb cross section of the PCF. This honeycomb is the mechanism by which the fibre guides the light, rather than a radially varying refractive index as per a conventional

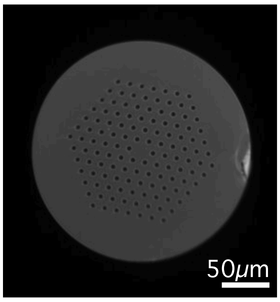

Figure 3.10: A photograph of the output-tip of the photonic crystal fibre.

optical fibre. The honeycomb is a regular structure of air gaps, and the central position where it could be said there is a missing hole is the active core along which the light is guided; this can be considered similar to a single-mode fibre core. Additionally, all the interstitial non-air regions can be considered single-mode fibre cores. Furthermore, it is possible to take this many-single-core output and focus to a spot, which is not possible with the output of a multimode fibre. The PCF used had a numerical aperture of 0.033 at 780 nm, and an outer diameter of 230 μm, an inner core diameter of 20 μm, and a mode field diameter of 15 μm.

To focus the output of the fibre was also a non-trivial problem. The difficulties here came from the small scale of the components and the concept of mounting the optics in the centre of the ultrasound transducer; the idea of mounting a combination of lenses at the fibre tip was impracticable. As such the design decided upon used a gradient index (GRIN) lens (Grintech GmbH, Jena, Germany). A GRIN lens has a refractive index which varies with distance from the axial centre, as illustrated in Figure 3.11.

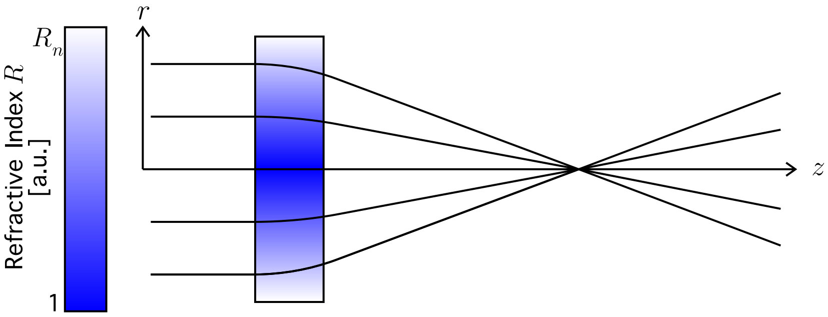

Figure 3.11: An illustration of how the radially varying refractive index, R, of a GRIN lens focuses light, where r and z are radius and depth, respectively.

The GRIN lens, with a focal length of 6.5 mm, was placed on a spacer a distance of 3 mm from the tip of the fibre; the theoretical diffraction limited spot size of the focused output beam was 25 μm. This assembly was contained within a metal tube of 700 μm outer diameter. An illustration of the fibre-lens assembly is presented in Figure 3.12.

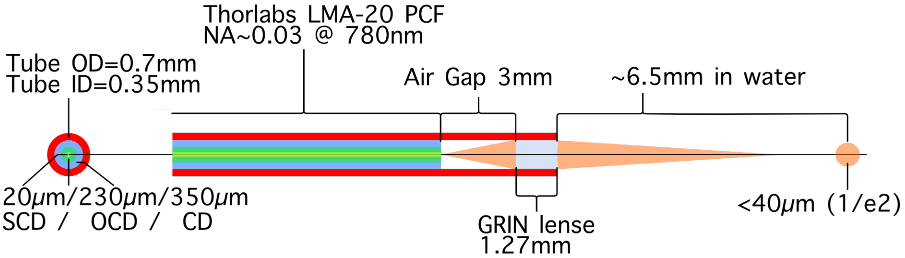
Thorlabs LMA-20 PCF
NA~0.03 @ 780nm
Tube OD=0.7mm
Tube ID=0.35mm
Air Gap 3mm
~6.5mm in water
20μm/230μm/350μm
SCD / OCD / CD
GRIN lense
1.27mm
<40μm (1/e2)

Figure 3.12: A diagram of the combined PCF and GRIN lens assembly; SCD, OCD and CD are the single-core, outer-core, and coating core diameters, respectively.

3.4 Control of the system and operation

The raster scanning system is controlled via a Matlab generic user interface (GUI). The GUI can be considered an interface to a Matlab wrapper function which passes the necessary inputs to the relevant sub-functions (C++, mex, m) and device libraries (dll). In addition to initialising scans, the GUI presents a preview to the data acquired once scanning is complete. Two additional functions of the GUI are as an oscilloscope for optoacoustic and acoustic data, and for on-the-fly 2D-imaging at a fixed y-position along a range of x-positions (B-scans). These two functions are of greatest use when focusing the system, and when checking the region of interest to be scanned. Additionaly, the laser power can be inspected also from within the scope function.

Figure 3.13 illustrates the hierarchy of the control structure of the code, and the order in which commands are passed to perform a raster scan.

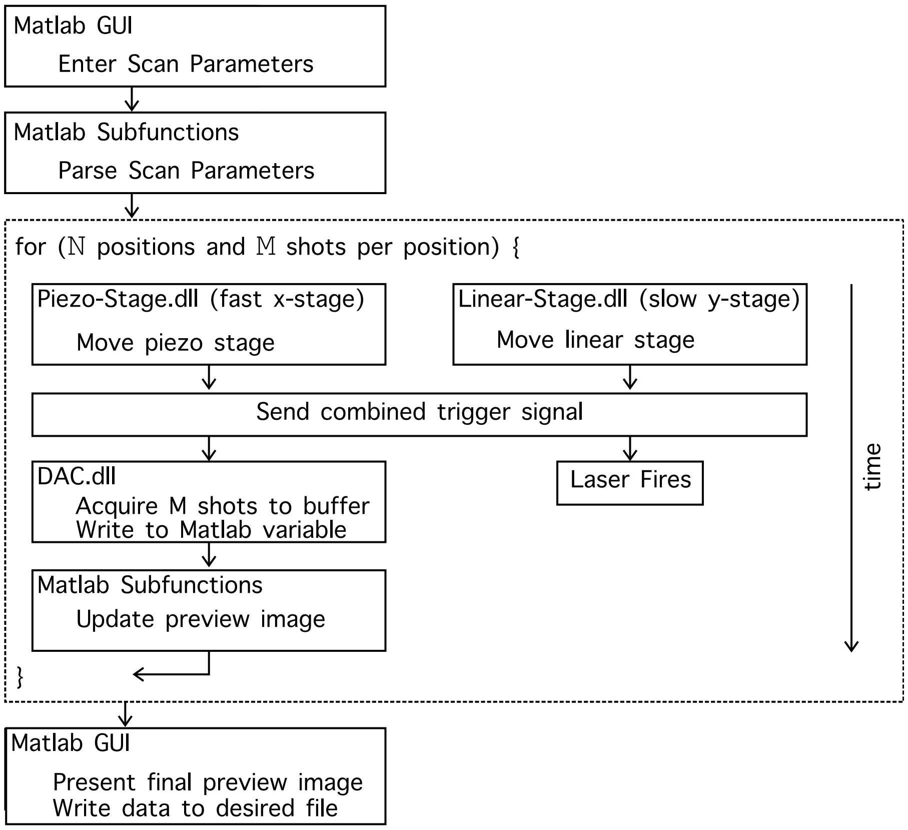
Matlab GUI
Enter Scan Parameters
Matlab Subfunctions
Parse Scan Parameters
for (N positions and M shots per position) {
Piezo-Stage.dll (fast x-stage)
Move piezo stage
Linear-Stage.dll (slow y-stage)
Move linear stage
Send combined trigger signal
DAC.dll
Acquire M shots to buffer
Write to Matlab variable
Laser Fires
Matlab Subfunctions
Update preview image
}
time
Matlab GUI
Present final preview image
Write data to desired file

Figure 3.13: A diagram of the hierarchy of the code and the order of commands to perform a raster scan.

One component of the code structure in Figure 3.13 yet to be discussed is the combined trigger. In the raster scanning system both the laser and data acquisition are triggered by a single signal generator. However, there exists a delay between the laser receiving the trigger pulse and firing of 100.4 μs. As such, the trigger signal used is a TTL 5V pulse with a 100.4 μs width, from which the positive edge triggers the laser and the negative edge triggers the data acquisition card.

3.5 Experimentation

The raster scanning iteration of the system was never intended to be used in performing biological studies, primarily because the runtime was too slow. Rather, it was an intermediate step towards a fast-scanning system, where it was then often used as a complementary scanning mode. However, raster scans were commonly made for phantoms where accurate positioning, a very small scan region, or a high number of averages were necessary. These phantoms were typically designed to investigate certain behaviours of the illumination-detection system, to provide data to test post-processing algorithms on, or to investigate physical properties of commonly encountered materials or structures. One invaluable use of the raster scanning mode was to perform sequential scans over increasingly smaller areas in efforts to ascertain the location of a small target. For example, in transducer characterisation scans microspheres of diameters in the order of 10 μm were often used due to their near point-source-like characteristics. To locate a microsphere of this size in an agar phantom several milimeters in size is non-trivial. For although the obvious step to take would be to insert a marker of larger size into the phantom, this marker must be either optoacousticaly invisible, or removable without leaving any potentially distorting remains such as dye. An additional use was to experimentally determine the speed of sound in a target volume. Here, a small region of interest scan could be made several times with a known translation of the target volume in depth, z between each scan; for example, scanning a microsphere at 5 depth intervals of 0.1 mm. With these data sets the known z-steps could be plotted against the time-samples for the peak amplitudes of the tracked source. Fitting a curve to these time-distance data sets, the speed of sound could therefore be estimated as the gradient of the fit.

A typical raster scan volume is presented in Figure 3.14. This method of presenting data is common throughout the thesis, and can be considered analogous to sinograms in CAT imaging. This figure presents one slice of the 3D scan volume at $y = 0$, so each column of pixels is one x-position, and each row is one time sample, $z \approx ct$, with the colour of any (x_i, t_j) pixel indicating the amplitude of the time-sample t_j of the signal $x(t)$ at position (x_i, y_0). The data presented in Figure 3.14 is from a phantom containing a 20 μm sphere that was scanned for an x–y range of 1.9x1.9 mm. The scan was performed 5 times with the phantom positioned at 5 different depths centred about the acoustic focus $z = z\prime$; thus, the presented volume is a composite volume formed from the sum of the 5 sub-scans. For the illumination several multimode fibres were arranged around the phantom, and remained stationary during scanning, ensuring a true AR data set. Figure 3.14A presents the centre slice of the scan volume, and Figure 3.14B presents the corresponding slice from the result of post-processing the scan with a novel version of the sythetic aperture focusing technique for optoacoustics, WSAFT, which is presented in detail later.

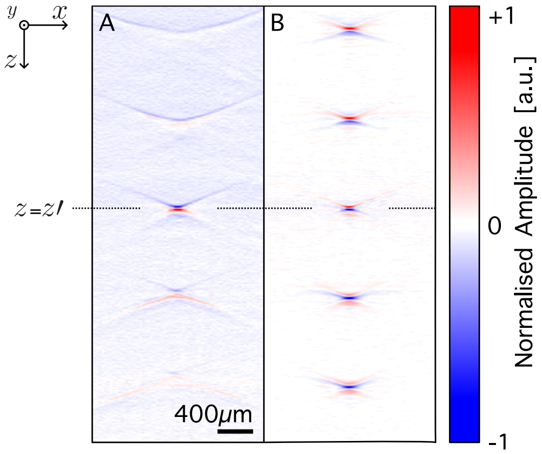

Figure 3.14: Central slices for A: an AR data set of a 20 μm microsphere raster scan and B: the WSAFT result for the scan.

An example data set for an OR raster scan is presented in Figure 3.15. Here 5 sutures of 50 μm diameter were staggered vertically in a cylinder of non-scattering agar, and the illumination was delivered via the multimode fibre inserted through the transducer hole. This experiment was a precursor to later work on fluence considerations in post-processing algorithms, and was performed to test the usefulness of such a phantom. One very common way of visualising OAM scan volumes, both AR and OR, is through maximum amplitude projections (MAPs) in one scan-dimension. In figure 3.15A a MAP through depth, z, is presented. Here, the amplitude of any (x_i, y_j) pixel is the maximum amplitude found in the column of data (z, x_i, y_j). As can be seen MAPs are therefore a useful visualisation technique, however they do lose the information about where these structures are in the volume. Therefore, in addition to conventional MAPs, this thesis frequently uses MAPs colour-coded for depth as per Figure 3.15B. In this type of image the brightness of a pixel indicated amplitude, and colour indicated depth. Here, for example, it can readily be seen from A and B that some sutures were detected with a lower amplitude than others; in B this observation can be extended to see that distance to the acoustic focus (at around 6.8 mm - green) is the key reason for this.

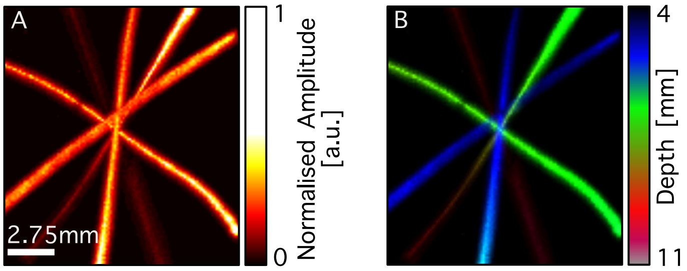

Figure 3.15: Maximum amplitude projections in z for an OR raster scan of a 50 μm suture, with **A**: a colourmap for amplitude and **B**: a colourmap for depth.

As was previously stated, raster scanning was very useful in orienting oneself over an imaging target, and in the location of certain structures or objects. Presented in Figure 3.16 is an example of using sequential raster scans to locate a microsphere. In this experiment a 40 μm microsphere was placed at the end of a 20 μm diameter suture. The intended goal was to make raster scans of increasingly small regions at increasing resolution so as to locate the sphere by following the suture to its tip before refocusing for the sphere. As was previously stated, markers such as this suture pose problems in some experiments because they themselves are optoacoustic sources. Nonetheless, these MAPs in depth, z, show how useful it was to use the raster-scan mode as a quick tool to search and orientate within an imaging target.

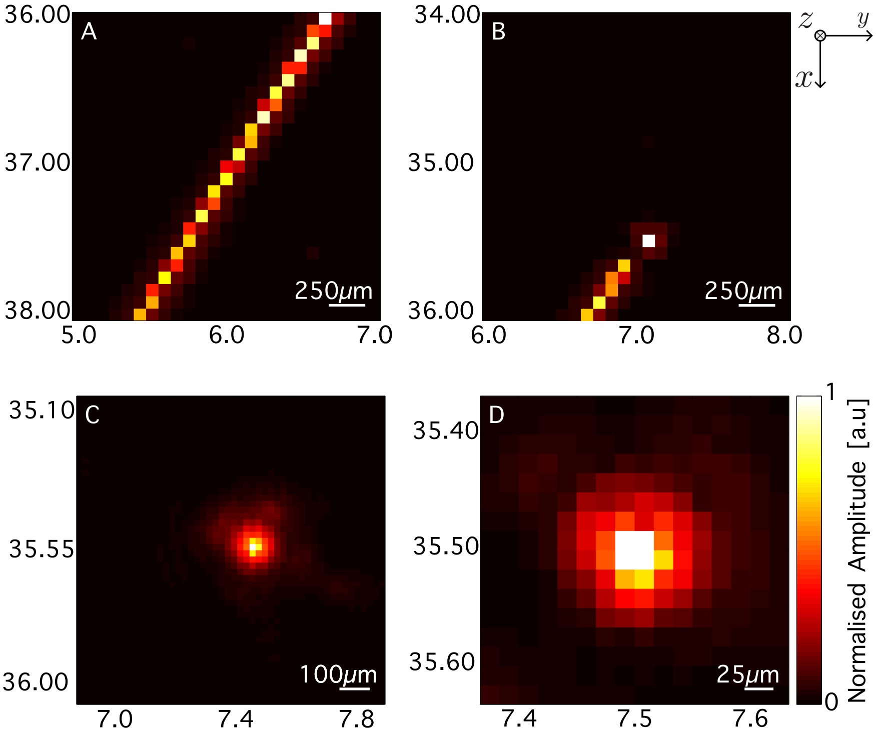

Figure 3.16: Maximum amplitude images in depth, z, for a series of raster scans performed to locate a 30 μm microsphere at the tip of a 20 μm diameter suture. Scans were performed over smaller regions and at higher resolution iteratively from A through D.

3.6 Discussions

The main observation to take from Figure 3.14 is that while the AR data of the scan (A) can be post-processed to yield a meaningful image (B), the raw scan volume itself only presents useful information at or very near the focal depth $z\prime$. As separation distance from the acoustic focus to the sphere increases then the image of the sphere at that position loses lateral focus, and the amplitude of the sphere signals decrease. Although the out-of-focus blurring is intuitive, the nature of the amplitude behaviour is unique to optoacoustics. This is because in ultrasonics, for example, the spherically focused transducer emits (sends) a pressure wave that is a section of a surface of a sphere. The wavefront then propagates along the radius of that sphere, and at the origin forms a focal point of maximum intensity i.e where the wave passes through the smallest volume in space. Having passed the focus, the wave then propagates along the radius away from the detector in exactly the same fashion. Therefore, because in ultrasonics the signal detected is a reflected portion of the emitted wave, it is intuitive that any microspheres, as per the phantom scanned here, only produce signals proportional to the the amount of energy incident upon them. That is to say that a perfect reflector of finite size positioned at the focus could return a wave with 100% of the energy of the sent wave, whereas the same finite reflector positioned interstitially of the focus and the transducer may only be irradiated by 50% of the sent wave, and thus only capable of returning 100% of 50% of the energy of the sent wave. The major difference here between optoacoustics and ultrasonics is that identical optoacoustic sources illuminated uniformly will generate equal amplitude pressure waves. Although this difference may appear obvious, it is often neglected when considering properties of the images during inspection, and in the implementation of delay-and-sum based post-processing algorithms.

When performing AR scans there are several considerations that were made to try and ensure high-quality data. The first consideration is the light fluence. The optimisation to be made in this regard is that the amplitude of an optoacoustic signal for an optical absorber anywhere within the target volume (or region thereof) is directly proportional to the fluence at the position of the absorber. Therefore, to increase the amplitude and SNR of the signal detected the fluence must be increased. The danger of increasing the illumination power to increase the at-depth fluence is that the fluence elsewhere is too high, and damages the target volume e.g. burning a biological target. One alternative option is to, as was already suggested, employ a shot-averaging scheme. Here, by summing many low-SNR signals for each position the overall SNR of the volume can be increased through the constructive interference of the signal versus the largely destructive interference of the background noise. However, using a firing rate of 10 KHz, and firing for 1s at each acquisition position will not necessarily negate damaging the volume, thus care must still be taken. The second consideration is the location of the acoustic focus within the volume. The transducer will most efficiently convert incident optoacoustic waves into electrical signals when they originate from the acoustic focus. Although optoacoustic waves originating out-of-focus can be refocused in post-processing, the decreasing SNR, as well as spatially determined detection artefacts, limit the performance of these algorithms. Furthermore, it is imperative that the acoustic focus be positioned at the key region of interest for the volume. If the region is very large in terms of depth, then a slight superficial-to-focus bias is preferred i.e. positioning the acoustic focus slightly deep of centre in the region of interest.

With OR data, as can be seen in Figure 3.15, several of the observations for AR data remain just as important. For instance, from 3.15B, it can be seen that although the unscattered fluence beam dictates and preserves lateral resolution all the way through the phantom, the greatest amplitude signals are from sutures situated at, or very near to, the acoustic focus i.e. the green portions of sutures at around 6.8 mm depth. Also, optoacoustic waves are generated solely in the presence of, and with amplitude directly proportional to, the illumination fluence. Perhaps the greatest restriction for OR scanning is the fluence intensity at the scattering surface of the imaging target. Although thus far only data from a multi-mode fibre was presented, consider the schematic of the GRIN lens and PCF in Figure 3.12. Here it can be seen that the focal spot size of the output beam is $< 40\mu\text{m}$ $(1/\exp^2)$. Therefore, given a pulse repetition frequency of 1KHz, a per-pulse laser energy range of 50-500 μJ, and a focal area of around 0.005 mm^2, the average intensity of the illumination at the focal spot falls into the range of around 1-10 kW/cm^2. Furthermore the potential for damaging the phantom at the optical focus is clear, and so ensuring sufficient fluence deep of the optical focus yet without causing thermal damage at the focus is a optimisation that must be made on a per-volume basis. However, pure OR-OAM is therefore classically limited to the superficial-depth regime. Further similarities between OR and AR data, and the transitional regime between the two, are presented at length later.

Overall, the raster scanning system is a robust system for acquiring both AR-OAM and OR-OAM images and for the empirical determination of the speed of sound. The main disadvantage is the acquisition speed for a full image volume. For a scan of 133x133 positions, with an 1800 sample acquisition for each position, scanning time for the raster system takes between 60 and 90 minutes depending on the number of shots acquired per position. This alone shows the motivation to move to a fast-scanning mode of operation for the system.

Chapter 4

Fast Scanning System

The main motivation to develop the fast scanning system was to provide realtime optoacoustic neuroimaging in mice. Logically, the fast scanning OAM system was a development of the raster scanning system from the previous chapter. Therefore, to achieve the aim of realtime imaging many changes had to be made.

4.1 System Overview

The main acquisition-time bottleneck in the raster system was the move-wait-acquire-repeat nature of the scans. As such, it was decided to move from this discretised raster scanning method to that of continuous motion of both stages with high repetition rate optoacoustic signal generation and detection (up to 10 kHz). Under the new scanning regime the linear stage was to move slowly, while the piezo stage would scan quickly, thus ensuring a sinusoidal locus for the laser head which could later be rasterised into a uniform matrix. An illustration of the fast-scanning locus can be seen in Figure 4.1. Needless to say, this scanning regime presented new challenges.

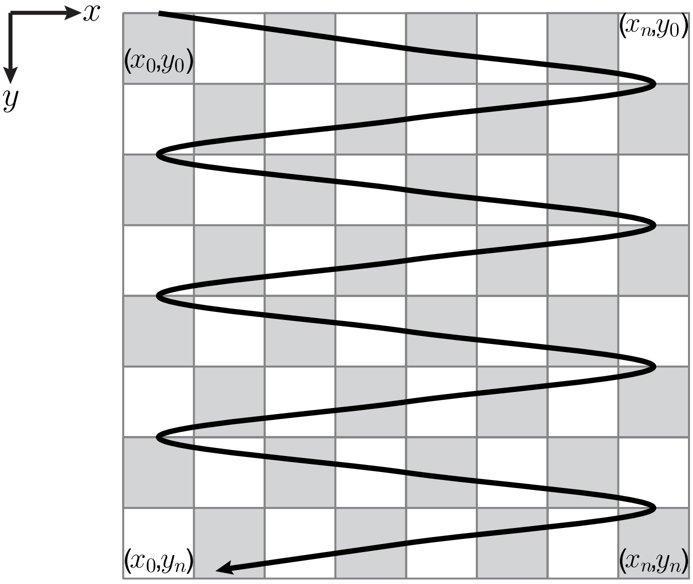

Figure 4.1: The locus for the fast-scanning regime. The linear stage scans slowly in the y-direction while the piezo stage scans rapidly in the x-direction; both stages are under constant motion during a scan.

In the raster scanning system the position of the laser head was known for each acquisition, now it was necessary to determine the position on-the-fly. Initially efforts focused on reading the position of the piezo stage and linear stage from their respective controllers. However, this approach was floored in two ways. Firstly, the controller for the linear stage could indeed buffer the position data onboard, and then the data could be requested from the controller via the control library. The problem here was the speed with which the controller could pass the data back to the computer, and the amount of data which it could buffer. In brief, the feedback for a crossing of the linear stage across the scan area took up to 2 minutes to read back, and any larger data sets were not practicable. Additionally, the slow read-back speed would make on-the-fly assignment of position data to each measurement impossible. Secondly, the piezo stage controller could not return instantaneous position while moving. One approach to solving this was to read the voltage across the piezo directly by soldering new connections across the stage terminals. This approach was floored because the piezo stage was under high-tension, which raised issues of both safety and practical acquisition, and because the preliminary signals measured were too inaccurate. These problems led to the decision to employ a laser-distance sensor to acquire a position for the piezo stage at each measurement point in parallel to the acoustic acquisitions. Due to the slow repeatable nature of the linear stage scanning, it was decided to buffer and transfer data from the controller for a movement across scan region. This buffered data would then be used as a velocity profile to predict the position of the stage at a given point in time throughout the course of a scan. The calibration would also only need to be performed once per region of interest to be scanned.

The acquisition of the data for the fast scanning system also had to be redesigned. In the raster scanning system the data at each position was returned to Matlab and stored in a position-based matrix of N_t-N_x-N_y samples. For the aim of fast-scanning it was not practical to return each acquisition, the corresponding position data, and laser power data for each position on the fly. As such, the data was buffered in a first-in-first-out (FIFO) buffer on the fast-sampling DAC, with one channel recording acoustic data and the second channel recording the laser power data. The output from the laser-distance sensor, which could only sample position at a maximum sampling rate of 10 kHz, was recorded by a second slower-sampling DAC (NI PCIe-6321, National Instruments, TX, USA). The high-speed DAC wrote the buffers to the RAM of the PC, and after total acquisition the RAM-stored data was transferred to the internal hard disks of the PC alongside the laser-distance sensor data as three sequential binary data files. Post acquisition these files were read into Matlab and signals were assigned positions within a regular position based volume such as that produced by the raster system.

For the raster scanning system the step size and range of the scan (or region of interest) were predefined, and this was also true for the fast scanning system. The difference was that the with the fast scanning system the combined velocity profile of the piezo and linear stages was first determined during a calibration movement. From this calibration profile the pulse repetition frequency necessary to ensure the desired step size at the region of greatest velocity was calculated. Although this was very successful in ensuring the necessary shot-density at the centre of the piezo stage's range of motion, it also gave a spatial oversampling elsewhere i.e. more acquisitions per area than desired. To place the acquisitions into the matrix a set of indices were found for a nearest neighbour interpolation between the empirical position values and the predefined step-size and region of interest i.e. acquisitions were binned into the nearest corresponding position index. In the first iteration of this data-positioning code acquisitions simply overwrote any shot already assigned that position. Finally, processed data was saved as a Matlab archive (.mat) and could be readily reloaded for post-processing and analysis later with ease.

A schematic of the fast scanning system is illustrated in Figure 4.2. In addition to the addition of the laser distance sensor (LDS), code was added allowing the oscilloscope to be controlled from the PC.

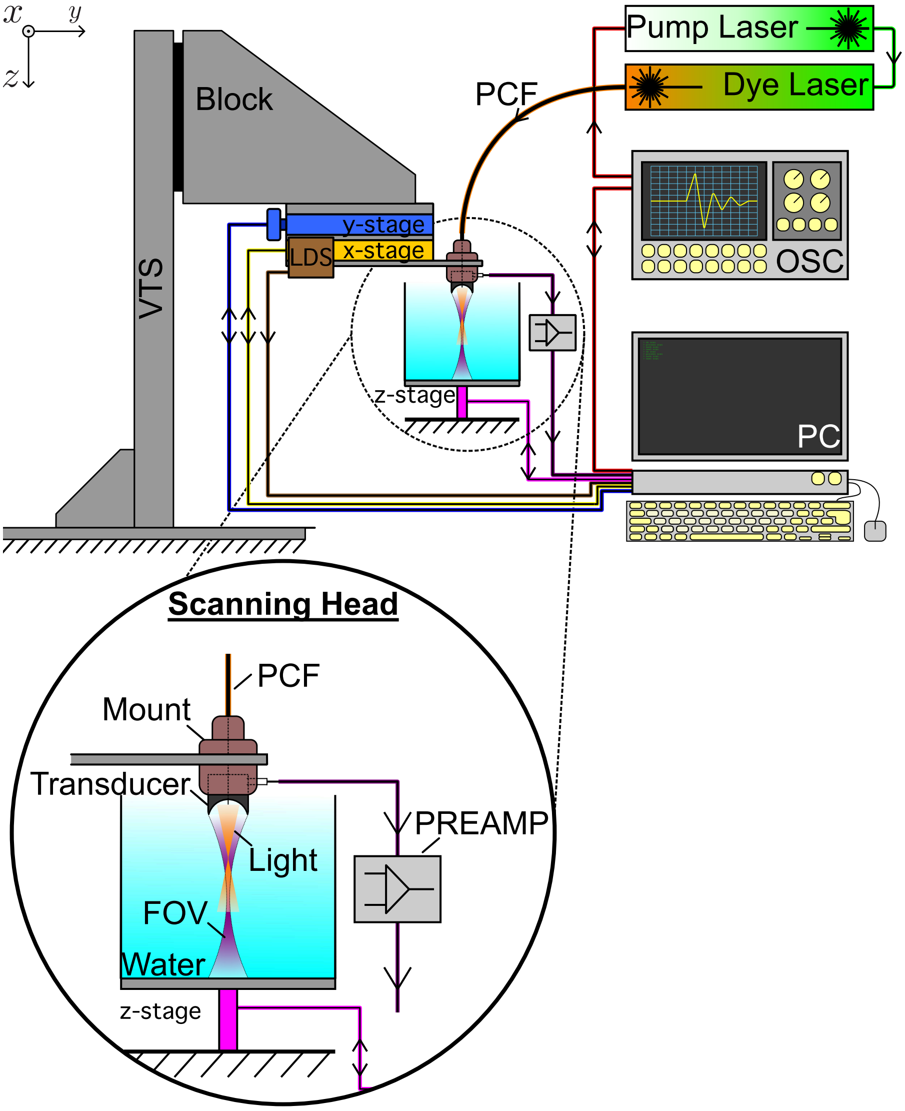
x
y
z
Block
VTS
y-stage
x-stage
LDS
PCF
Pump Laser
Dye Laser
OSC
PC
z-stage
Scanning Head
PCF
Mount
Transducer
Light
PREAMP
FOV
Water
z-stage

Figure 4.2: A schematic of the fast scanning optoacoustic microscope. VTS is the coarse large-range manual vertical position stage. The trigger signals from the oscilloscope (OSC - red) fired both the pump laser and started the data acquisition cards on the PC. The $x-$, $y-$ and $z-$stages (red, yellow, pink) were controlled from inside the scanning routine on the PC; the signal from the laser distance sensor (brown - LDS) was used to calibrate the x-stage motion. Detected ultrasound signals were passed to the PC via a preamplifier (purple). Water was necessary as the transducers are water-coupled. The inset figure shows how the field of view (FOV) of the transducer (purple) and a the excitation light emitted by, in this illustration, a photonic crystal fibre (PCF).

4.2 Power Limitation and Spatial averaging

The per pulse laser energy would fluctuate at a rate of approximately 0.05 Hz during the course of a scan. Given one laser shot of low power and one of high power incident on an identical absorber and identical detection, the high power shot would yield a detected ultrasound signal of greater amplitude as per equation 1.14. This point is intuitive and not apparently problematic. However, as previously stated, the first rasterising regime used to assign acoustic acquisitions to positions within the final data matrix would simply overwrite any existing acquisitions at that position. As such a signal with high amplitude (good SNR) could be replaced by one with low amplitude (poor SNR) or vice versa. This is clearly non-optimal and as such two steps were taken to properly handle the laser power fluctuation.

Firstly, as laser power was recorded on a per-shot basis the rasterising code was written to accept two thresholds as input variables. These thresholds were the lowest and highest acceptable laser powers for a shot to be written to the matrix as fractions of the distribution of laser power for the scan i.e. take only signals acquired for laser power $L(n)$ for n shots according to $\frac{1}{4}\bar{L} \leq L(n) \leq \frac{3}{4}\bar{L}$. An example laser-power histogram with user-defined thresholds is presented in Figure 4.3.

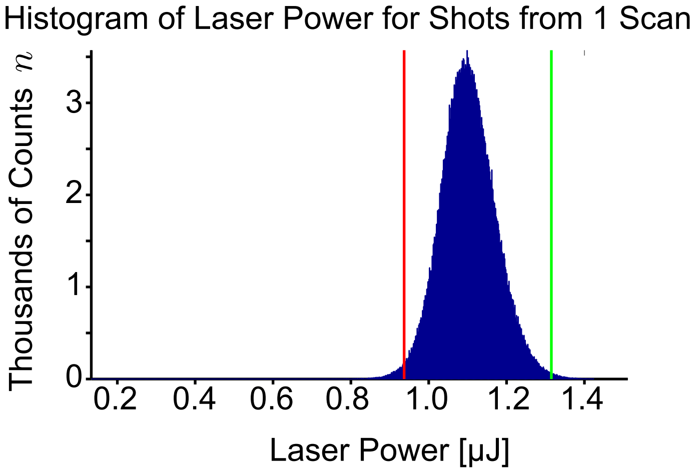

Figure 4.3: An example laser power distribution for one scan. The red and green lines indicate the lower and upper thresholds as defined by the user.

Secondly, the overwriting method was exchanged for an averaging-based method. In this approach Delaunay triangles were calculated for the predefined raster grid. Each shot was then summed into the triangle with the nearest vertex to it's true x–y position as found by a nearest-neighbour computation. In parallel to summing the shot to that triangle, a count-matrix was also iterated by one at the same index. Lastly, the total summed matrix was elementally-divided by the count matrix so as to average the contributions. This is illustrated with psuedo code snippet Algorithm 1. Note that the assignments indexing was, in reality, more complex as there is more than one sample per acquisition, and that this snippet is illustrative rather than comprehensive.

Algorithm 1 Assignment of Acquisitions to Raster Grid

```
procedure $outVol \leftarrow$ RasteriseData($inData$, $Grid$, $positionData$)
    $dt \leftarrow$ DelaunayTriangles($Grid$)
    $i \leftarrow$ nearestNeighbour($dt$, $positionData$)
    loop: $n \leftarrow$ 1:length($i$)
        $outVol(i(n)) \leftarrow outVol(i(n)) + inData(n)$
        $nCounts(i(n)) \leftarrow nCounts(i(n)) + 1$;
    $outVol \leftarrow outVol./nCounts$
```

4.3 Amplitude Criterion and Fibre-Motion artefact correction

Due to the fast scanning motion of the transducer-fibre assembly, the tolerances of the the central hole through the detector, and the transducer mounts, some vibration artefacts were noticed in early data sets acquired. This motion artefact is clearly seen in Figure 4.4. Here, a mouse ear was scanned with OR-OAM for a region of 4.5x4.5 mm, and the figure shows three top-down maximum amplitude images in z. In Figure 4.4A data was only assigned to the raster volume if the stage was moving from left to right. Similarly, in 4.4B data was only taken when the stage was moving right to left. The primary artefact is visible in 4.4C, where data was assigned regardless of the direction the transducer was moving. This primary artefact is clearly observable as a doubling of structures in the x-axis. The main cause for the artefact was found to be the deflection of the fibre due to it's inertia and the resistance to motion offered by the viscosity of the water i.e. as the stage accelerated the fibre tip in the water would lag the motion slightly; the mirrored action was seen under deceleration. As only the x-axis was fast-scanning no mirroring or similar artefact was noticed in the y-axis.

To address this issue from the post-processing perspective a cross-correlation based algorithm was implemented. This algorithm built the one direction volumes as in Figure 4.4A-B, then the cross correlation was taken between the two for each y-position. The corresponding delay was then found for the maximum cross-correlation value, and one volume shifted before being summed into the other. The results of this are presented in Figure 4.5, alongside an image of the cross-correlation map for that scan.

The main benefit of using signals acquired from both directions of motion was an effective increase in the per-pixel averaging. This can be seen when

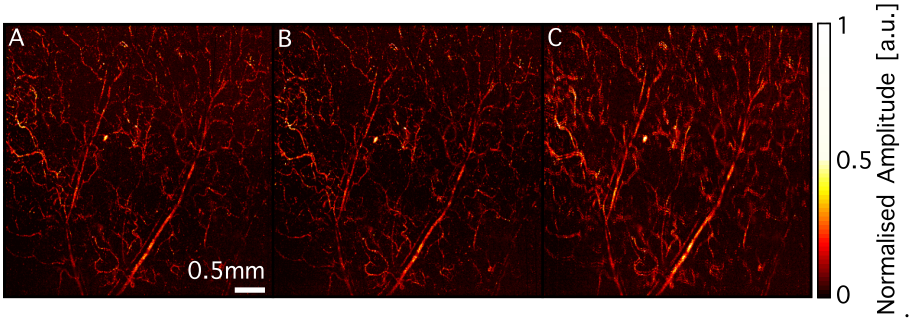

Figure 4.4: An optical resolution optoacoustic microscopy image of a mouse ear (4.5x4.5 mm), with acquisitions used while the transducer-laser assembly moved from (a) left-to-right only, (b) right-to-left only, and (c) in both directions.

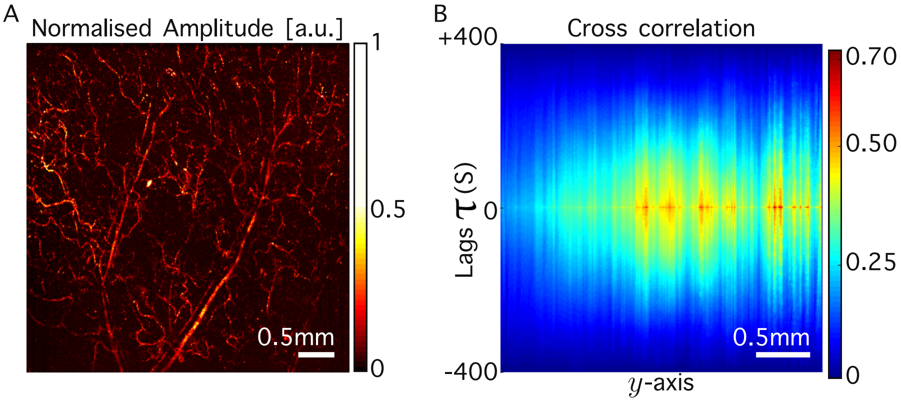

Figure 4.5: A: An optical resolution optoacoustic microscopy image of a mouse ear (4.5x4.5 mm), with acquisitions used while the transducer-laser assembly moved in both directions and fibre drift was corrected for via a cross-correlation algorithm; B: cross-correlation against lag τ at each y-position.

inspecting one signal from a one-way volume against the same position in the correlation-corrected two-way volume, as is presented in Figure 4.6. The RMS SNR was calculated for each signal, and is found in the Figure as annotations of 27 dB and 28 dB for the one-way and two-way volumes, respectively. This improvement is slight, though that is to be expected. Recall that the rasterised grid was defined first, and the speed of the stages and the pulse repetition frequency of the laser were then calculated so as to achieve this resolution. As such, the total number of averages for any given position within the final rasterised volume may be as low as 1 shot at the centre of the volume, where shot density is lowest. For the two signals presented here the one-way signal is from a single contribution (no averaging), whereas the two-way signal is the average of 4 contributions. This is because during left-to-right motion, only one acquisition was near this raster position, whereas in right-to-left motion this position was the nearest-neighbour location for 4 acquisitions. Furthermore, with such a slight difference the increase of just 1 dB is readily understandable. By extension, if the raster grid were to be lowered in resolution, more signals would be assigned to each pixel. This would see an increase of SNR, but a decrease in resolution.

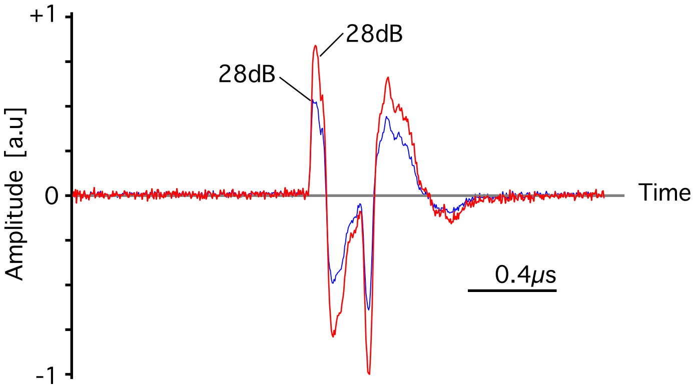

Figure 4.6: Time-domain optoacoustic signals from the previously presented mouse ear data. The optoacoustic signal from the one-way volume (blue) is annotated with an SNR of 27 dB, and the signal from the two-way volume (red) with an SNR of 28 dB.

One constraint of this coherence shifting method is that the data needs to contain very well spatially defined structures before it can be applied. Otherwise the coherence measure is simply too noisy and the shifts applied thereafter seemingly random.

4.4 Experimentation

An example of AR-data for a mouse brain through a hole in the skull is presented in Figure 4.7 as two MAPs. In Figure 4.7A, the data is colour-coded for amplitude, whereas in 4.7B it is colour-coded for depth. The AR data presented here is the result of an early implementation of a synthetic aperture focusing technique (SAFT), which is discussed at length later, and has been high pass filtered. The scan was made using the liquid light-guide,positioned above the mouse, to provide very broad, static illumination; the scan size is 5x5 mm with a target resolution of 20x20 μm steps.

An example of OR-data for a juvenile zebrafish is presented in Figure 4.8 (12 mm developmental stage - 35 dpf). Again, in Figure 4.8A, the data is colour-coded for amplitude, whereas in 4.8B it is colour-coded for depth.

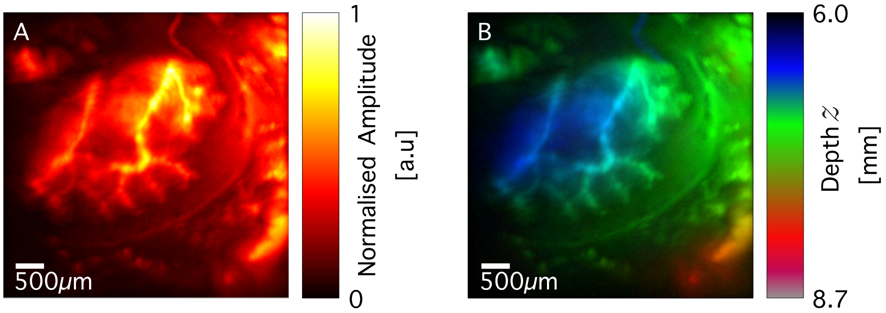
A
500μm
1
0
Normalised Amplitude [a.u]
B
500μm
6.0
8.7
Depth z [mm]

Figure 4.7: Maximum amplitude images of mouse brain through a hole in the skull; (A) colour-coded for amplitude, (B) colour-coded for depth.

The scan was made with the PCF, and covers a scan range of 3x12 mm, which required 55s to acquire.

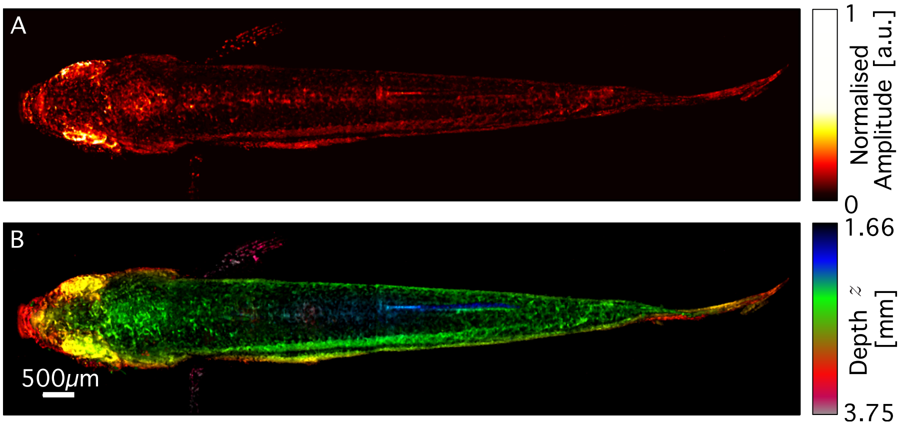
A
1
0
Normalised Amplitude [a.u.]
B
500μm
1.66
3.75
Depth z [mm]

Figure 4.8: Maximum amplitude images of an *ex-vivo* juvenille zebrafish; (A) colour-coded for amplitude, (B) colour-coded for depth.

4.5 Discussion

The AR data presented in Figure 4.7 shows superficial brain vasculature after removal of part of the covering skull. Recall from the previous chapter that an important parameter in AR-OAM scanning is the location of the acoustic focus within the target volume. For this experiment it was expected that the incident fluence would not be sufficiently penetrating to yield strong signals at depth within the highly optically scattering and attenuating brain. Therefore, the acoustic focus was positioned at the surface of the brain for two reasons. Firstly, to have maximum detection-sensitivity and excitation-potential at the same region with the goal of acquiring an image of superficial vasculature with good SNR and intrinsic lateral resolution. Secondly, it was hoped that scattered illumination and out-of-focus detection would give optimal conditions for SAFT-based post-processing to recover any large structures at depth. As is apparent from Figure 4.7B, the scan was successful in the first objective, as the structures most clearly visible lie close to, or just superficial of, the acoustic focus at around 6.8 mm. Unfortunately, as was expected little to know structures were visible even after post-processing. This is largely believed to have been due to the low optical fluence, transducer sensitivity, and transducer resolution at those depths.

The OR data presented in Figure 4.8 shows the scan of a full *ex-vivo* juvenile zebrafish; this volume is not post-processed with any SAFT based algorithms, with only some high-pass time domain filtering used to remove system noise. The primary difference to the AR data of the brain is that the peak signal amplitude and lateral resolution is dictated by the incident illumination. This is clearly seen in 4.8B, where the image is effectively of the surface of the fish through a 2 mm range of depths. Not surprisingly there is not significant information in the images beneath the surface. This is because after the illuminating beam has reached an optically absorbing point on the surface (thus generating the detected signal) it is significantly attenuated and also subjected to degree of optical scattering.

Overall the nature of the data sets presented in Figures 4.7 and 4.8 is not different than was discussed in the previous chapter i.e. the limitations of OR and AR imaging remain the same, and the same optimisation problems need to be solved while designing an experiment or study. What is different is the size of the volumes presented, and the time necessary to acquire them; the OR data, for example, required only 55s. Comparing this to the raster scan volumes presented previously, for which runtime was in the order of 1-2 hours, the advantages of the fast-scanning mode are clear. Perhaps most importantly, it allows for many large-area high-resolution scans to be made every hour; this is vital and already shown to be useable in performing time-critical biological studies [19].

Chapter 5

Pulse Echo Ultrasound Microscopy

Ultrasound microscopy is typically used for non-biological imaging purposes such as imaging of computer processors and in materials testing within the manufacturing industry. This is primarily because despite very good depth penetration, the practical applications for ultrasound microscopy within a biomedical context are limited primarily due to it's insensitivity to biological processes or markers. However, in the context of this thesis, readily coregisterable ultrasound data is of great use in complimenting the optoacoustic microscopy data.

5.1 Motivation

The primary initial motivation for acquiring pulse-echo ultrasound (PE-US) data volumes was to have an image of structural information of the scanning target on which optoacoustic data could be overlaid. For example, an ultrasound image of an intact mouse head would show the scalp, skull, and brain interfaces and any other changes of acoustic impedance; this could then be overlaid with optoacoustic information showing vasculature throughout the head. The seconday motivation was to provide structural information on the target being scanned. Namely, as a method to check whether signals were true optoacoustic sources, or simply an artefact from the acoustic propeties of the target as per Chapter 1.

One further use of an ultrasound mode was the location of microspheres in phantom experiments. As was shown in Chapter 3, having a larger structure to help locate microspheres is very useful. However, any optoacoustic-based marker, such as a suture, will typically need removing before scanning the sphere to avoid unwanted signals. Microsphere phantoms were always made in agar, which provided sufficient ultrasound contrast to water at the interface that by marking the agar surface orientation could be greatly simplified, and the time needed to locate spheres greatly reduced.

5.2 Ultrasound Generation and Acquisition

Thus far the development of the system has been focused on the passive detection of ultrasound waves generated through the optoacoustic effect. However, both of the transducers presented in Chapter 3.2 were also capable of being used to actively generate ultrasound. In the ideal case a spherical ultrasound transducer of infinite bandwidth provided with a high amplitude dirac-delta excitation pulse produces a dirac-delta acoustic wave which is inherently broadband and perfectly focuses at the centre of the sphere. However, in reality transducer geometry is a portion of a sphere, and has some limited bandwidth. Here the pulse-generator used was capable of delivering square-waves of up to 180V amplitude and a rise time of <4ns (5073PR Olympus Europa GmbH, DE), which was sufficiently impulsive to excite the full bandwidth of both transducers. Overall, as the properties of the transducers that affect their ability to passively detect and spatiotemporally-resolve ultrasound sources are the same as those which dictate their performance as an active element, visualisation of their performance with respect to ultrasound generation is the same as presented previously (Fig. 3.5, 3.6, 3.8, 3.9).

Although the scanning mechanics and protocol remained unchanged, the data acquisition signal-chain and code needed modifying for the scanning PE-US mode; a system schematic for the PE-US mode is presented in Figure 5.1. Firstly, the pre-amplifier used in optoacoustic scans was replaced by the ultrasound pulser. Intuitively this was necessary as the preamplifier had no means by which the high amplitude excitation pulse could pass through to the transducer unimpeded and without itself being damaged. Usefully, the pulser was capable of operating in both the excitation and collection signal path, as it also contained an amplifier. Thus, the absence of the preamplifier was not problematic. Secondly, the sensitivity of the data acquisition card had to be changed to accomodate the higher amplitude signals it was expected to digitise. Lastly, the data acquisition code was modified to account for the temporal difference in the arrival of signals. Namely, optoacoustic waves were generated nearly instantaneously throughout the target media and signals were recorded after the time of flight from the optical absorber to the transducer; wheras PE-US signals were recorded after twice the time of flight from the transducer to an acoustically reflective interface. This is most clearly stated when mapping the signal volume into a cartesian distance volume as

$$\begin{aligned} z &\approx c_0 t \qquad \text{(optoacoustic)}, \\ z &\approx c_0 t/2 \qquad \text{(pulse-echo)}. \end{aligned} \tag{5.1}$$

Overall, the PVDF detector was found to be the best performing of the two transducers for use in the PE-US scan. Again, this was due to its superior available bandwidth and the cleanliness of its EIR.

5.3 Dual-Mode Acquisition

The logical extension of a single system capable of PE-US and OAM scanning is to scan a target in both modes sequentially with no inter-scan delay. The simplest instance of dual-mode operation was when performing raster scans. However, two sequential fast-scans would most certainly be faster than a single raster scan. Such a pair of scans would be immediately coregisterable and thus allow useful insights to be gained both post-experiment, say structural parameters for data analysis, or immediately during the experimental session, such as checking the current scan volume is correctly positioned or to check for the presence of an unwanted air pocket.

To make such a scan possible the process of switching the operating modes of the system needed significant optimisation so as to minimise the time between the two scans. This was largely done through modifying the operating code for the system to maintain variables common to the two scans, whilst derived variables and system parameters would be updated automatically. The remaining bottle-neck was physically switching the transducer connection from the pre-amplifier used for optoacoustic scans to the pulser-amplifier used in the PE-US scans. This was minimised to a few seconds through securing the relevant cables and connections in close proximity to one another. Future modification may consider a software-controllable switch, such as a relay, though the sensitivity of this connection to electrical noise cannot be understated, and as such great caution should be exercised.

5.4 Hybrid PE-OAM

One future goal for the system is hybrid mode acquisition. Hybrid-mode acquisition is defined here as acquiring both an optoacoustic and a PE-US signal for every scanning position. The advantage of this over two sequential scans is that in a time-sensitive biological context, both an optoacoustic and a coregisterable PE-US volume can be acquired in the shortest possible timeframe. Although modification of the signal chain and data acquisition code for the PE-US mode were reasonably simple to make, modifying the system to permit on-the-fly dual-mode scans posed a significant obstacle.

In optimising the system for dual-mode acquisition the first major obstacles to hybrid operation became clear - the necessary switching of hardware and data acquisition variables. Firstly, the optoacoustic data would have to be acquired through the same acquisition channel as the PE-US data, be-

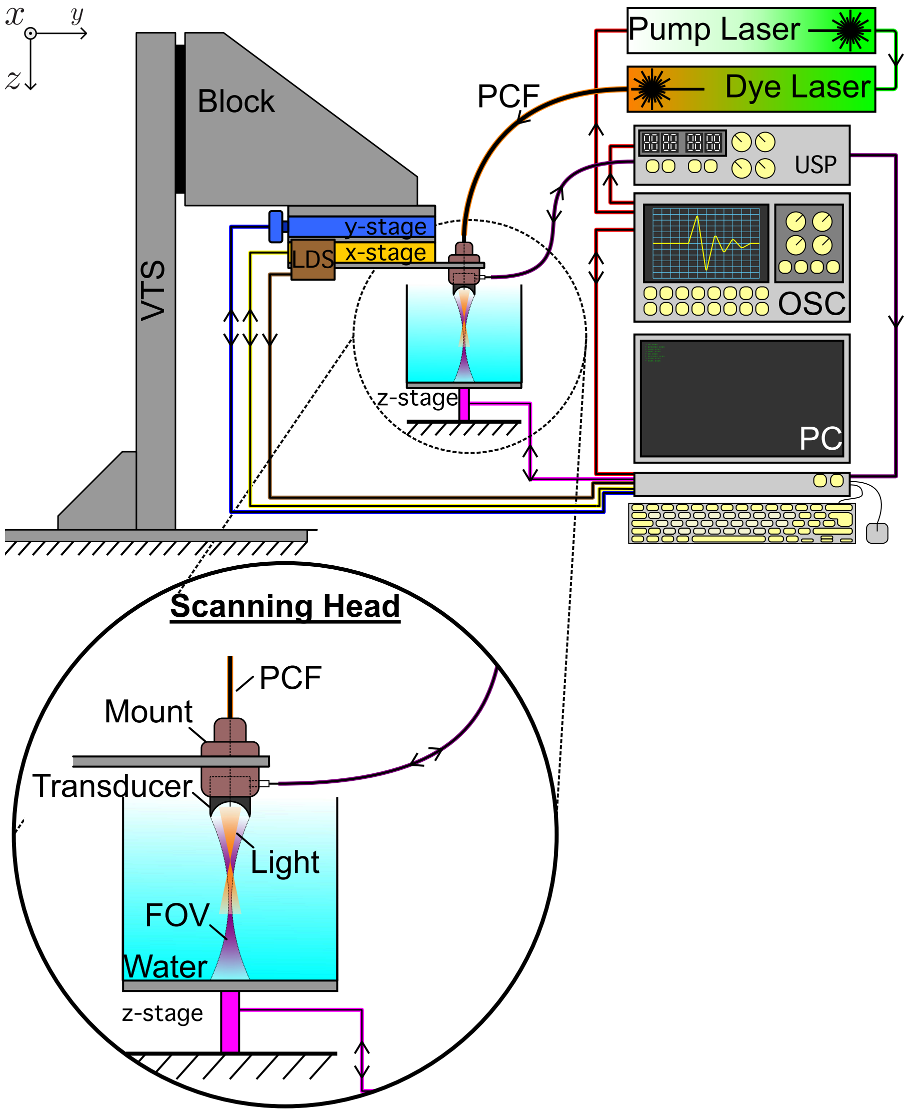
x
y
z
Block
VTS
PCF
Pump Laser
Dye Laser
USP
OSC
PC
y-stage
x-stage
LDS
z-stage
Scanning Head
PCF
Mount
Transducer
Light
FOV
Water
z-stage

Figure 5.1: A schematic of the ultrasound and optoacoustic scanning microscope. VTS is the coarse large-range manual vertical position stage. The trigger signals from the oscilloscope (OSC - red) fired both the pump laser and started the data acquisition cards on the PC. The $x-$, $y-$ and $z-$ stages (red, yellow, pink) were controlled from inside the scanning routine on the PC; the signal from the laser distance sensor (brown - LDS) was used to calibrate the x-stage motion. Detected ultrasound signals were passed to the PC via the ultrasound pulser (USP - purple); the pulser was also used to generate ultrasound waves from the transducer. Water was necessary as the transducers are water-coupled. The inset figure shows how the field of view (FOV) of the transducer (purple) and a the excitation light emitted by, in this illustration, a photonic crystal fibre (PCF).

cause swapping between the amplifier in the pulser and the standalone pre-amplifier would be impracticable. Secondly, the data acquisition card would need switching between expecting signals in the range of ±200mV and ±1V on a per-shot basis. An additional issue here would be that with changing of the dynamic range on the acquisition channel, the card would clear its data buffer, thus massively increasing runtime for the scan. Finally, the last major obstacle becomes clear in the context of the fast-scanning operation. Recall that in fast-scanning operation desired volume parameters were defined (resolution, region of interest, etc.) from which a scanning locus was computed. After the scan was complete, data was then rasterised into a cartesian volume based on metrics of the most appropriate location for each signal acquired. Additionally, recall that the PE-US and optoacoustic signals were acquired over different timeframes to account for time-of-flight and delay in triggering the laser to the laser firing.

To overcome these obstacles several modifications would have to be made to the hardware of the system. Firstly, the issues of different dynamic range and difference in time-frames could be solved by the inclusion of a second high-speed data acquisition card. With each card acquiring data for one scan-mode, then issues associated with reinitialisation, dynamic range, and memory buffering would be readily negated. Secondly, through better splitting of the excitation-detection signal-chain a pre-amplifier could be retained for the optoacoustic data.

5.5 Experimentation

In this section the results for three scans using pulse echo ultrasound are presented along with a description of what each experiment contained. The scans were all performed alongside optoacoustic scans. Additionally presented are the dual-mode OA-US data sets for two scans presented elsewhere in the thesis.

The first experiment was imaging through an intact mouse skull (scalp removed) with the PVDF ultrasound transducer and the fast-scanning system. With the skull placed at the acoustic focus ($\simeq$6.8 mm) total acquisition of the data set took approximately 55s for a 4.5x4.5 mm scan. The orthogonal MAPs for the scan are presented in Figure 5.2.

The scan clearly shows not only the location of the skull, but also the texture of the surface, the bregma, and the location of a remnant hair. These features are clearly annotated in Figure 5.2. The skull is a curved surface, and as such the entire skull did not lie within the focus of the ultrasound transducer. The effect of this is that as y increase the skull in Figure 5.2A becomes slowly blurred, while in 5.2B the amplitude decreases; the curved profile is apparent in 5.2(C). Also visible in Figure 5.2(B-C) is the surface of the transparent film which covers the mouse and ensures the water-coupling

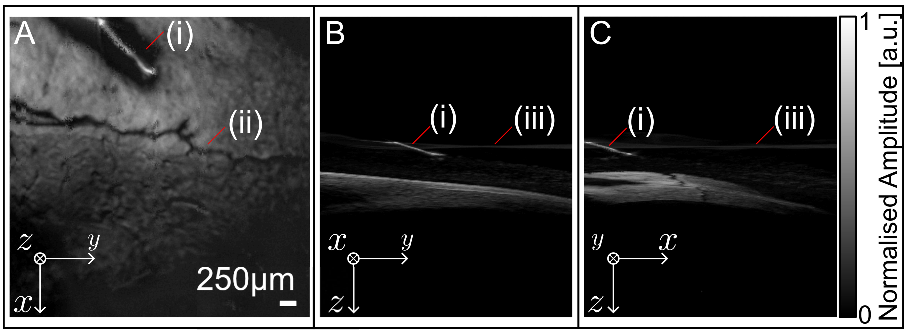

Figure 5.2: Maximum amplitude projections for a pulse-echo ultrasound image of a mouse skull; projections through (A) z, (B) x and (C) z. Annotations are of (i) a hair (ii) the bregma, and (iii) the transparent foil.

is achieved.

This first scan was part of a series of scans performed to try and achieve optoacoustic images of gold nano rod labelled cells injected in the striatum ≃2.5 mm deep of the skull. It was hoped that this would be possible through the intact skull, though until post-processing of the data after acquisition it would not be immediately apparent if this had ben successful. Consequently, to try and ensure results pertaining to that objective scans were also made with a mouse where a hole was drilled in the skull.

The second scan shows, again, the skull of a mouse at the focus with the scalp removed. This mouse though had the aforementioned hole in the skull, which is clearly visible in the pulse-echo ultrasound images presented in Figure 5.3; the annotated convention is maintained from Figure 5.2. This scan, again of 4.5x4.5 mm, also took ≃55s to acquire.

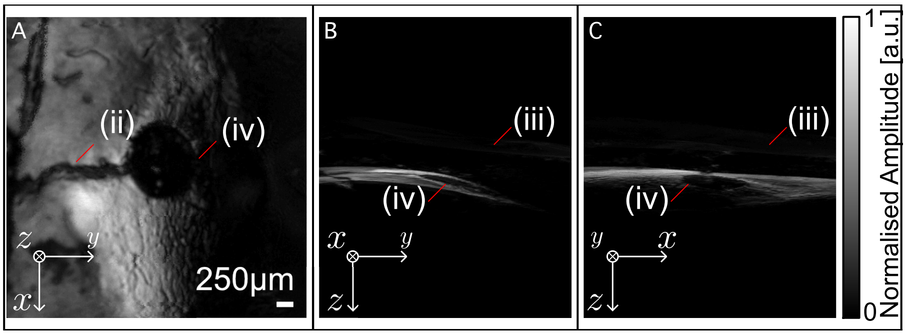

Figure 5.3: Maximum intensity projections for a pulse-echo ultrasound image of a mouse skull; projections through (A) z, (B) x and (C) z. Annotations retain the convention of Figure 5.2, and are of (ii) the bregma, (iii) the transparent foil and (iV) the hole.

The third experimental result shown here is the pulse-echo ultrasound of a mouse ear, for which orthogonal MAPs are presented in Figure 5.4. This scan was performed in conjunction with an optoacoustic scan, where the main purpose of the experiment was to acquire a data set demonstrating the capability of the fast-scanning system to acquire optical-resolution optoacoustic images; the same scan presented in Chapter 3. The PE-US scan was performed primarily to orientate the system and the sample so as to achieve a useful optoacoustic data set. A secondary objective was to have a coregisterable structural data set for the ear, thus giving greater insight into what is shown in the optoacoustic data set.

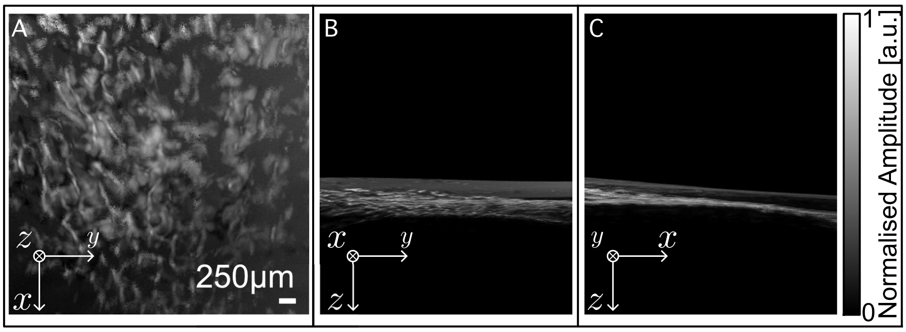

Figure 5.4: Maximum intensity projections for a pulse-echo ultrasound image of a mouse ear; projections through (A) z, (B) x and (C) y.

The most readily visible feature in Figure 5.4(A) is the arrangement of the cartliage and other tissue, while (B-C) shows that the ear was sucseffuly positioned with a near-parallel planar orientation relative to the scanning plane.

Lastly two coregistered dual-mode scans are presented. Firstly, an example of a coregistred data set is presented in Figure 5.5 with an overlay of the previously presented OR-OAM scan (Figure 4.5) and a PE-US scan (Figure 5.4) of a mouse ear. Secondly, Figure 5.6 presents a data set from the scan of a 12 mm developmental stage juvenile zebrafish. It shows an example of how a whole-volume PE-US scan may be performed so as to best select a subvolume to perform an OAM scan. In both Figure 5.5 and 5.6 MAPs for the PE-US data are shown, with the OAM data overlaid using a fixed degree of transparency.

As can be seen from these two data sets, due to the design of the system it is reasonably simple to coregister the data from an investigation, with PE-US providing valuable structural information, and OAM providing functional imaging.

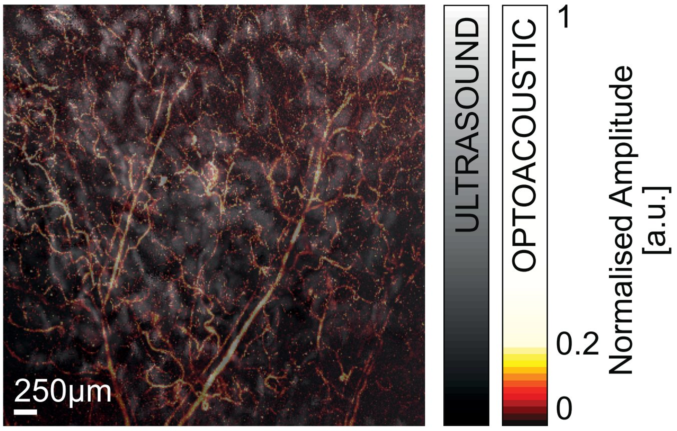
250µm
ULTRASOUND
OPTOACOUSTIC
1
0.2
0
Normalised Amplitude [a.u.]

Figure 5.5: The top-down maximum amplitude projections for an OAM image and a PE-US image of a mouse ear overlaid.

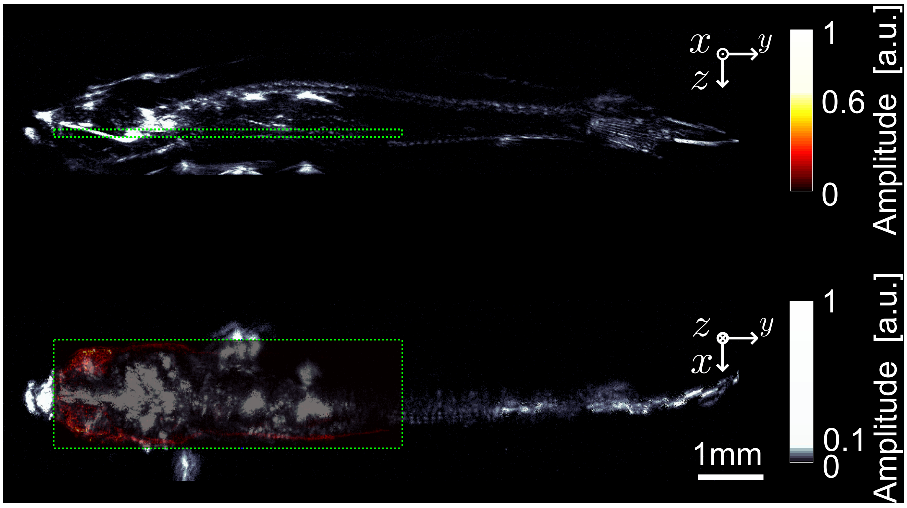
x
y
z
1
0.6
0
Amplitude [a.u.]
z
y
x
1mm
1
0.1
0
Amplitude [a.u.]

Figure 5.6: MAPs of scanning a juvenile zebrafish with (top) the PE-US mode of the system and (bottom) the OR-OAM mode. The green rectangle illustrates the subvolume for which the OAM data is overlaid.

5.6 Discussion

In optoacoustics it is very useful to have information about the structure of the imaging target. This is because, as was presented in Chapter 1, the changes in acoustic properties can yield artefacts in optoacoustic images. Therefore, the ability of the PE-US mode of the system to yield images, such as in Figures 5.2-5.4, is invaluable. Specfcialy, in neuroimaging the interstitial presence of the skull with respect to the brain and the scanning transducer poses a significant challenge. With this challenge in mind the PE-

US mode of the system has already been used in measuring and modelling the transmission function of murine skull [20], as is presented later in in Part II.

Part II

Effects of acoustic mismatches of the skull

The challenges of imaging through intact mouse skull and approaches to correction for its presence.

Chapter 6

Acoustic Effects of Murine Skull

The work presented in this chapter was published in the Journal of Biophotonics & Biology (2016) [20].

6.1 Introduction

While OR-OAM can achieve sub-micron spatial resolution, its potential as a volumetric imaging modality for neuroimaging in mice is limited by its severely restricted depth penetration. As a result, studies are commonly performed in young mice [21], through thinned skulls [22] or otherwise concentrate on demonstrating high-resolution functional imaging performance in a thin layer of pial vasculature immediately adjacent to the skull [23]. Alternatively AR-OAM can be reach significantly greater depths, although, the presence of an acoustically mismatched skull was previously shown to also significantly deteriorate imaging performance in this modality [24], [25]. This is in contrast to a previous study of a rat skull [26]. Here a quantitative description of the transmission characteristics of optoacoustically generated acoustic waves travelling through the mouse skull is presented, with the aim of providing insight into how the skull affects optoacoustic imaging performance for both AR-OAM and OR-OAM systems.

6.2 Experimentation

In order to analyse and quantify effects of the murine skull in various illumination and detection scenarios, the optoacoustic microscopy system presented in Part I was used. For data acquisition in pure acoustic resolution mode, broad and unfocused illumination was applied to the imaged object via the liquid light guide or multimode fibre, providing side-illumination (perpendicular to the acoustic axis) as shown in Figure 6.1. To achieve optical resolution performance the system was operated as per the PCF and GRIN-lens configuration.

To determine the skull-induced deterioration in the acoustic resolution performance, an agar phantom was prepared containing a single 10 μm microsphere. The phantom was then oriented so as to place the microsphere in the focus of the ultrasonic transducer. Two data sets were then acquired, once with and once without a piece of excised adult mouse skull (230 μm thick) which was placed between the phantom and the transducer and coupled using distilled water. To ensure similar conditions to those found in-vivo, the skull was kept hydrated between the surgery and measurement time points.

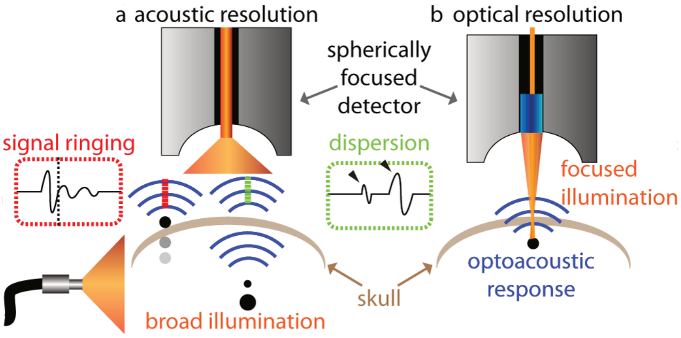

Figure 6.1: Schematics of the experimental approaches. (a) AR-OAM configuration using broad illumination. Optoacoustic sources located just above the skull generate ringing artifacts and shadow signals due to reflections at the skull surfaces (vertical line in the blue box denotes temporal position of the skull). Acoustic dispersion of the skull creates frequency dependent attenuation with higher frequency signals (generated by smaller objects) experiencing stronger attenuation compared to lower frequency content (generated by larger objects), see green box. (b) OR-OAM configuration using focused illumination. Focused light is scattered by the skull, broadening the excitation beam and affecting the lateral resolution performance.

In order to examine the effects the skull might have on the microscopy system's actual imaging performance, scans were made of several sutures (50 μm diameter) embedded at different depths in scattering, tissue-mimicking agar phantom (1% intralipid). High-averaging AR-OAM raster scans were performed twice. Once with and once without a piece of excised skull placed above the central crossing of the sutures, which covered almost the entire phantom diameter. Post acquisition the out-of-focus signals were further recovered using a synthetic aperture-focusing algorithm WSAFT, which again is presented later in Part III.

Finally, in order to accurately analyse the applicability of optoacoustic microscopy for non-invasive imaging of fine brain vasculature in OR mode, a perfusion fixation procedure [27] was adapted for labelling the brain's vasculature ex-vivo. The procedure thus enables studying the effects of the murine skull independently from potential artifacts related to in-vivo imaging, such as motion. Adult CD1 mice were used for perfusion. The animals were sacrificed with an overdose of ketamine and xylazine, followed by IP injection of 200 heparin units, and then perfused through the left ventricle with heparinized PBS (5 units heparin/ml) using a perfusion pump (behr Labor-Technik GmbH, Germany). The perfusion agent was then changed to a 1:4 mixture of Pelikan 4001 ink (Pelikan Holding AG, Switzerland) to agarose, prepared using 1.5% of low gelling agarose (SeaPrep, Lonza, Switzerland) in PBS. Following the mixture's complete perfusion, the agarose was allowed to cool and set for 45 minutes at 4°C, thereby fully replacing the circulating blood with highly absorbing ink while the agarose retains the integrity of the solution and the structure of the vasculature (Fig. 6.4g). Furthermore, the speed of sound difference of water and agarose is negligibly small, thus adverse effects of the perfusion method were minimised. The skull was exposed and prepared for imaging by either leaving it intact, thinning it using a high-speed handheld drill (IDEAL Micro Drill, Cellpoint Scientific, USA), or removing it completely. Acquisition time was kept low at approximately two minutes for the entire 3D volumes (ROI 10x7 mm), with PBS being used as the coupling medium to diminish any negative effects of distilled water on the biological tissue.

6.3 Results

The results of the microsphere experiment presented in Figure 6.2 show that the skull disperses the optoacoustically generated ultrasound wave and effectively acts as a low-pass filter. As higher frequencies suffer greater attenuation, the peak of the attenuated signal becomes broader and lower in amplitude when compared to the non-attenuated signal (Figure 6.2b). The axial FWHM of the Hilbert-transformed signals, governed by the acoustic resolution, amounts to 35 ns (53 μm) and 62 ns (93 μm) for the non-attenuated and attenuated case, respectively. The frequency-dependent attenuation (or insertion loss) of the skull was subsequently calculated by dividing the Fourier transformed optoacoustic signals detected with the skull by those detected without, demonstrating significant attenuation of high frequency signal components by the skull (Fig. 6.2a).

The microsphere acts as an ultrasound point source and thus the incident acoustic pressure on the skull arrives at a wide range of angles. Solid bodies of finite size support guided waves (leaky Lamb waves and Scholte-Stoneley waves for plates embedded in a fluid), which are highly dispersive [28]. Thus, the waves transmitted through the skull suffer not only frequency but also angle-dependent filtering. Eventually, the transmitted waves are detected

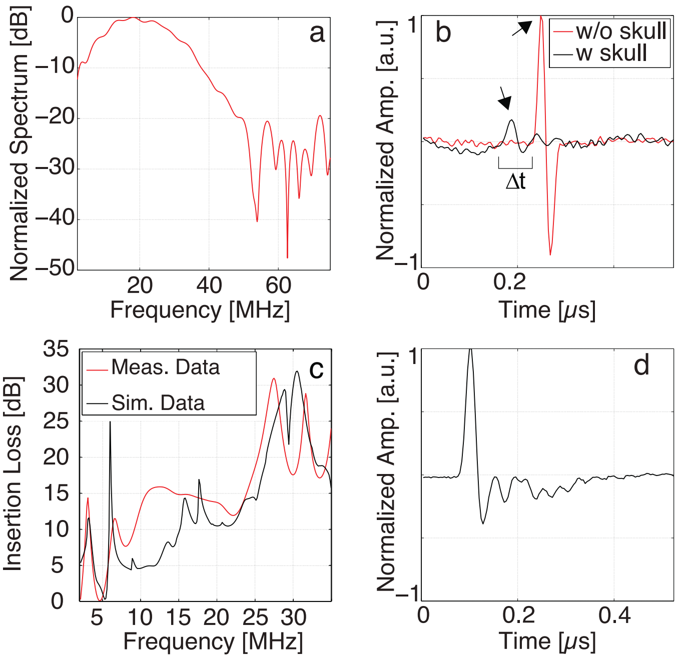

Figure 6.2: Results of the microsphere experiments demonstrate acoustic dispersion and ringing effects of adult murine skull. (a) Normalised US frequency spectrum of the signal of a single 10 μm microsphere excited with a nanosecond laser pulse and measured with a ultrawideband PVdF transducer. (b) Optoacoustic signal traces generated in the presence and absence of the skull. The attenuated peak is lower in amplitude and broader when compared to the non-attenuated peak (marked by arrows). The signal shift is labeled Δt. (c) Simulated (black) and measured (red) frequency dependent attenuation (insertion loss) of the skull showing a strong increase with frequency. (d) Time domain signal of a microsphere placed in the immediate vicinity of the skull surface clearly shows signal ringing due to reflections at the skull-tissue interface.

using a spherically focused detector, which covers a range of angles from 4 up to 25 deg. All these factors explain why the insertion loss is not a monotonic curve. This complicated behaviour can be simulated using a simple homogeneous plate model [28] and approximating the insertion loss, IL as being only produced by the skull under perfect alignment conditions as

$$IL(\omega) = \frac{\int_{\theta_1}^{\theta_2} T(k_0 \sin(\theta), \omega) \sin(\theta) \mathrm{d}\theta}{cos(\theta_1) - cos(\theta_2)}, \tag{6.1}$$

where k_0 is the wavenumber in the fluid, ω is the angular frequency and T corresponds to the transmission coefficient of the plate model. By using measured and literature values for the plate model (density of 1800 kgm^{-3} [29], longitudinal and shear speed of sound of 2900 ms^{-1} and 1444 ms^{-1} [30] and a thickness of 245.5 μm), and evaluating Eq. (6.1) between the angles covered by the transducer yields the black curve in Fig. 6.2c. Not only can the general trend can be well explained by this model, but also the transmission maximum near 5 MHz, which is produced by thickness-dependent leaky Lamb modes of the skull acting as a solid plate [28]. As the frequency increases, the agreement between experimental and predicted curves becomes mainly qualitative, with the order of magnitude remaining well in agreement for frequencies above 25 MHz.

As a consequence of these frequency-angle-dependent filtering effects, it can be observed that the skull introduces both time shifts and ringing artifacts in the arrival of the measured optoacoustic signals. The speed of sound is significantly higher in bone as compared to water [24], thus, optoacoustic signals travelling through the skull will arrive earlier at the detector surface as compared to signals travelling the same distance through water alone. Indeed, the time shift as seen in Fig. 6.2b is calculated to be Δt=3 ns . The speed of sound in the skull is given by

$$c_{sk} = \frac{c \cdot w}{w - c \cdot \Delta t}, \tag{6.2}$$

where w is the skull's thickness and c is the speed of sound in water. Using the measured thickness of the adult murine skull (230 μm), the optoacoustically determined speed of sound in the skull was calculated to be 2828 m/s, closely corresponding to the 2800 - 2900 m/s range found in literature [31], [24]. Moreover, when a microsphere absorber is placed in the immediate vicinity of the outer skull surface, ringing is created due to reflections of the generated optoacoustic signal at the two skull surfaces, which could be mistakenly interpreted as shallow absorbers inside the brain (Fig. 6.2d). Recall, this ringing behaviour was described in Chapter 1.

Figure 6.3 shows volumetric optoacoustic images for the embedded 50 μm suture phantom experiments, colour-coded for depth. To compare the two scenarios, lateral FWHM measurements were estimated at the positions marked by white arrows (Fig. 6.3a). The FWHM only increases by 13%

on average when the skull fragment obstructs the transducer's view. Such minor broadening of 50 μm diameter structures when imaging through the skull is generally expected since absorbers of this size emit optoacoustic responses at much lower frequencies as compared to the 10 μm sphere. In comparing Fig. 6.3b to 6.3a, it becomes apparent that the reconstructed sutures also exhibit minor irregularities (yellow arrows), which might be attributed to the local refraction effects with the curvature and porosity of the skull possibly influencing the appearance of the reconstructed features.

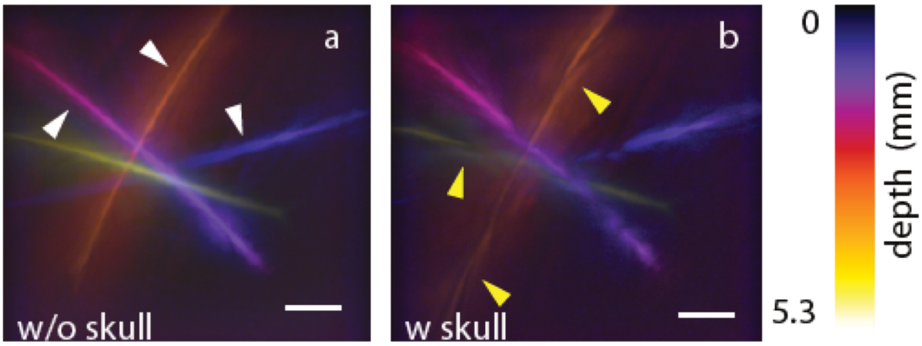

Figure 6.3: Effects of acoustic attenuation on imaging performance in the AR mode. (a) Three-dimensional optoacoustic image (color-coded for depth) of four absorbing sutures arbitrarily arranged inside tissue-mimicking scattering agar phantom. (b) The corresponding image acquired in the presence of skull. Scale bars correspond to 1.5 mm. Yellow arrows mark irregularities in the skull measurements. White arrows mark the position of FWHM measurements: 365 μm, 261 μm, 210 μm and 402 μm, 308 μm, 236 μm in (a) and (b) respectively.

Even though the brain vasculature is clearly visible in MAP images acquired through the intact skull (Fig. 6.4a), the fine capillary structure is not visible. When a partial cortical window is created by thinning the skull, both acoustic attenuation and photon scattering are locally reduced and finer vasculature becomes visible in the region of the thinned window (Fig. 6.4c). Naturally, the finest capillary structures are visible when no bone is obstructing the view of the transducer (Fig. 6.4b). As a qualitative measure of the effective useable lateral resolution, the FWHM for exemplary small visible vessels was calculated for all the three cases and were found to be 40.5 μm, 29.4 μm and 21.8 μm for the intact skull, thinned skull and excised brain, respectively. Figures 6.4e and6.4f show the effects of the skull in imaging biological targets in pure acoustic resolution mode, prepared as above. Therein, a slice of the axial FWHM of an exemplary vessel reduces from 59 μm to 49.8 μm upon removal of the skull. Lateral FWHM decreases from 852.3 μm to 632.8 μm.

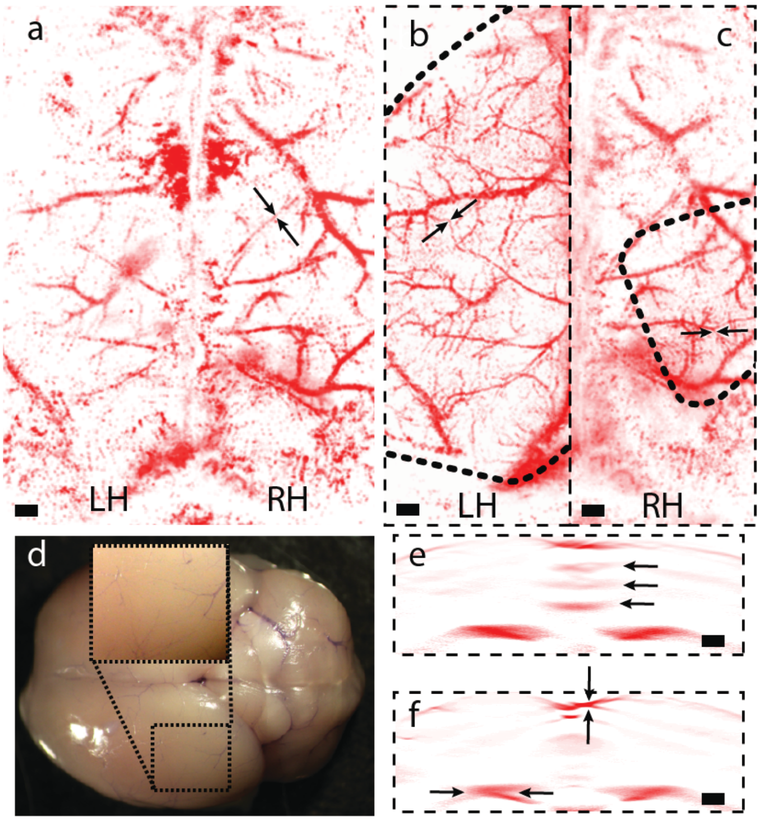

Figure 6.4: Murine skull affects the effective lateral resolution performance in OR-OAM scans of biological targets. MAPs of OR images of the perfused brain recorded through an intact skull (a), thinned skull (c) and without presence of the skull (b). Dashed lines mark the area where the skull was thinned (c) or removed (b). (b) and (c) each show one hemisphere (LH: left hemisphere, RH: right hemisphere) of the whole brain depicted in (a). A two-dimensional slice of AR data of a perfused brain through the intact skull (e) and with the skull removed (f). Arrows in (f) denote the positions of FWHM measurements. A photograph of an excised mouse brain, perfused with a mixture of agarose and ink, is shown in (d). Scale bars are 375 μm.

6.4 Discussion and Conclusions

In conclusion, it has been shown how the adult murine skull affects the effective lateral and axial resolution in non-invasive OAM studies, which may limit the capacity for transcranial imaging of small capillary structures in deep brain. The insertion loss of a piece of skull was determined for the first time using optoacoustically generated signals. A simple approximation using a homogeneous solid plate model is able to explain most of the features of the insertion loss observed experimentally. Discrepancies between the experiments and the model may be attributed to that fact that the skull is not a homogeneous solid plate but rather an inhomogeneous layered structure of compact and spongy bone tissue. However, good qualitative agreement has been found even without considering absorption within the porous region of the skull. This is the first time that solid-plate-like behavior has been observed in a skull, including high transmission peaks due to leaky-Lamb waves thanks to the usage of a broadband transducer and the relatively flat shape of the murine skull. The skull's acoustic low-pass filtering effects limit the resolution in all forms of OAM; however, in the special case of OR-OAM, the blurring of the cortical vasculature in the lateral direction is not solely attributed to the frequency-dependent acoustic attenuation but also to the light scattering properties of the cortical bone, which would therefore reduce the effective lateral resolution in future non-invasive in vivo experiments. The additional image degradation can be attributed to reflections at the skull-tissue-interface experienced by strong optoacoustic sources inside and on top of the skull; where the resultant time-domain ringing conceivably masks brain vasculature located below the skull. Measures such as skull thinning, cortical windows and using infant animals with thinner skulls may assist to reduce the skull-related effects, yet some of these methods may compromise the non-invasive nature and versatility of the imaging studies.

Chapter 7

Broadband Acoustic Properties of a Murine Skull

The work presented in this chapter was published in the journal Physics in Medicine & Biology (2016) [29].

7.1 Introduction

As was previously shown, skull bone represents a highly mismatched and dispersive barrier for the propagation of high frequency ultrasound. To this end, applications involving one-way ultrasound transmission through the skull, such as transcranial focused ultrasound surgery [30], blood brain barrier opening for drug delivery [31], ultrasound neurostimulation [32], and optoacoustic neuroimaging [33], have primarily been proven successful in overcoming this barrier. Yet, accurate knowledge of the skull's acoustic properties is a prerequisite for attaining high spatial accuracy in transcranial therapeutic and imaging applications [34].

Acoustic characterization of the skull has been initially performed using a focused transducer with small numerical aperture and a hydrophone to measure the insertion loss of human skulls between 0.25 and 2 MHz [35]. Most studies that followed were performed in the context of therapeutic high-intensity focused ultrasound (HIFU) applications in humans. However, these use of narrowband ultrasound transudcers and X-ray computed tomography (XCT) or magnetic resonance images of the skull to gain structural information. Some examples of such studies are using a Fourier propagation approach to attain transcranial ultrasound focusing [36]; development of a three-layer fluid model for narrowband phase-only simulations of transcranial wave propagation [37]; finite differences time domain (FDTD) models used to simulate transcranial wave propagation in three dimensions [38], which used XCT data, but ignored shear waves or mode conversion; a FDTD model that considered shear waves and mode conversion in addition to longitudinal waves in 3D [39], this time using μXCT data; [40] considered shear waves though neglected multiple reflections within the skull due to high attenuation.

The skull transmission dispersion can be potentially measured directly using established ultrasound plate characterisation techniques [41]. However, employing such techniques for measuring small-sized, partially-curved and non-homogeneous samples such as the murine skull remains a challenge. More recently, point-wise pulse-echo ultrasound measurements developed for human skull [42] have attained accurate measurements of thickness and longitudinal speed of sound, albeit relying on normal incidence orientation of the skull and separability of reflections between the different skull layers. The longitudinal speed of sound and attenuation at multiple discrete frequencies are reported in [43].

Overall, the existing methods for characterisation of the skull rely on assumptions of narrowband ultrasound transmission through planar surfaces or otherwise only consider plane waves or normal incidence, such as in Chapter 1. Some of these assumptions do not hold true for many real biological applications. A typical skull is also expected to effectively act as a highly mismatched solid plate that may additionally support the propagation of guided waves, such as the highly dispersive leaky Lamb waves, when embedded in a fluid [44]. Thus, the waves transmitted through the skull suffer not only frequency- but also angle-dependent filtering. The first confirmations of this approximation were presented in Chapter 6. As optoacoustic microscopy sees the generation of potentially ultra-wideband acoustic waves that can be incident upon the murine skull at any geometrically feasible angle, the necessity of developing a universal skull-characterisation strategy is clear.

Any universal strategy for skull-characterisation would therefore consist of measuring insertion loss using a broadband point-source and detecting the signals with the actual detector configuration optimised for the desired application [45]. Notwithstanding that cavitating microbubbles have been used as a point source for time reversal skull aberration correction in narrowband conditions [46], the use of black microspheres as an optoacoustic point source are ideal for this task, as per Chapter 3.2. Presented here is a proposed measurement and simulation framework for extracting geometric and elastic parameters of the murine skull represented via a skull transmission model. As a first approximation, and in order to show the potential of the proposed methodology, the transmission coefficient of a homogeneous isotropic solid layer embedded in a fluid was used. The modelling was facilitated by PE-US measurements of the skull orientation.

The key concepts used in this chapter are the angular-spectrum dependence of the transmission coefficient of the solid layer, the use of a plane-wave expansion to propagate the point-source to said solid layer, and the use of convolution to multiply the source and plate responses in the reciprocal space frequency domain [47], and forward propagating that result using the Fourier transform [48].

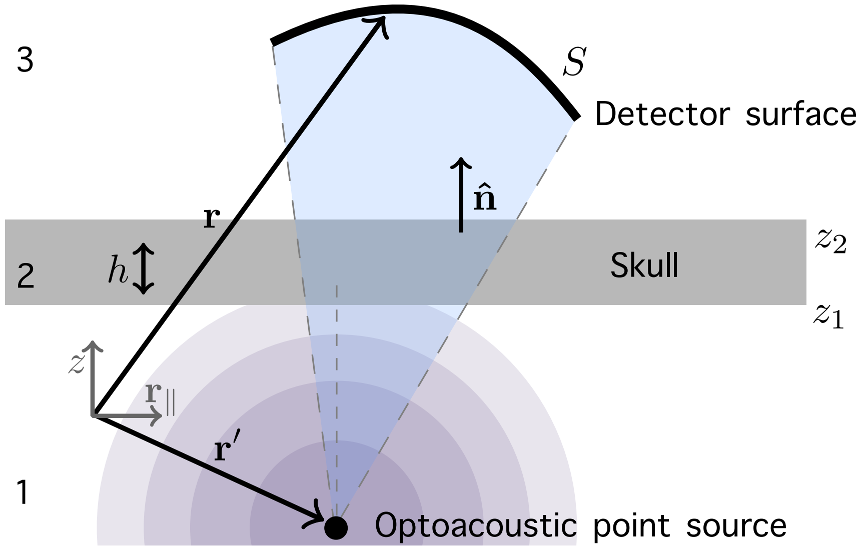

Figure 7.1: Geometry of the proposed method for the measurement of the skull insertion loss. The space is divided into three regions. Broadband ultrasound waves generated by an optoacoustic point source impinge at the skull of thickness h and surface normal vector $\hat{\mathbf{n}}$. The transmitted wave reaches the detector's surface S. The acceptance solid angle of the spherically focused detector is indicated by dashed lines.

7.2 Theory

7.2.1 Transmission through a fluid-loaded solid layer

As depicted in Fig. 7.1, the model for estimating the acoustic properties of the skull consists of broadband ultrasound waves generated by an optoacoustic point source, which are transmitted through the skull and detected by an arbitrary transducer surface. In the particular case of a spherically focused detector, its solid angle of acceptance is indicated by the dashed lines. The transmission coefficient of a flat solid plate of thickness h immersed between two fluids can be calculated using plane waves for an arbitrary angle of incidence. If the plate is homogeneous and isotropic, the calculation is reduced to a two-dimensional problem [49]. As shown in Fig. 7.2, the space is divided into three regions $j = 1, 2, 3$; each having different elasto-acoustic properties characterized by the density ρ_j and the sound wave speed c_{vj}, where v represents either longitudinal (ℓ) or transverse (t) waves. In the case under study, media 1 and 3 are assumed to be fluids and therefore only $c_{\ell 1}$ and $c_{\ell 3}$ are considered. The acoustic field in regions 1 and 3 is expressed as a plane wave potential ϕ which is a solution of the Helmholtz equation for the angular frequency ω. When time dependence is expressed via $\exp(-\mathrm{i}\omega t)$, ϕ is related to the pressure as $p = \mathrm{i}\omega\rho_j\phi_j$. Region 2 can be described using Stokes-Helmholtz decomposition of the displacement vector $\mathbf{u}_2 = \nabla\xi_2 + \nabla\times\zeta_2$, where ξ_2 and ζ_2 represent longitudinal and transverse plane waves, respectively. The wavenumbers $k_{vj} = \omega/c_{vj}$ define the wavevectors $\mathbf{k}^{\pm}_{vj} = k_{vj}\left(\sin(\theta_{vj})\hat{\mathbf{r}}_{\|} \pm \cos(\theta_{vj})\hat{\mathbf{z}}\right)$, where the $\pm$ sign indicates the propagation direction along the z axis; $\hat{\mathbf{r}}_{\|} = \cos(\varphi)\hat{\mathbf{x}} + \sin(\varphi)\hat{\mathbf{y}}$ and $\hat{\mathbf{z}}$ are unit vectors, θ_{vj} is the polar angle, and φ the azimuthal angle.

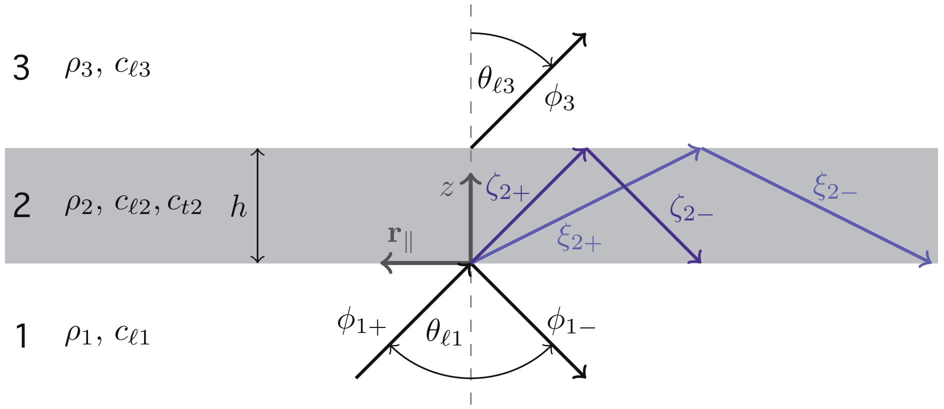

Figure 7.2: Diagram of the plane wave model of a fluid-loaded solid layer. ϕ_{1+} is the incident wave and ϕ_3 the transmitted wave.

For an incident plane wave in region 1, the field in the three regions can be written as follows

$$\phi_1 = \phi_{1+} + \phi_{1-} = e^{i\mathbf{k}^{+}_{\ell 1}\cdot\mathbf{r}} + Re^{i\mathbf{k}^{-}_{\ell 1}\cdot\mathbf{r}}\,, \tag{7.1a}$$

$$\xi_2 = \xi_+ + \xi_- = A^+e^{i\mathbf{k}^{+}_{\ell 2}\cdot\mathbf{r}} + A^-e^{i\mathbf{k}^{-}_{\ell 2}\cdot(\mathbf{r}-\mathbf{h})}\,, \tag{7.1b}$$

$$\zeta_2 = \zeta_+ + \zeta_- = B^+e^{i\mathbf{k}^{+}_{t2}\cdot\mathbf{r}} + B^-e^{i\mathbf{k}^{-}_{t2}\cdot(\mathbf{r}-\mathbf{h})}\,, \tag{7.1c}$$

$$\phi_3 = Te^{i\mathbf{k}^{+}_{\ell 3}\cdot(\mathbf{r}-\mathbf{h})}\,, \tag{7.1d}$$

where $\mathbf{h} = h\hat{\mathbf{z}}$, $A^{\pm}$, $B^{\pm}$ are the complex amplitudes for the upwards $(+)$ and downwards $(-)$ longitudinal and transverse potentials, and R and T are the complex wave-potential amplitudes for the reflected and the transmitted waves respectively. Continuity of the normal displacement and stresses at both interfaces produces a linear system of equations for the six plane wave coefficients, which is solved for each $(\mathbf{k}_{\|}, \omega)$ pair. Losses in the plate can be accounted for using volumetric χ and shear η viscosities included in the Lamé constants as $\lambda \equiv \lambda_0 + \mathrm{i}\omega(2\eta/3 - \chi)$ and $\mu \equiv \mu_0 - \mathrm{i}\omega\eta$ [50]. Leaky Lamb modes appear naturally in this model due to the inclusion of multiple reflections.

7.2.2 The angular spectrum method

A wave potential ψ_1 describing an optoacoustic point source (see Fig. 7.1) in frequency domain can be written as

$$\psi_1(\mathbf{r},\omega) = \frac{e^{\mathrm{i}k_{\ell 1}|\mathbf{r}-\mathbf{r}'|}}{4\pi\,|\mathbf{r}-\mathbf{r}'|}\psi_1(\omega)\,, \tag{7.2}$$

provided that its radius is smaller than all the considered wavelengths; $\psi_1(\omega)$ contains the information characteristic of the acoustic wave generated by thermal expansion under rapid heat deposition [51]. For $z > z_2$, one can express ψ_3 as

$$\psi_3(\mathbf{r},\omega) = \frac{1}{4\pi^2}\int_{-\infty}^{\infty} \psi_3(\mathbf{k}_\parallel, z, \omega)\, e^{\mathrm{i}\mathbf{k}_\parallel\cdot\mathbf{r}_\parallel}\, d^2\mathbf{k}_\parallel \tag{7.3}$$

or, alternatively, via the plane wave expansion of the point source and the solid layer transmission coefficient, as [47]

$$\psi_3(\mathbf{k}_\parallel, z, \omega) = \psi_1(\mathbf{k}_\parallel, z_1, \omega)\, T(\mathbf{k}_\parallel, \omega)\, e^{\mathrm{i}k_{z3}(z-z_2)}\,, \tag{7.4}$$

where $k_{zj} = \sqrt{k_{\ell j}^2 - |\mathbf{k}_\parallel|^2}$. Replacing the explicit expression of the point source [48] evaluated at the 1-2 interface $\psi_1(\mathbf{k}_\parallel, z_1, \omega)$ in Eq. (7.3) and assuming that fluids 1 and 3 have the same properties, i.e. $k_{z1} = k_{z3} = k_z$, yields

$$\psi_3(\mathbf{r},\omega) = \mathrm{i}\frac{\psi_1(\omega)}{8\pi^2}\int_{-\infty}^{\infty} e^{\mathrm{i}\mathbf{k}_\parallel\cdot(\mathbf{r}_\parallel-\mathbf{r}'_\parallel)}\,\frac{e^{\mathrm{i}k_z(z-h-z')}}{k_z}\,T(\mathbf{k}_\parallel,\omega)\,d^2\mathbf{k}_\parallel\,. \tag{7.5}$$

The later expression could be evaluated numerically at points on the detector surface $\mathbf{r} \in S$ using the two-dimensional FFT algorithm. Eq. (7.5) is valid for an arbitrary detector surface and general solid layer transmission including multilayered anisotropic flat layers or even artificial anisotropic plates such as phononic-cristal plates [52]. Taking advantage of the symmetry with respect to the azimuthal angle φ, implicit in the isotropic solid assumption, and setting $\mathbf{r}' = \mathbf{0}$, Eq. (7.5) can be expressed as a Hankel transform [47]

$$\psi_3(\mathbf{r},\omega) = \mathrm{i}\frac{\psi_1(\omega)}{4\pi}\int_0^{\infty} \frac{e^{\mathrm{i}k_z(z-h)}}{k_z}\,T(\mathrm{k}_r,\omega)\,J_0(\mathrm{k}_r\mathrm{r})\mathrm{k}_r d\mathrm{k}_r\,, \tag{7.6}$$

which was evaluated using a Bessel series field expansion implemented in C++. Finally, in order to calculate the insertion loss let

$$\Pi_0(\omega) = \int_S \psi_1(\mathbf{r},\omega)dS\,, \tag{7.7}$$

which is proportional to the pressure detected by the transducer in absence of the solid layer and

$$\Pi_s(\omega) = \int_S \psi_3(\mathbf{r},\omega) dS \,, \tag{7.8}$$

when the solid layer is in the acoustic path, resulting in the following expression for the insertion loss

$$\mathrm{IL} = 20 \log_{10} \left(\frac{\Pi_0(\omega)}{\Pi_s(\omega)} \right) . \tag{7.9}$$

Deviating from the rigorous expression of Eqs. (7.5) and (7.6), one can approximate ψ_3 assuming that waves radiated from the point source follow a straight line that crosses the solid layer modulated only in its amplitude and phase, such that

$$\psi_3(\mathbf{r},\omega) \simeq \psi_1(\omega) \frac{e^{\mathrm{i}k_{\ell 1}(r-h/\cos(\theta_{\ell 1}))}}{4\pi r} T(\mathbf{k}_{\|},\omega) \,, \tag{7.10}$$

where the term $h/\cos(\theta_{\ell 1})$ compensates for the delay excess when the ray crosses the solid layer. Furthermore, assuming that $h/\cos(\theta_{\ell 1}) << r$, the plate and the detector are perfectly aligned, and the point source lies at the focus of a spherically focused detector, the following expression is obtained

$$\frac{\Pi_0(\omega)}{\Pi_s(\omega)} \simeq \frac{\cos(\theta_1) - \cos(\theta_2)}{\int_{\theta_1}^{\theta_2} T(k_{\ell 1}\sin(\theta),\omega)\, \sin(\theta) d\theta} \,, \tag{7.11}$$

where the integral limits θ_1 and θ_2 cover the entire detector surface. Eq. (7.11) corresponds to the plate's transmission loss averaged over a given angle range. It can be readily noticed due to the $\sin(\theta)$ weighting that contributions from angles close to normal incidence are negligible as compared to those collected from the edges of the active aperture.

7.3 Materials and methods

7.3.1 Experimental Setup

Experimental validation of the proposed modelling methodology was done using the multi-mode fibre side-illumination variant of the system as per Chapter 6 (shown in Fig. 6.1). The optoacoustic signal excitation was performed at 532 nm with between 100 - 500 μJ of per-pulse light energy.

Black polyethylene spheres of 20 μm in diameter (Cospheric LLC, Santa Barbara, USA) were used as the optoacoustic point sources. The spheres was kept in a stable position by means of an agarose block. As interstitial objects, a hydrolytic class 1 borosilicate glass cover-slip (Carl Roth, Karlsruhe, Germany) and a piece of the right parietal bone of two 17 weeks old mice (Athymic nude Foxn1$^{\mathrm{nu}}$, Harlan, The Netherlands) were used. The skull pieces were kept hydrated using phosphate-buffered saline solution (Life Technologies Corp., UK) and the same solution was used as immersion medium in the measurements. The optoacoustic signal of the microsphere $s(t)$ was an average acquisition of 10000 shots, and was measured at 9 different positions forming a regular two-dimensional grid with a step size of 3 μm. The interstitial object (the solid plate or the piece of skull) were placed in the acoustic path and the measurement repeated to obtain $s'(t)$. The insertion loss is thus calculated as $\mathrm{IL}(\omega) = 20\log_{10}(S(\omega)/S'(\omega))$. An additional PE-US scan was performed over a region comprising the area of the skull that fell within the transducer's acceptance cone with a step size of 30 μm. The position of the skull relative to the detector was calculated using cross correlation, and the recovered skull surface was then fitted to a plane giving $\hat{\mathbf{n}}$ and z_1 (see Fig. 7.1.

7.3.2 Numerical calculations

A non-exhaustive parameter estimation using a genetic algorithm [53] was performed to retrieve h, ρ_2, $c_{\ell 2}$, c_{t2} and the losses χ, η from the measured IL. The parametric estimation optimization was executed in the frequency range from 10 MHz to 40 MHz in order to match the effective detection bandwidth of the ultrasound transducer. All other parameters were used as input. In particular, it was assumed that $c_{\ell 1} = c_{\ell 3} = 1505$ ms^{-1}, $\rho_1 = \rho_3 = 1000$ kgm^{-3}, and taking the previously described transducer's geometry and the geometrical parameters obtained from the ultrasound scan. Three different calculations were performed using different levels of approximations, namely Eq. (7.6) (Rigorous), Eq. (7.10) (Ray approximation), and a version of Eq. (7.11) (Transmission loss) modified to deal with an arbitrary plate orientation. The transducer's surface was discretised using the Kurihara grid [54] to reduce the computation time of the rigorous model by dividing the surface in different z-levels where the angular spectrum, which is only z dependent, needs to be calculated once. A surface element size of $\Delta r_S = \lambda/5$ was used in the field evaluation. In addition, the integrand of Eq. (7.6) was filtered with a cutoff at 47.4 degrees to avoid aliasing [55].

7.4 Results

7.4.1 Glass plate measurements

The glass cover-slip results, presented in Fig.7.3(a), show good agreement between measured and calculated IL.

The black curve is the mean of the measured IL and it is surrounded by a grey region limited by the minimum and the maximum of the measured IL values. The rigorous model provides the closest fit to the experimental curve, whereas the ray approximation the farthest. The fitted plane gives

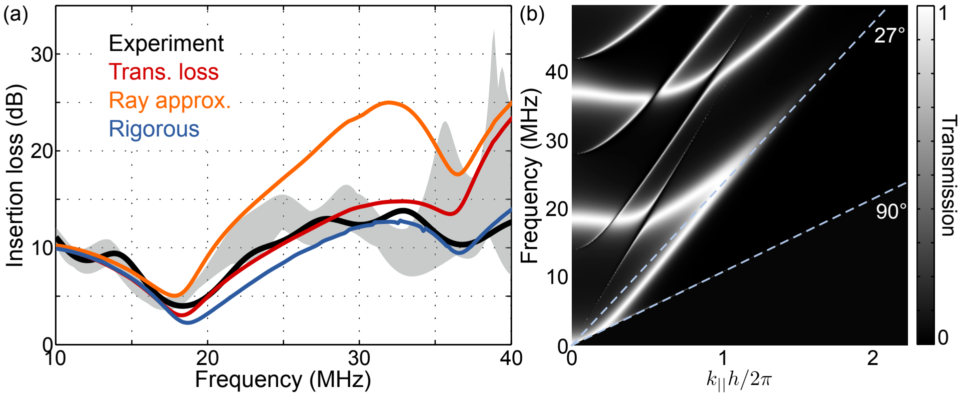

Figure 7.3: Insertion loss as a function of the frequency (a) and transmission $|T(k_{||},\omega)|^2$ dispersion calculated from the estimated parameters (b) for the glass cover-slip. The grey region surrounding the measured mean IL in (a) is limited by the minimum and maximum measured values.

Parameter	Estimation	[49]	Deviation (%)
h (μm)	141	-	-
ρ (kg/m^3)	2203	2200	0.1
$c_{\ell 2}$(m/s)	5242	5560	-6
c_{t2}(m/s)	3796	3430	10

Table 7.1: Estimated parameters for the glass plate compared to [49].

$z_1 = 586$ μm and $\hat{\mathbf{n}} = (0, 0, 1)$. The estimated parameters are compared with the values reported in [49] in table 7.1. The thickness lies within the range given by the manufacturer, i.e. between 130 and 160 μm. All three theoretical curves coincide below 17 MHz but deviate for higher frequencies. The transmission loss is even closer to the measurements than the rigorous model up to 27 MHz but it overestimates the IL at higher frequencies. The extracted parameters yield the transmission dispersion $|T(k_{||}, \omega)|^2$ of Fig. 7.3 (b). Most of the leaky-Lamb modes fall inside the spectral field of view (SFoV) which is limited by the transducer angle of acceptance and which is depicted by the dashed line at 27 degrees. At ~20 MHz the SFoV is intersected by the cutoff-free antisymmetric mode (A$_0$). The presence of this intersection explains the first dip on the IL curve. The second dip at 36 MHz is less pronounced as it results from several modes away from the limit of the SFoV.

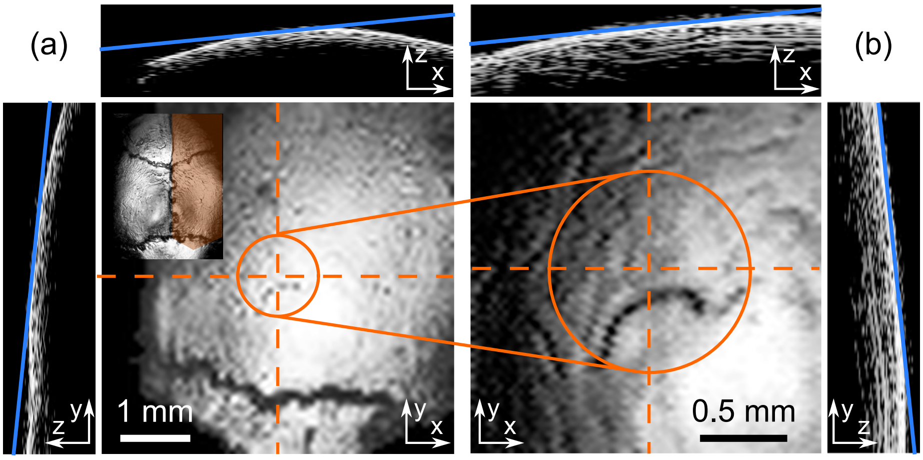

Figure 7.4: Ultrasound images of mouse skull 1 in focus. (a) and (b) show maximum amplitude projections from the top whereas lateral panels depict cross sections taken at the positions of the dashed lines. The portion of the skull which falls inside of the transducer's acceptance cone is indicated by a circle. Blue lines indicate the position of the fitted plane. The inset in (a) shows a full mouse skull and the shadowed area represents the fragment used in the experiments.

7.4.2 Mouse skull measurements

Fig. 7.4 shows pulse-echo ultrasound images of skull 1 imaged for two different scanning ranges. The 1.2 mm diameter circle corresponds to the transducer's acceptance cone projected on the skull surface for an aperture angle of $\simeq$27 deg. The plane fitted to this region can be seen as a blue line in the ultrasound cross sections and gives $z_1 = 1.1$ mm and $\hat{\mathbf{n}} = (-0.0996, 0.0945, 0.9905)$. The IL curves are shown in Fig. 7.5(a). The parameters estimated from the fit are shown in table 7.2. The skull thickness was measured with a caliper to be between 0.41 and 0.50 mm depending on the measured area. Density ρ_2 and longitudinal speed of sound $c_{\ell 2}$ are in agreement with previously reported values for human skull [35, 43].

These values are the average of a multilayered bone structure composed of cortical and cancellous bone, each having different acoustic properties [56]. c_{t2} is higher than the 1500 ms^{-1} reported for human skull [57]), although this work used a simplified interfacial transmission model and only one incidence angle to calculate and measure this value. Compared with mouse skull density from μX-ray CT [58] the estimation presented here lies on the lower range of the reported values ranging from 1800 to 3000 kgm^{-3} from a two dimensional μX-ray CT image, although no average density for the whole skull bone is given, preventing a direct comparison.

A second mouse skull was tested using the same technique with $z_1 =$

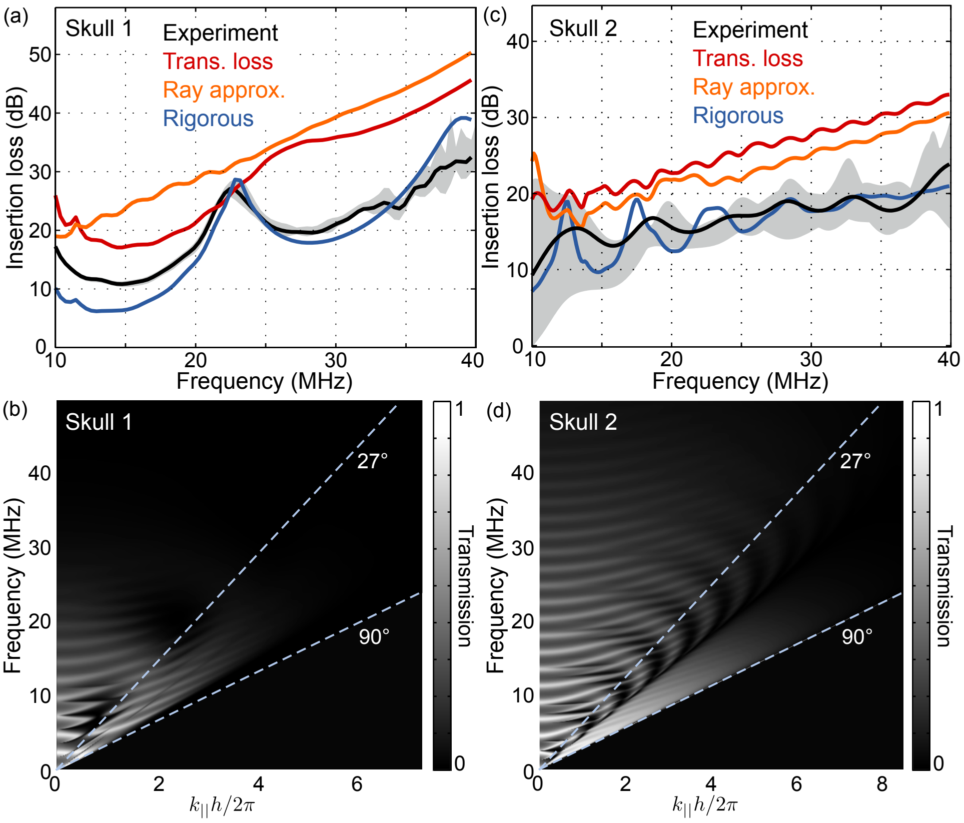

Figure 7.5: Insertion loss as a function of the frequency (a), (c) and transmission $|T(k_{||}, \omega)|^2$ dispersion (b), (d) calculated from the estimated parameters for two mouse skulls. The gray region surrounding the measured mean IL in (a), (c) is limited by the minimum and maximum measured values.

Parameter	Skull 1	Skull 2
h (μm)	458	534
ρ (kg/m^3)	1969	1933
$c_{\ell 2}$(m/s)	2242	2425
c_{t2}(m/s)	1710	1337
χ (Pa s)	0.79	0.013
η (Pa s)	1.99	0.81

Table 7.2: Estimated parameters for two mouse skulls

1.2 mm and $\hat{\mathbf{n}} = (-0.266, 0.102, 0.959)$ extracted from the pulse-echo scan. The IL curves and the fitted curves are shown in Fig. 7.5(c). The parameters estimated from the fit are shown in table 7.2. As a result of the thickness and the more pronounced inclination angle of the skull with respect to the transducer axis, the measured IL curve looks different from the one shown in Fig. 7.5(c). Surprisingly, many more modes are present in the curves due to the increased thickness, although the IL is lower in magnitude, opposite to what would be expected. The most significant deviation is for χ and η, which are one order of magnitude lower for skull 2. Losses mostly affect the prediction of the ray approximation and the transmission loss models, which fail to reproduce the measured IL features. Also for both skulls, the rigorous model is closer to the measured insertion loss. However, at low frequencies, the deviation from the experimental curve reaches up to 7 dB for skull 1 and around 5 dB for skull 2. The greater thickness of the mouse skulls is reflected in the transmission dispersion of its estimated parameters (Fig. 7.5(b) and 7.5(d)). Compared to the glass plate, more modes are inside the SFoV and the effect of the frequency dependent losses is now significant.

7.5 Discussion

Naturally, the accuracy of the frequency-dependent IL estimations using the proposed method will generally depend on the particular transducer used for the measurements. In particular, the angular extent of its aperture for a given focal distance would affect the effective SFoV thus covering different plate modes. This effect is particularly strong at high frequencies as shown in Figs. 7.3(a), 7.5(a), and 7.5(c), where the experimental data exhibit higher variability.

The data obtained from the optoacoustic measurement is generally not sufficient in order to perform accurate parameter estimation. The knowledge of the relative position of the skull with respect to the transducer would allow one to reliably estimate the values of the elastic constants. On the other hand, introduction of additional geometrical parameters, which can play a critical role for transmission of higher frequency components, would further increase the size and the complexity of the optimization problem.

The approach presented here relies on the local flatness of the inspected solid plate. While this condition is easy to fulfill for the simple case of the glass cover-slip, the additional pulse-echo ultrasound scan is key to test this condition on the skulls geometry. In the showcased example (see Fig. 7.4), the validity of the locally-flat-plate condition is evident. In fact, provided the skull is close enough to the transducer focus, most of its surface can be considered as locally flat.

The actual z_1 position is subject to measurement uncertainty when one attempts to fit a plane to an unfocused pulse-echo data. From Eq. (7.6), it can be seen that this uncertainty does not affect the outcome of ψ_3 when both fluids are the same, thus the expression $\exp(\mathrm{i}k_{z1}z_1+\mathrm{i}k_{z3}(z-z_2))$ can be replaced with $\exp(\mathrm{i}k_z(z-h))$. However, the transducer-skull distance does affect the outcome of the measurements as the area of the skull inside the transducer's acceptance cone depends on it. Also, the differences observed between the rigorous model and the approximations point towards the need of including diffraction effects and spatial shifts in the calculations.

In principle, the transmission dispersion can be measured directly using a pair of transducers [41]. However, performing such measurement on small and partially curved non-homogeneous samples over broad frequency range is not straightforward. The presented method overcomes the inconvenience of scanning two focused transducers by introducing a point source and a single-point measurement. The fit of the elastic constants in this case differs from the fit of the dispersion curves in the scanning method. Several sets of elastic constants can produce similar results when only the transmission maxima are used in the reconstruction of the elastic stiffness and the optimisation is performed simultaneously for all parameters. In the presented case, it is the whole measured IL curve that is used in the optimisation procedure.

In order to demonstrate the importance of appropriate modelling of the internal reflections in the skull, Figure 7.6 shows a simplified calculation comparing the transmission dispersion of either fluid (neither c_{t2} nor η are considered) or a solid layer using the estimated parameters of skull 1 (table 7.2). It can be readily seen that neglecting internal reflections implies that the solid layer has the angular spectrum of a fluid-solid interface. Hence, in order to excite a transverse wave, angles far from the normal incidence case must be considered. In such scenario, the effective angular coverage of the spherically focused detector used in the presented experiments might not be sufficient to sense the transverse wave components, thus the optimisation process may conclude with a large set of equally probable c_{t2}. However, the simulation results in Fig. 7.6 clearly show that this assumption would only hold for the low frequency regime ($\omega h/\pi c_{\ell 1} < 1$) and shear effects manifest even at very small angles in the presented model. Whether the

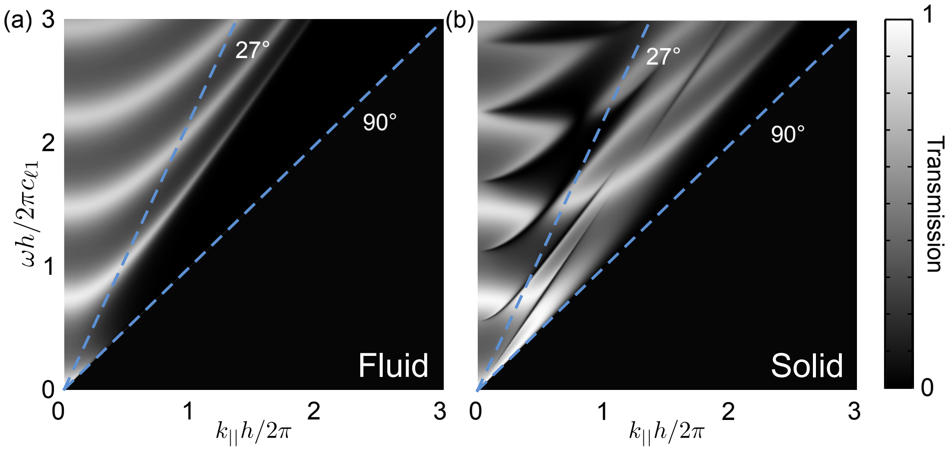

Figure 7.6: Transmission $|T(k_{||},\omega)|^2$ dispersion calculated from the estimated parameters of skull 1 assuming a fluid (a) and a solid (b) homogeneous layer.

same behaviour is to be expected in the skull may only be answered partially and will depend on the fitting accuracy of the presented skull model in each particular case.

Note that the IL is a complex quantity having generally both magnitude and phase. In the present work, only the results for the magnitude of the IL are reported, as the parameter estimation optimisation for the complex IL did not converge to satisfactory results. Existence of inaccuracies in the assumed geometry as well as the general simplicity of the assumed single-layer solid model are amongst the most relevant reasons for this outcome. Future work should consider more sophisticated modelling geometries to compensate for this deficiency.

The computation of Eqs. (7.5) and (7.6) is particularly fast for flat detectors using a quasi-discrete Hankel transform and reconstruction algorithm [59, 60]. However, for the spherically focused detector used in this work, the Hankel transform and reconstruction doubles the computation time of the direct Bessel series expansion when the z-level detector discretisation is used. In addition, the transmission method could be extended to better cope with the structural complexity of the skull, which has been commonly treated as cancellous bone sandwiched between two cortical bone layers [61]. More rigorous approaches could be additionally used to deal with the cancellous bone's porosity [62].

7.6 Conclusion

Here a new method for accurate measurement of the skull's insertion loss over broad frequency range is presented. In addition, a rigorous model has been developed that allows for estimating elastic constants of the skull from the insertion loss data thanks to the coregistered PE-US measurements. The good predictive value of the method has been validated with a glass cover-slip and two ex-vivo adult mouse skulls by using an ultrawideband PVDF spherically-focused ultrasound transducer. The insertion loss attained by the suggested method depends strongly on the detector's geometry and the position of the skull, whereas the estimated parameters are universal and representative of the region within the transducer's acceptance cone. One of the main advantages of the method is the simplicity of the coregistration between the OAM and PE-US scans, which are performed by the same transducer. Thus, no additional imaging technique, such as x-ray computed tomography or magnetic resonance imaging, is required for assessing skull geometry. Both the model and the measurement technique are flexible in terms of skull's orientation and do not require it to be perpendicular to the transducer axis. Also, the flexible semi-analytical formulation allows for seamless extension of the model into more realistic skull models, other transducer geometries, and diverse experimental scenarios involving broadband acoustic transmission through locally flat solid structures. It is thus anticipated that the developed methodology may find broad usability in accurate modelling and quantification of the skull transmission effects, ultimately enabling correction for skull aberrations in a number of applications employing transcranial detection or transmission of high frequency ultrasound.

Part III

Algorithms for synthetic aperture focusing in scanning microscopy

Improving Ultrasound Images from a Hybrid-Focus Optoacoustic and Ultrasonic Microscope

Chapter 8

Background

Optoacoustic microscopy, as presented in this thesis, uses a combination of focused optical excitation, and focused ultrasound detection. Considering, at first, the case of acoustic resolution OAM the necessity for synthetic aperture algorithms can be most clearly stated. The description here is illustrative of the prinicple concepts behind SAFT, with specifics presented in the following chapters

Consider a spherically focused ultrasound detector with three acoustic sources inside the field-of-view, as illustrated in Figure 8.1. The first source, S_0, sits at the acoustic focus, and generates spherical waves. These waves propagate outwards, and when they arrive at the transducer the wavefront arrival is simultaneous across the surface of the detector. Now consider the second source, S_1, which is deep of the focus of the detector; again, this source is generating spherical waves. When the waves arrive at the transducer surface they no longer arrive simultaneously, but are temporally spread. Similarly, the third source, S_2, shallow of the focus, will also arrive at the surface of the detector at different times.

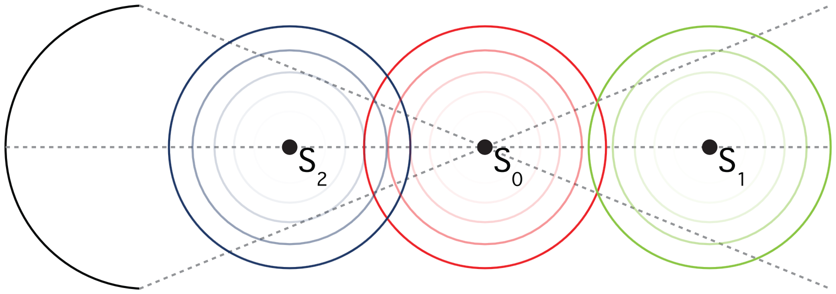

Figure 8.1: How the arrival times for the wavefront of an out-of-focus acoustic source are spread compared to those of an in focus source.

The synthetic aperture focusing technique (SAFT) has been applied broadly in ultrasound imaging [63, 64] and optacousitcs [65, 66]. SAFT is most readily visualised when considering a linear array. In the linear array example consider an acoustic source is positioned in front of one, central element. This source then generates spherical waves, which are incident on each element after some time of flight, and subsequently recorded as a time-domain electrical signal. Assuming the central arrival is known to be correct, then by applying an appropriate delay, $\tau_n = t - \mathrm{d}t$, to the signals for the the adjacent elements the arriving spherical wave appears approximately planar, as illustrated in Figure 8.2. SAFT is a development of this concept, where by appropriately summing these delayed signals the lateral resolution with which the source is resolved can be improved.

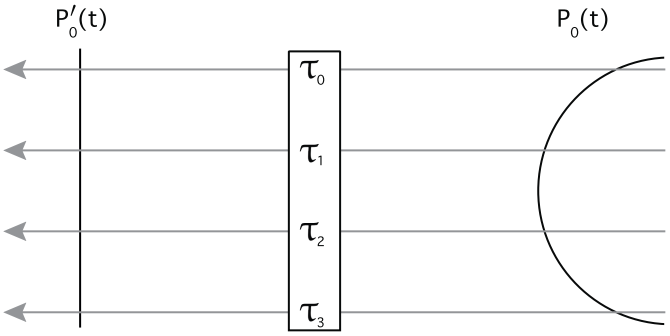

Figure 8.2: An illustration of how delaying the arrivals of a spherical wave $P_0(t)$ to approximate a plane wave $P_0'(t)$

Applying SAFT to focused detection geometry necessitates a different delay calculation than the array example, but the overall principle is the same. By further extension still, the concept translates to AR-OAM by considering that rather than having many elements, the single scanning element provides the adjacent signals. However, there are some overlooked special modifications needed in the application of SAFT which need be considered when applying it to optoacoustics.

Chapter 9

SIR-SAFT

The work presented in this chapter was published in the journal Optics Letters (2014) [67].

9.1 Introduction

There are two main issues in the application of SAFT to OAM data sets. In this chapter the case of AR-OAM is addressed where, due to the tightly focused transducer, sources deep and shallow of the acoustic-focus are poorly laterally resolved. The first aforementioned flaw is that with send-receive modalities, such as pulse-echo ultrasonics, the spatial impulse response of the transducer effects both the strength of the signals generated and the signals detected. Conversely, in AR-OAM the amplitude of signals emitted by sources is not governed by the properties of the ultrasonic transducer, which only influences the detected signals. Secondly, although SAFT is very effective far of the focus, it cannot be applied near-to and at the focus, because the filtering and averaging effects detrimentally effect the in-focus (true) data. An alternative to SAFT is an interpolated model-matrix inversion (IMMI) method as used in tomography. However, the full-3D implementation is currently too slow and only implementable in the simplest case.

Here, a development of SAFT based upon the spatial impulse response (SIR) of the detector is presented, which provides greater improvements for out-of-focus sources in an AR-OAM system. This algorithm, SIR-SAFT, is applicable to AR-OAM data sets both far-of and at the acoustic focus, in full 3D, and due to the delay-sum nature is computationaly fast.

9.2 Theory

A schematic of the SAFT principle can be seen in Figure 9.1, where 5 sources lie at different depths from the focus, F, of the detector, and a line of equal-delay is marked for each source, $-t_1$ to t_3. There are two detector positions shown, (x_0, y_0) and (x_n, y_0), and the sources at t_2 and t_3 will also be detected by detector position (x_n, y_0); position (x_n, y_0) has the spatial impulse response of the detector overlaid. Using Einstein summation notation SAFT is defined as

$$S_{nm}(z) = W_{nmij}(z) \cdot D_{ij}(z - \mathrm{d}z), \tag{9.1}$$

where $D_{ij}(z - \mathrm{d}z)$ is the delayed time-domain signal acquired at transducer position $\mathbf{r}_{ij} = (x_i, y_j)$, and $W_{nmij}(z)$ is a weighting function at $\mathbf{r}'_{nmij} = (x_n - x_i, y_m - y_j)$ that is =1 inside the focal-cone (Fig. 9.1), and =0 elsewhere.

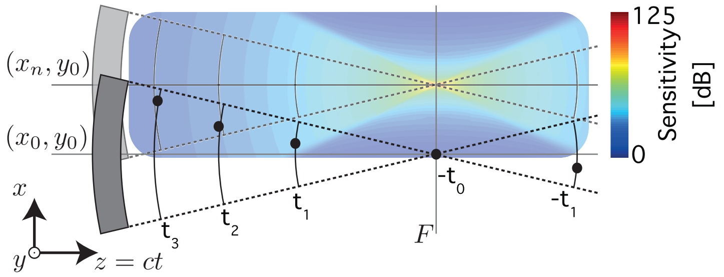

Figure 9.1: A schematic of 5 acoustic sources at different depths from the focus, F, of the ultrasound detector, with lines of equal-delay marked for each source. Two detector positions, (x_0, y_0) and (x_n, y_0), are shown; position (x_n, y_0) has the acoustic sensitivity field of the detector overlaid.

Overall, SAFT improves the lateral resolution and increases the amplitude of out of focus signals, whilst improving SNR. However, the edge of the extent of the contributions considered can cause artifacts in the output image. To address this issue the contributions are often subject to a windowing function during SAFT [64] or a further post-beamforming step, namely the coherence factor (CF), to improve images further still [68]. The CF is defined as

$$CF_{nm}(z) = \frac{|S_{nm}(z)|^2}{N(z)(W_{mnij}(z) \cdot |D_{ij}(z - \mathrm{d}z)|)^2,} \tag{9.2}$$

where $N(z)$ is the depth dependant non-zero width of $W_{nmij}(z)$ and $CF_{nm}(z)$ is effectively a measure of the phase relation of adjacent signals, with highly directional sources giving a high coherent sum. However, the CF is very sensitive to low SNR data [64, 66, 69, 68], which can be common in optoacoustic microscopy.

The method proposed here, SIR-SAFT, uses the SIR of the transducer as the weighting function $W_{nmij}(z)$ in equation 9.1. This approach gives a different set of contributions than the conventionally used angular-acceptance cone, and also weights the amplitudes of the contributed signals non-uniformly.

It is hypothesised that such an approach would both improve lateral resolution and rectify the amplitudes for out-of-focus sources whilst effectively suppressing noise; the algorithm should not interfere with the application of the CF.

9.3 Methods

For the simulation the detector modelled was a cylindrically focused 25 MHz piezo-electric ultrasound transducer with a numerical aperture of 0.45. The receive-mode electrical impulse response (EIR) of the detector was measured experimentally by recording the signal from a 10 μm sphere placed at the focal depth of 12.3 mm. The SIR-SAFT was tested with a simulated data set of 41 microspheres of 30 μm radius uniformly spaced on both sides of the focus. Uniform illumination of very short duration ($\leq$ 10ns) was assumed, with pressure signals for the microspheres being calculated as per [5]. A simulation was made of each sphere individually, and a superposition of all the sources is presented in Figure (9.2a). The EIR measured was then used as the coefficients for a finite impulse response (FIR) filter. Through filtering the simulated data sets from the 30 μm microspheres with said FIR filter the signals were effectively convolved with the EIR of the detector. Additionally, Gaussian white-noise was added to the simulated data with an amplitude of 15% of the maxima. The simulations and subsequent processing were performed in 2D, and SIR-SAFT was also tested on an experimental data set in 3D.

9.4 Results

The abilities of SAFT and SIR-SAFT to improve SNR and to resolve out-of-focus sources can be seen qualitatively in Figure 9.2, which presents (a) a section of the sinogram (raw data) of the simulated data set, (b-c) the results of conventional SAFT and SIR-SAFT processing, and (d-e) the results of applying the CF to both SAFT and SIR-SAFT. Also presented in Figure 9.2 are the superposition of the acoustic signals at $x = 0$ for (top-bottom) the sinogram, and the results of the SAFT and SIR-SAFT processing, respectively.

To better evaluate the performance of the different methods the SNR and the lateral and axial full-width half maximum (FWHM) were calculated for each source in the simulated data set. The lateral FWHM values are presented in Figure (9.3a), though the corresponding axial values may be found in Table 9.1. The axial SNR values are also presented in Figure (9.3b).

The values of FWHM and SNR for three of the sources in the simulated data and the subsequent SAFT-based processing results are presented in Table 9.1. The sources selected were located 3 mm shallow of the focus

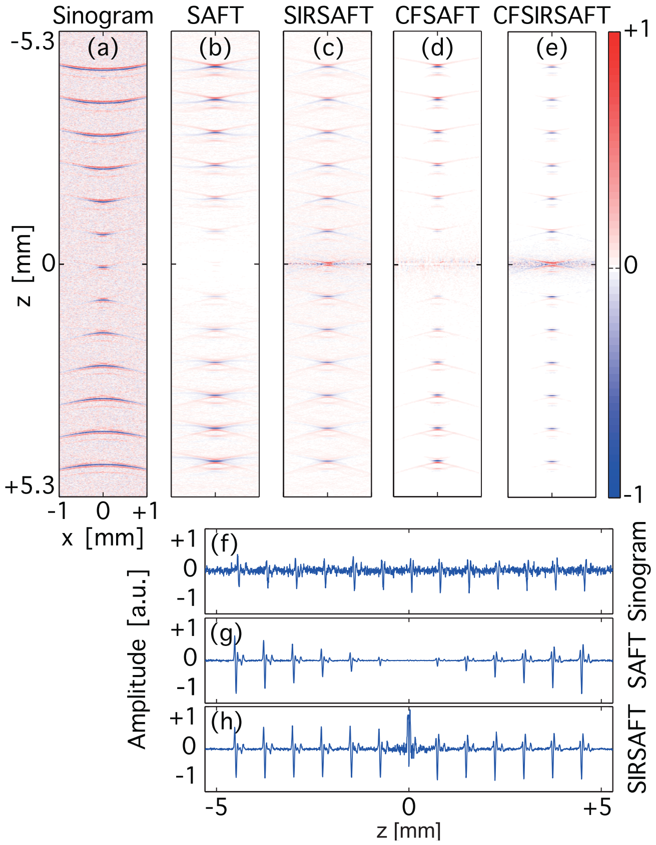

Figure 9.2: A superposition image of the sinograms for simulations of 30 μm spheres at different depths, where 13 of 41 spheres are shown (a); and, (b-e) a superposition of the results of applying SAFT, SIRSAFT, CFSAFT, and CFSIRSAFT. The superposition of the acoustic signals at $x = 0$ is shown below as (f-h) sinogram, SAFT, and SIRSAFT.

(-3 mm), at the focus (0 mm), and 3 mm deeper than the focus (+3 mm). Asterisks in Table 9.1 denote affected values where the application of SAFT is destructive rather than beneficial, which occurs near the focus where the data approaches being true. Because of this SAFT is only applicable outside of a near-focus boundry area, the data from inside which needs to then be copy-pasted into the final image alongside the results of SAFT. However, such a boundary will be visible in the final image, and must be defined on a per scan basis.

The testing on the simulated data shows that SIR-SAFT can effectively rectify the signals at all depths (Fig. 9.2h) rather than introduce a large amplification to out-of-focus signals at the expense of those near the focus (Fig. 9.2g). Further, SIR-SAFT can be seen to outperform conventional SAFT in terms of improved lateral resolution (Fig. 9.3a), where the improve-

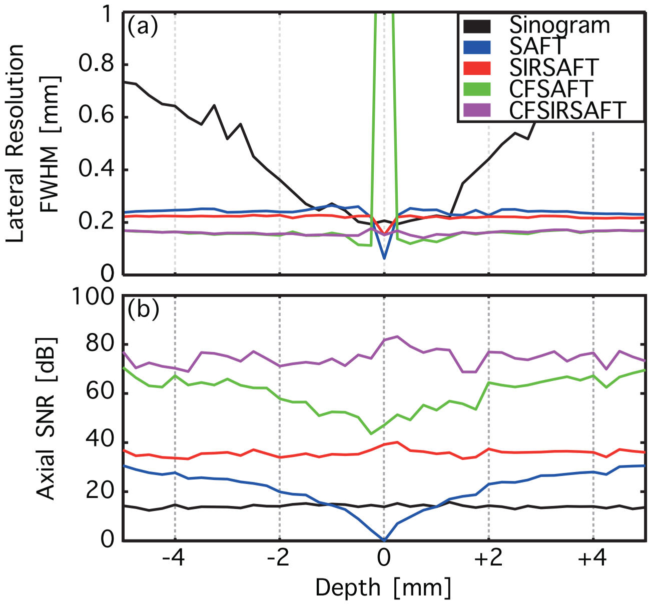

Figure 9.3: The lateral FWHM (top) and the axial SNR (bottom) for all 41 simulated microspheres at many depths, as per Figure 9.2.

ment compared to SAFT is small for out-of-focus sources, but significant for near-focus sources (Tab. 9.1). The performance of SIR-SAFT in improving SNR is also significant, with the rectified signals being of around 36-39 dB for all depths (Tab. 9.1, Fig. 9.3b), whereas conventional SAFT performed closely to SIR-SAFT out-of-focus but very poorly near-focus (Fig. 9.3). Lastly, SIR-SAFT did not impede use of the CF, but rather the improvements were compounded. This is clearly seen as the results of CF-SIR-SAFT gave an SNR of $\geq$70 dB throughout the focal field, compared to $\simeq$15 dB for the raw data (Fig. 9.3b).

The experimental data set is of a 30 μm suture loosely knotted and placed in scattering agar (1% intralipid) at an oblique angle to the focal plane. The data set was acquired with a DAC of 250 MHz sampling frequency (Model: M3i.4142; Spectrum Systementwicklung Microelectronic GmbH, Grosshansdorf, Germany) with uniform illumination at 532 nm, which was supplied by a pumped Nd:YAG Q-switched laser (Model: IS8II-E; Edge-Wave GmbH, Wöurselen, Germany). The spherically focused piezoelectric ultrasound transducer used had a center frequency of 25 MHz, an outer diameter of 5.5 mm, and a focal length of 12.3 mm (InSensor, Kvistgaard, Denmark); the same detector as was used in the simulations. The volumetric data set was acquired using a raster scanning translation of the detector in $x - y$, with a step size of 20 μm in both dimensions, a pulse repetition frequency of 1 KHz, and with 50 averages per-position. Post acquisition the

Method	Source Depth					
	-3 mm		**0 mm**		+3 mm	
	FWHM (lat./ax.) [μm]	SNR [dB]	FWHM (lat./ax.) [μm]	SNR [dB]	FWHM (lat./ax.) [μm]	SNR [dB]
Sinogram	638/27	13.4	207/24	13.8	518/27	13.7
SAFT	243/27	26.5	63/585*	0*	239/26	25.1
SIR-SAFT	225/27	36.1	152/7	39.2	224/26	36
CF-SAFT	167/24	64.7	2712*/7	47.1	158/24	65.9
CF-SIR-SAFT	169/25	75.3	152/7	81.8	160/25	75.2

Table 9.1: Qualitative measures of resolution and SNR performance for SAFT, SIR-SAFT, CF-SAFT, and CF-SIR-SAFT. The values are for sources 3 mm shallow of the focus, the focus (bold), and 3 mm deeper than the focus. Asterisks denote affected values.

data were bandpass filtered between 3-30 MHz, and down-sampled to 62.5 MHz sampling frequency and 40 μm step size so as to reduce the computational time for processing. The sinogram for the experimental data and for the results of CF-SAFT and CF-SIR-SAFT processing were also rendered as volumes (Amira, Visage Imaging Inc.), which are presented in Figure 9.4. In these images the data were normalized and the same colourmap and thresholds were applied to each data set.

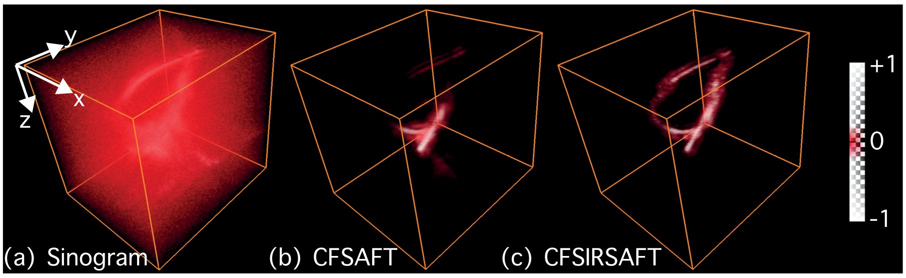

Figure 9.4: A volume rendering of experimental optoacoustic microscopy data of a loosely-knotted 30 μm suture, where (a) is the sinogram, and (b) is the results of CF-SAFT processing, and (c) is the results of CF-SIR-SAFT processing.

Top-down maximum amplitude projections (MAP) for a scan of a 30 μm suture are presented in Figure 9.5. A photograph of the suture from above (without the scattering layer) (a) shows the approximate region of interest (ROI) for the MAP images as a white box. The MAP image of the sinogram (b) shows the FWHM of the suture along two white lines, which correspond to a near-focal depth (lower-left value) and a far-focal depth (upper right value). These measures are also present for the MAP images for (c) the SAFT result, (d) the SIR-SAFT result, and (e-f) subsequent application of the CF to both SAFT and SIR-SAFT, respectively.

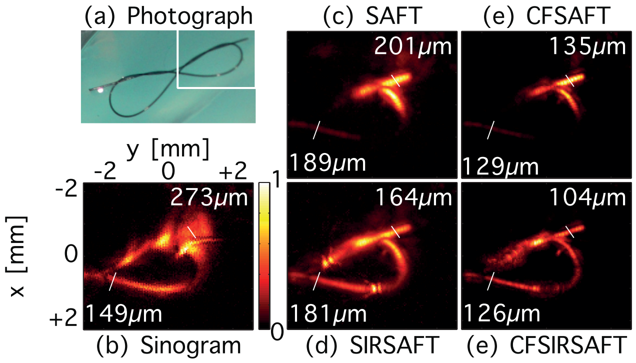
(a) Photograph
(c) SAFT
(e) CFSAFT
201μm
135μm
189μm
129μm
y [mm]
-2
0
+2
1
-2
x [mm]
0
+2
273μm
149μm
164μm
181μm
104μm
126μm
0
(b) Sinogram
(d) SIRSAFT
(e) CFSIRSAFT

Figure 9.5: Maximum amplitude images with annotated measures of FWHM for a 30 μm suture orientated obliquely to the focal plane after different SAFT-based processing; a photograph of the suture phantom is annotated with the approximate ROI.

9.5 Discussion & Conclusion

The testing of SIR-SAFT on the experimental data showed significantly better performance than SAFT, again the performance was compounded by the application of the CF. This can be seen as the improvement of measurable FWHM of the suture both near and far of the focus (Fig. 9.5), and as the more uniformly amplitude corrected suture structure throughout the rendered volume (Fig. 9.4). Overall these improvements see SIR-SAFT as a promising algorithm for application in AR-OAM, given its ability to recover resolution and increase SNR without distorting the data, a highly desirable trait in OAM, especially with regards to multi-spectral imaging and functional studies.

Chapter 10

Universal Synthetic Aperture Framework for Scanning Optoacoustic Microscopy with Heterogeneous or Non-Stationary Illumination (W-SAFT)

The work presented in this chapter was published in the journal Optica (2017) [70].

OAM is a highly versatile imaging method that can achieve high spatial resolution at superficial depths through use of focused illumination (OR); and, can be adapted for imaging with ultrasonic resolution at much greater depths where the excitation light is diffuse (AR). These two modes of operation can be further combined to create a highly scalable technique that can image at multiple penetration scales by gradually exchanging microscopic optical resolution in superficial tissues with ultrasonic resolution at diffuse (macroscopic) depths. However, optoacoustic microscopy commonly employs scanning acquisition geometries that impede the use of synthetic aperture techniques to achieve meaningful images due to non-stationary illumination patterns and strong non-uniformity of the excitation light field. Here a universal framework for scanning optoacoustic microscopy is presented that uses a weighted synthetic aperture focusing technique (W-SAFT) to create a uniform imaging sensitivity across microscopic, mesoscopic and macroscopic penetration regimes. Robust performance of the new multi-scale reconstruction methodology is showcased with simulations, synthetic phantoms, and validated with experimental data acquired from juvenile zebrafish. It is shown that the consideration of the fluence is vital, as any optically dictated lateral-resolution is maintained, while lateral resolution for out-of-focus ultrasonic data is improved; additionally, the dynamic range of the peak-peak signal amplitudes is compressed to improve data visualisation.

10.1 Introduction

As shown in previous chapters, scanning optoacoustic microscopy comes in two main variants. In AR-OAM [15], a focused ultrasound transducer is used and illumination is usually broad with respect to the field of view (FOV) of the transducer (Fig. 10.1(a)), whereas in OR-OAM [71, 16, 13] an unfocused ultrasound transducer is used and the lateral-resolution is dictated by the beam width of the focused illumination at a given depth (Fig. 10.1(b)). As seen in previous chapters, the AR approach is successful at imaging many centimetres deep in optically scattering media, however the limit of achievable resolution is dictated by the properties of the transducer e.g. numerical aperture, bandwidth, sensitivity. Furthermore, the lateral resolution outside the focal area is restorable through methods such as the virtual detector method [66], synthetic aperture focusing technique (SAFT) [67], and model matrix inversion [72, 73]. However, consideration of the light fluence distribution in the imaged tissue is vital as it may directly affect the resulting image quality, in particular when synthetic aperture focusing is applied to non-stationary (moving) illumination datasets. On the other hand, when considering an optically non-scattering medium with an illumination beam of low divergence, the achievable lateral resolution of the OR method can theoretically be very high, approaching the optical diffraction limit. However, biomedical imaging targets are typically optically scattering, thus after a few hundred micrometers the beam becomes diffuse, which limits the effective penetration of the modality to superficial depths [17]. Overall, OR microscopy is capable of achieving greater resolution than AR microscopy, though the latter is the only valid approach for deep-tissue imaging.

More recently, hybrid focus optoacoustic microscopy (HFOAM) systems, which employ a combination of focused illumination and focused ultrasound detection are being developed [14, 74]. Indeed, the system presented in Part I is one such system. These systems aim to provide OR in the superficial regime gradually exchanged for AR at depths where the light is diffuse. Here it is similarly necessary that any algorithms employed to restore out-of-focus lateral resolution in the AR regime do not impair the lateral-resolution in the OR regime. Additionally, although computationally fast, SAFT or other existing delay-sum based image reconstruction algorithms do not address the issue of fluence, as they are based on the assumption of an AR scenario and thus homogeneous illumination.

Introduced here is a weighted synthetic aperture focusing technique (W-SAFT) to account for arbitrary scanning fluence in optoacoustic microscopy systems. This algorithm was developed through a distortion-correction approach, and considers the transducer sensitivity, optical beam properties, and optical properties of the imaging target, to give optimal lateral resolution throughout the scanned volume. Additionally, amplitudes are compressed to within a more useful dynamic range without loss of context, i.e. preserving the relative strength of the different optical absorbers in the corrected images.

10.2 Theory

10.2.1 Background

Most scanning optoacoustic microscopy systems translate the ultrasound transducer and illumination source to acquire time-domain optoacoustic signals of N samples from a set of points in the x–y plane (x_i, y_j). Typically, two linearly-spaced arrays of $\{x_1, ..., x_n\}$ and $\{y_1, ..., y_m\}$ define a regular grid of measurement locations. The scan volumes of such systems are therefore a volume $\boldsymbol{D}$ with size (n, m, N), and are spatially defined as (x, y, z), where $z = c_0 N/f_s$, c_0 is the speed of sound and f_s is the temporal sampling frequency. The instantaneous centre of the volume is given as $(x', y', z') = (x - x_i, y - y_j, z - z_f)$, where $i = 1, ..., n$, $j = 1, ..., m$, and z_f is the focal length of the transducer. This distinction is necessary as although the (x, y, z) space is intuitive in viewing the data volumes, the W-SAFT algorithm works in the (x', y', z') space.

The optoacoustic signals are only detected from locations where optical absorbers are both located within the FOV of the ultrasound transducer and illuminated by the short duration laser light. As can be seen in Fig. 10.1(a), for AR microscopy the entire transducer's FOV falls within the limits of the diffuse light fluence, thus any optical absorber within the FOV will yield a measured signal. Conversely, in the OR regime (Fig. 10.1(b)) the same FOV is only partially illuminated, thus not all the optical absorbers within the transducer's FOV inherently generate an acoustic wave to detect. At shallow depths, before the incident illumination is divergent, HFOAM essentially produces OR-type data, whereas at greater depth the illumination is equal to or broader than the extent of the FOV of the transducer, producing AR data (Fig. 10.1(c)).

SAFT uses a delay and sum based operation to steer an artificial acoustic focus through volumetric data. The method has successfully been used to correct for the focusing distortions of spherically focused transducers i.e. to restore out-of-focus lateral resolution by exploiting overlapping acquisitions. The SAFT operation in spherical coordinates, illustrated in Fig. 1(d), can be written as

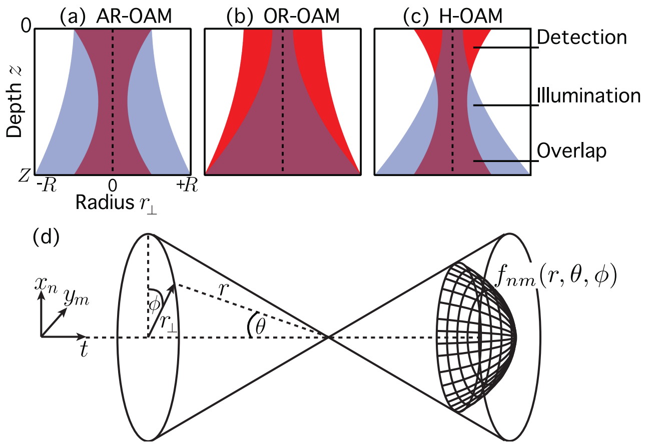

Figure 10.1: Illustrations of the extents of the axially symmetric fields of light fluence (blue) and ultrasound-transducer field-of-view (red) as functions of depth z and polar-radius (radius to the focal axis) $r_\perp$. (a) The acoustic resolution (AR) case with broad illumination and focused detection, (b) The optical resolution (OR) case with a focused illumination, (c) Hybrid resolution optoacoustic microscopy (HFOAM) uses both focused illumination and detection. An illustration of the 3D-SAFT operation in spherical coordinates is shown in (d).

$$\sigma_{nm}\{f_{nm}(r,\theta,\phi)\}(t) = \int_0^{2\pi}\int_{\theta_1}^{\theta_2} f_{nm}(r,\theta,\phi)\mathrm{d}\theta\mathrm{d}\phi, \tag{10.1}$$

where nm denotes the discrete transducer position in x–y , $f_{nm}(r,\theta,\phi)$ is a function through the acquired data at a radial distance r from the transducer-focus, and has axial spherical symmetry through ϕ, and an arc length between θ_1 and θ_2 as limited by the FOV of the transducer. Additionally, $r_\perp$ is the polar radius of r, and r can be described in the scanning coordinate system (x,y,t) as $r^2 = x^2 + y^2 + (c_0 t)^2$.

Overall, the integration through f_{nm} is therefore a summation through equal delay, and performing this operation for all unique values of r at each transducer position for a data set restores the out-of-focus lateral acoustic resolution. This operation is readily applied to AR data, however, for OR microscopy, or the OR-to-AR transitional (mesoscopic) regime in HFOAM, SAFT will laterally blur data in all x-y planes where the fluence is narrower than the lateral FOV of the transducer. One further artefact in the results of SAFT processed data is an amplitude bias for out-of-focus sources. The summation based operation has many more contributions out-of-focus than near-focus.

10.2.2 The W-SAFT Algorithm

The limits of integration in the SAFT operation (10.1) can be alternatively considered a function of their polar radius, $r_\perp$, and time, t for the ϕ-symmetric combined sensitivity field. Thus, (10.1) can be rewritten as

$$\sigma_{nm}\{f_{nm}\}(t) = \iint^{\gamma(r_\perp,t)} f_{nm}(r,\theta,\phi)\mathrm{d}\theta\mathrm{d}\phi, \tag{10.2}$$

where the limits function $\gamma(r_\perp, t)$ can readily be replaced by a binary volume $\mathbf{\Gamma}$ which is 1 inside the limits, and 0 elsewhere, and has the same dimensions as $\boldsymbol{D}$.

This limits function, $\gamma(r_\perp, t)$ in the AR case is defined by the limits of the FOV of the transducer, $\psi(r_\perp, t)$, which is readily calculable from the geometry. However, in HFOAM data the lateral resolution is optically dictated over a certain depth range, thus the limits function is the combination of the transducer's FOV and the extent of the light fluence. Normalisation of the fluence was performed along the spherical arcs of equal delay to the acoustic focus.

By doing so for each unique arc, $\Upsilon(r)$, where Υ is the unique-value operator, the focus-normalised fluence function $\hat{u}$ and the subsequent fluence extent function $\hat{u}'$, can be written in spherical coordinates as

$$\begin{aligned} \hat{u}(r,\theta,\phi) &= \frac{u(r,\theta,\phi)}{\max(|u(r,\theta,\phi)|)} \qquad \forall\,\Upsilon(r), \\ \hat{u}'(r,\theta,\phi) &= \begin{cases} 1, & \text{if } \hat{u}(r,\theta,\phi) > k \\ 0, & \text{otherwise,} \end{cases} \end{aligned} \tag{10.3}$$

where u is the fluence field and k is a threshold value. Furthermore, the combined extent function is given as

$$\gamma(r,\theta,\phi) = \psi(r,\theta,\phi)\,\hat{u}'(r,\theta,\phi), \tag{10.4}$$

and $\mathbf{\Gamma}$ can again define a binary masking volume. It should be noted, that the value for k is most appropriately set as the value of $\hat{u}'$ at the intersection of ψ and $\hat{u}'$ for the greatest value of r below the focus for which an optoacoustic source can still reasonably be expected to be excited. Obviously, in simulations this depth is known, though must be estimated or observed for experimental data.

The routine of applying the SAFT integral at each transducer position can be written as

$$\mathbf{V} = \mathtt{SAFT}(\mathbf{D}(\mathbf{r}), \mathbf{\Gamma}(\boldsymbol{r'})), \tag{10.5}$$

where r' is r centred at (x_n, y_m, z').

The general approach of W-SAFT is that $\boldsymbol{\Gamma}$ is used to spatially mask the summation of the data, $\boldsymbol{D}$. Thereby data in the OR and mesoscopic regimes are not blurred, yet the lateral resolution of data in the AR regime can be improved. As $\boldsymbol{\Gamma}$ is a combination of the fluence field and the FOV of the transducer, then in an imaging target with a non-flat optically scattering surface it must be recalculated for each of the n unique surface depths as $\boldsymbol{\Gamma}_i$, where $i = 1 : n$. A subset of the data volume $\boldsymbol{D}_i$ can then be defined as any voxel of $\boldsymbol{D}$ where the above surface matches the current depth, i.e. where $S(x, y) = S_i$. For each matched surface point, the limiting function further defines a region (typically conical in shape) below said point where the excitation-detection criteria are met. By iterating over each surface depth and processing the $\boldsymbol{D}_i$ volumes with SAFT masked by the associated $\boldsymbol{\Gamma}_i$, a cumulative output volume $\boldsymbol{V}$ can be constructed as the sum of each sub-volume SAFT result, $\boldsymbol{V}_i$ i.e.

$$\boldsymbol{V} = \sum_{i}^{n} \left[\boldsymbol{V}_i = \texttt{SAFT}(\boldsymbol{D}_i, \boldsymbol{\Gamma}_i)\right]. \tag{10.6}$$

There are two major distortions that arise in $\boldsymbol{V}$ as a result of this process. Firstly, the refocusing-distortion from SAFT itself, which gives rise to higher amplitude signals further from the acoustic focus. Secondly, a cumulative error from repetitious additions of the same voxel i.e. where $\boldsymbol{D}_i$ has overlap between different depth iterations. There also exists a third trend in the final data, which is due to the attenuation and spreading losses in the fluence through the volume.

The first distortion can be compensated for by measuring the refocusing distortion for each depth iteration

$$\boldsymbol{F}_i = 1/\texttt{SAFT}(\boldsymbol{O}, \boldsymbol{W}_i), \tag{10.7}$$

where $\boldsymbol{O} = 1 \; \forall (x, y, z)$, and $\boldsymbol{W}_i$ is a weighting-masking function, which itself is a combination of several functions

$$\boldsymbol{W}_i = \boldsymbol{H}\, \boldsymbol{U_i}\, \boldsymbol{\Gamma_i}, \tag{10.8}$$

where $\boldsymbol{H}$ is the maximum amplitude projection (MAP) in time of the 4D spatial impulse response (SIR) and $\boldsymbol{U}_i$ is the 3D fluence distribution for the current surface depth S_i. At this stage, $\boldsymbol{U}_i$ does not contain an optical attenuation term, with amplitude variations solely from lateral widening of the beam. The second distortion, the cumulative addition of common-voxels as a result of iterating over surface depths, is compensated for through the use of a count-matrix, $\boldsymbol{C}$, which is calculated via

$$\boldsymbol{C} = \sum_{i}^{n} \boldsymbol{\Gamma}_i. \tag{10.9}$$

The data subset $\boldsymbol{D}_i$ is then divided by the count-matrix correction before being passed to the SAFT operator, so as each output voxel has had any cumulative amplitude bias removed. Including the two distortion correction steps, the SAFT procedure can be written as per (10.10), which is also illustrated in Fig. 10.2.

$$\begin{aligned}
&\text{for } i = 1 : n\{\\
&\qquad \boldsymbol{D}_i' = \boldsymbol{D}_i / \boldsymbol{C}\\
&\qquad \boldsymbol{W}_i = \boldsymbol{H}\, \boldsymbol{U}_{\boldsymbol{i}} \boldsymbol{\Gamma}_{\boldsymbol{i}},\\
&\qquad \boldsymbol{V}_i' = \texttt{SAFT}(\boldsymbol{D}_i', \boldsymbol{\Gamma}_i),\\
&\qquad \boldsymbol{F}_i = 1/\texttt{SAFT}(\boldsymbol{O}, \boldsymbol{W}_i),\\
&\qquad \boldsymbol{V}_i = \boldsymbol{V}_i' \, \boldsymbol{F}_i\\
&\qquad \}\\
&\boldsymbol{V} = \sum_i^n \boldsymbol{V}_i.
\end{aligned} \tag{10.10}$$

The output volume $\boldsymbol{V}$ here will be corrected for the refocusing distortions, and the cumulative amplitude bias. However, as previously stated, the fluence term $\boldsymbol{U}$ only contains amplitude variations that result from beam widening, thus any estimations of light attenuation must be included additionally. The main assumption here is that the incident fluence is unattenuated until reaching the surface $S(x, y)$ and thereafter the generalised attenuation coefficient, α, is a constant forming a depth-dependent attenuation function, $A(z)$, of a general form

$$A(z) = e^{\alpha z},\ \alpha \leq 0. \tag{10.11}$$

As the fluence distribution in HFOAM is scanning in the lateral plane, it is imperative that correction for $A(z)$ be included in the SAFT operation, and not as a pre- or post-correction step. This correction is done by defining a fluence-attenuation compensation function $G(z) = 1/A(z)$, and modifying the definition of $\boldsymbol{V}_i'$ in (10.10) to be

$$\boldsymbol{V}_i' = \texttt{SAFT}(\boldsymbol{D}_i', \boldsymbol{\Gamma}_i \boldsymbol{G}), \tag{10.12}$$

where $\boldsymbol{G}$ varies in z only.

Our approach does not dictate the most appropriate method for fluence estimation, which is a complex research topic unto itself. For the current investigation, models of embedded Gaussian beams [75] were used, where the un-scattered incident beam, $v(x', y', z)$ was defined by beam waist values chosen from the geometrical properties of the illumination optics as per [76]. With this model the beam waist at the optically scattering surface $S(x, y)$ could then be determined. Taking the at-surface beam waist of the un-scattered beam, an at-depth scattered beam waist was selected. With

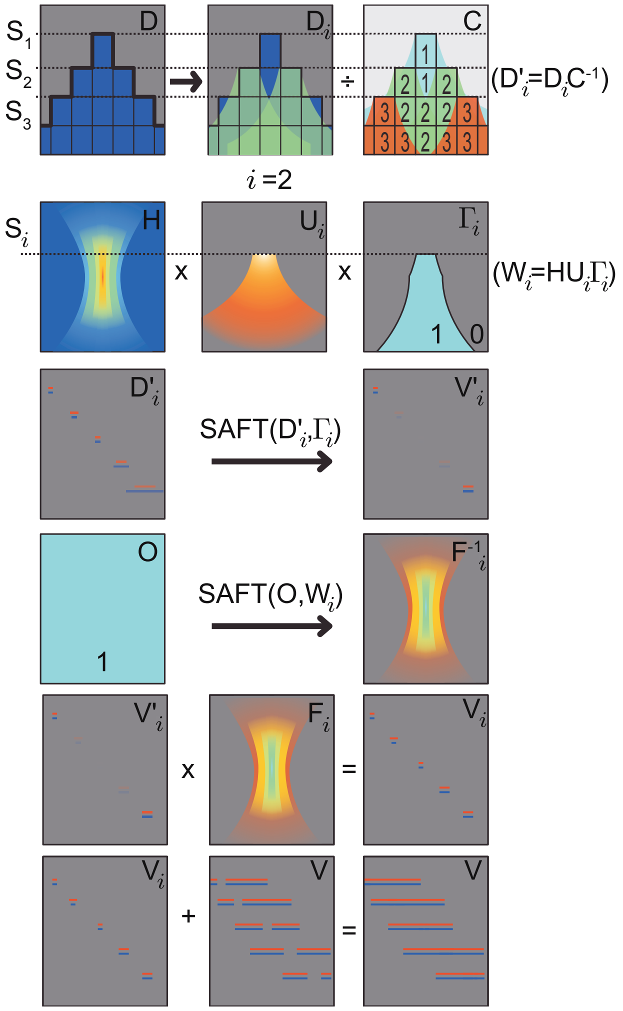

Figure 10.2: A schematic illustration of the process of implementing W-SAFT. Each row of the figure corresponds to one line in (10.10).

these two beam waists, the M^2 value for the scattered beam was calculated, as was the beam waist at all depths inside the scattering volume, giving the scattered beam $\boldsymbol{U}_i = u_i(x', y', z)$. To model the scattered beam for experimental data, an estimate of the beam spread at a certain depth inside the imaging target needed to be determined. This was achieved by iteratively running many instances of W-SAFT while varying the at-depth beam-waist until an output volume met the criterion of not blurring the at-depth lateral resolution and, ideally, yielding an improvement.

Although in simulation any attenuation modelled is known and can thus be used to modulate $\boldsymbol{U}_i$, in the experimental case this must be estimated. For the experimental data presented in the following sections, the fluence attenuation was estimated based on fitting curves to the instances of $\boldsymbol{V}_i$ as returned by (10.10) without $\boldsymbol{G}$. This was deemed appropriate as fluence attenuation is the major cause of decreasing signal amplitude in z. Because of the surface-depth dependent nature of $\boldsymbol{V}_i$, the gain function is also estimated on a per-surface-depth basis; this estimate is then combined into a revision of (10.12) as

$$\begin{aligned} \mathcal{G}_i &\approxeq \boldsymbol{G}_i, \\ \boldsymbol{V}_i' &= \texttt{SAFT}(\boldsymbol{D}_i', \boldsymbol{\Gamma}_i \mathcal{G}_i). \end{aligned} \tag{10.13}$$

One major limitation in the peak-to-peak amplitude equalisation of signals from sources in the optically-dictated resolution regime is, intuitively, that as not all possible lateral contributions exist, the superposition necessary for full peak-peak equalisation cannot be achieved. Therefore, the peak-to-peak amplitude equalisation is best considered as a dynamic range compression. Additionally, this limited-contribution scenario will limit the potential for improving spatial-resolution.

10.3 Methods

In the development and assessment of the new algorithm, four data sets were used. The first was a simulated data set, as described previously, the second and the third were an experimental scan of a suture phantom in both clear and scattering agar, and the fourth was an ex-vivo scan of a juvenile zebra fish.

In the post-processing of the simulated and experimental scans, a PC with 64GB RAM, a 3.2 GHz processor (i7 3930, Intel, USA) and a GPU with 2304 cores and 3GB onboard memory (GeForce GTX 780, Nvidia, USA) was used.

10.3.1 Simulated Scan

For initial performance testing, a scan was simulated for 9 microspheres of 60 μm diameter arranged at equal vertical intervals between ± 1.4 mm from the acoustic focus, spaced uniformly in a 3x3 grid through x–y between ± 1 mm from the centre of the imaged volume. The scattering optical surface was modelled as a dome of concentric rings having uniform depth and equal step size centred above the centre of the imaged volume. The modelled Gaussian-beam fluence was also subject to an additional attenuation-modelling gain of -12 dB/cm below the scattering surface.

The optoacoustic signal for the microspheres was calculated as per [5], and to model the detection of the pressure signals by the transducer, the program Field-II was used [18]. The transducer was simulated as broadband, and subsequently the final data set could be filtered to simulate the effects of any electrical impulse response (EIR); Field-II was also used to simulate the

SIR of the transducer. To reduce runtime in computing the simulated scan, the axial symmetry of the microspheres, transducer, and incident fluence was exploited. Namely, the pressure signals detected for each sphere $p(t)$ were modelled not for all pairs of (x, y) but rather for all unique values of the radii r, i.e. $\Upsilon(r) = \sqrt{x_n^2 + y_m^2}$. Subsequently, the simulated data was extruded about the instantaneous z-axis (the sphere centre) at (x', y', z). This sub-volume $\boldsymbol{D'}$ could then be weighted by the subset of the moving-fluence incident over the sphere, which is dependent on the corresponding subset of the surface $\boldsymbol{S'}$, and summed into the master volume $\boldsymbol{D}$.

This simulated data was also processed with a modified version of a previous implementation of a weighting-based SAFT algorithm, SIR-SAFT [67], which exclusively uses the SIR of the transducer as a weighting field. However, as this algorithm assumes spatially uniform fluence, it was modified as follows to include fluence-dictated spatial masking.

$$\begin{aligned} &\text{for } i = 1 : n\{ \\ &\qquad \boldsymbol{W}_i = \boldsymbol{H}\,\boldsymbol{\Gamma_i}, \\ &\qquad \boldsymbol{V}_i = \texttt{SAFT}(\boldsymbol{D}'_i, \boldsymbol{W}_i), \\ &\qquad \} \\ &\boldsymbol{V} = \sum_i^n \boldsymbol{V}_i. \end{aligned} \tag{10.14}$$

10.3.2 Phantom Scan

Two phantoms were made with sutures of 50 μm cross-sectional diameter mounted in a cylinder of agar. In phantom A the agar was non-scattering and contained 6 sutures, whereas phantom B was highly scattering (1% intralipid concentration) and contained 5 sutures. The purpose of these phantoms was to demonstrate the application of the proposed algorithm to experimental data in both the OR and AR regime.

The scans were performed with the HFOAM system presented in Part I, using the PVDF ultrasound transducer for detection, except operating in the raster-scan mode so as signal averaging could be used to ensure high SNR; illumination was delivered through the multimode fibre. The scan performed on phantom A covered an x–y region of 3x3 mm in square steps of 30 μm with a pulse repetition frequency of 1 KHz and a per-pulse energy of around 275 μJ; the scans were made with 50 averages per position. The scan of phantom B was over a larger region of 9x9 mm with steps of 60 μm and 350 averages per position.

In the simulated scan, the surface was modelled and therefore known. In the phantom experiments, the surfaces were positioned close to the transducer and set to be parallel to the scanning x–y plane. This was done by taking PE-US B-scans along x for several positions of y, and setting the distance from the transducer to the surface of the agar to be constant.

10.3.3 Biological Scan

In the third test, the algorithm was applied to a data acquired from an ex-vivo juvenile zebra fish (35 days post fertilisation) mounted in clear agar. This model organism is a common subject in optoacoustic imaging studies [19] and was selected here because of high degree of scattering across its volume. The HFOAM system was operated in this case in the fast-scanning mode (applying no averaging) and used the photonic crystal fibre (PCF) and GRIN lens assembly. PE-US scans were also made, with a region of interest of 3x12 mm, of which a 1.6x6.1 mm sub-region was optoacoustically scanned. Both volumes were scanned with an x–y pixel-size of 10 μm without applying signal averaging; the optoacoustic scan was made with a per-pulse laser energy of around 15 μJ.

A map of the optically scattering surface $S(x, y)$ was determined semi-automatically. This value was then used to look-up the depth of the scattering surface for any x–y position of the scanning transducer, and thus the beam-waist of the un-scattered beam. As per the theory section, the scattered beam-waist was iteratively estimated as an embedded Gaussian beam, thus giving an estimate of the fluence distribution inside the imaged fish.

10.4 Results

10.4.1 Numerical Simulations

The results of applying W-SAFT to the simulated data are presented in Fig. 10.3 (iv), demonstrating significant improvement in the out of focus lateral resolution in the AR regime ($z' > -0.5$), whilst retaining optically dictated lateral resolution in the OR regime ($z' < -0.5$). This can be seen both qualitatively from the MAP images in panels B and C, and quantitatively from the full-width half-maximum annotations in C. The typical individual optoacoustic waveforms in **D** can be seen in Fig. 10.3D. Here a composite time-domain signal shows how in the OR regime the central signal for a sphere will still have temporally-distinct peak amplitudes even after the W-SAFT processing, due to the limited-contribution effects mentioned previously. Furthermore, with the three major distortion corrections and the fluence-attenuation compensation gain, the difference in normalised amplitude between the highest- and lowest-amplitude peak is 0.56 (iv). This is in contrast to the results of modified SIR-SAFT (ii), where the optically resolved data is laterally blurred and the normalised peak-peak amplitude range is 0.99 (see Fig.3 D). The importance of including all the distortion corrections is also clear when comparing the complete W-SAFT algorithm

(iv) to the intermediate result (iii) where only the limit function, Γ (10.10), was used.

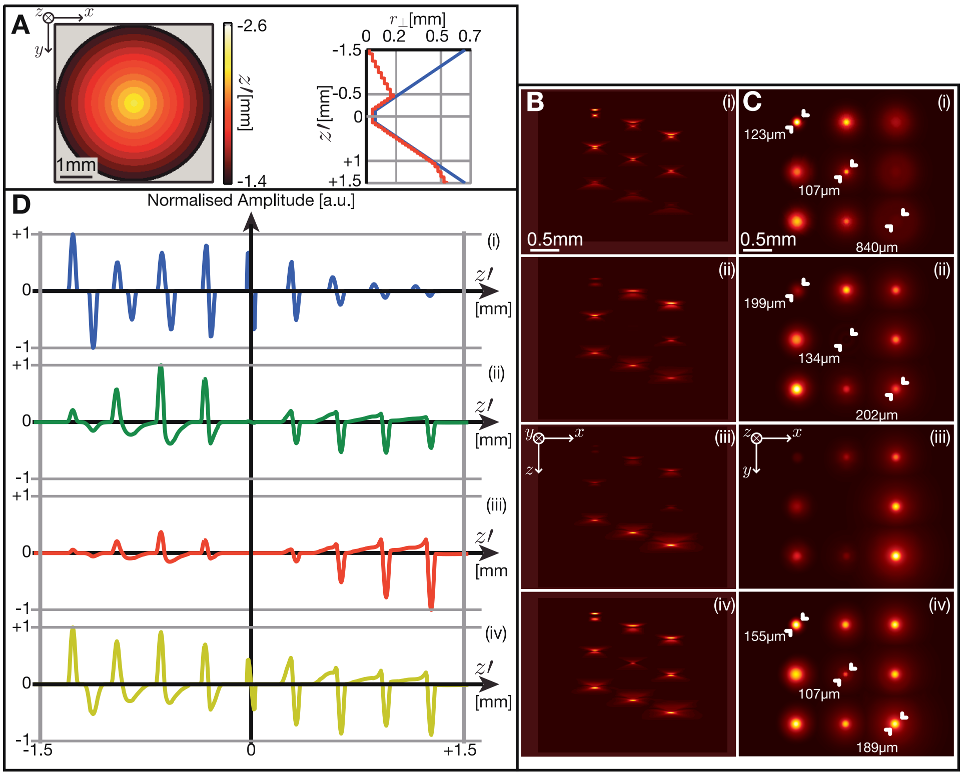

Figure 10.3: (A) left: Depth profile of the optically-scattering surface $S(x, y)$, where grey is no-surface, right: the limits of $\gamma(r_\perp, \theta)$ (red) and $\psi(r_\perp, \theta)$ (blue) evaluated at z'. (B) MAPs through y and (C) MAPS through z, where (i) is the simulated data, $\boldsymbol{D}$, (ii) the results of modified SIR-SAFT, (iii) the intermediate result of W-SAFT using only limit function Γ (10.10) and (iv) the complete result of W-SAFT with all distortion corrections, $\boldsymbol{V}$ (10.10). (C) also shows annotations of FWHM for 3 of the spheres. (D) shows the composite time-domain centre shots for (i-iv) i.e. superpositions of the time-domain signals for the centre of each sphere.

10.4.2 Phantom Scan

The performance of our method is further confirmed in the experimental results using the agar-suture phantom, as can be seen from Fig. 10.4. The out-of-focus lateral resolution in AR data (panel A) is improved, the lateral resolution in OR data (panel B) is maintained below a 19% mean decrease and in both cases a high degree of peak-peak amplitude compression is achieved. In the AR case, the advantages of W-SAFT are even more

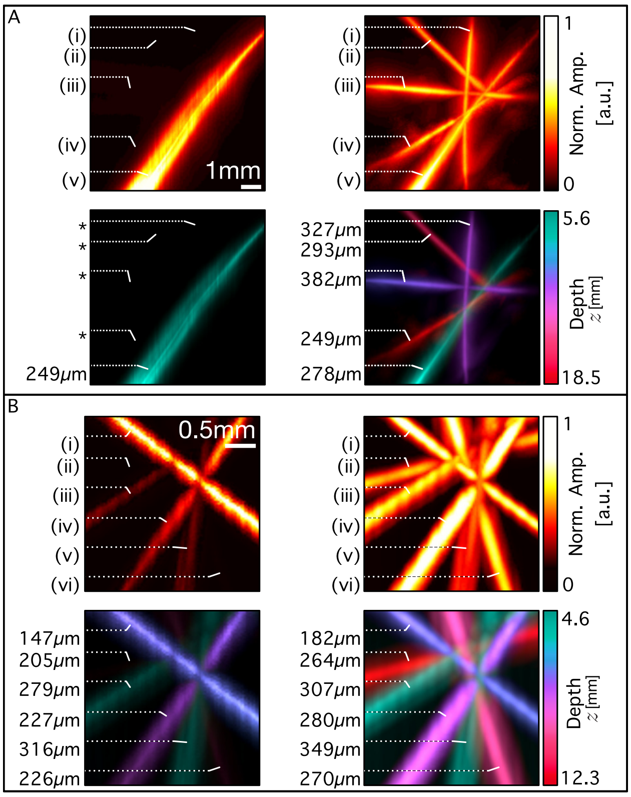

Figure 10.4: MAPs for experimental AR data (A) and OR data (B). In both A and B the left column is the unprocessed scan volume and the right column is the W-SAFT result; the top row are conventional MAPs in depth, z, and the bottom row are the same MAPs with a depth-coded colour scale. The top row is annotated with suture numbers, and in the bottom row each suture is annotated with a measure of FWHM.

obvious. In the unprocessed data (left column) only suture (v) is readily distinguishable, due to it's proximity to the acoustic focus. Conversely, in the processed data (right column) sutures (i-iv) are also clearly visible both with respect to their lateral resolution and the very small difference in amplitudes.

10.4.3 Zebrafish Imaging

Ex-vivo juvenile zebrafish imaging results are presented in Fig. 10.5, including the pulse-echo whole-body scan, the original optoacoustic scans, and the results of applying the W-SAFT method to the optoacoustic data. Panel (A) shows the MAP images of the pulse-echo ultrasound data (grey), the mask for the optically scattering surface (colour), and three regions through which partial-volume MAPs were made (dashed boxes).

Panel (B) presents said small-volume MAPs (a-c) through (1) the signal volume, (2) the W-SAFT result, (3) the W-SAFT result with annotations of key anatomical features, and (4) the annotated pulse-echo ultrasound signal volume.

Visualisation of volumetric signal-dense data presented some additional challenges. Here, MAPs of sub-volumes (thin layers) were chosen, as they effectively present sections of 3D structures. It should be noted that in order to improve legibility histogram-based noise-floor removal was performed for all data presented i.e. histograms with log-spaced bins were made for all volumes, and a threshold set at the maxima; voxels with an amplitude below the bin-value for the maxima were set to 0. This is possible because overwhelmingly more voxels for each volume lie outside the imaged specimen and thus mainly contain noise.

It can be clearly seen how W-SAFT affects the image quality. For instance, in all three of the subvolumes (10.5B.a-c), the MAPs for the unprocessed data volumes (10.5B.a-c.1) are largely shell-like i.e. only voxels from the periphery of the fish are visible, before the incident beam is scattered and attenuated. In contrast, in the W-SAFT results (10.5B.a-c.2-3) the volumes are more complete i.e. the signal amplitudes are more evenly distributed across the entire fish volume. Here the added value of optoacoustic over ultrasound is also evident, as although the pulse-echo ultrasound images are very useful in orientation of the target (top), the small subvolumes in (d) show very few features due to the lack of acoustic contrast. In the head subvolume (10.5B.a), the W-SAFT result (10.5B.a.3) gives a coronal cross section of the eyes and the brain, outlined in yellow and magenta, respectively. The brain section shows the telencephalon (cyan), and the front of the optic tectum (green). Although the eyes are present in the unprocessed data (10.5B.a.1), the brain is only visible in the W-SAFT processed volume (10.5B.a.2-3). In the torso subvolume (10.5B.b), the W-SAFT processing further reveals anatomical features located just behind the pronephros and above the anterior swim bladder, which could not be clearly identified from the atlas (peach). This unidentified structure is not easily seen in the signal volume (10.5B.b.1), whereas it is readily observed in the W-SAFT result (10.5B.b.2-3). In the anterior subvolume (10.5B.c), the W-SAFT result reveals the upper-left portion of the pronephros (orange), and a major vessel inside the liver (blue). These anatomical features were identified and labeled based on a qualitative comparison of the reconstructed optoacoustic volumes with the optical projection tomography (OPT) atlas [77].

10.5 Discussion

The first effort trialled here at retaining optically dominated resolution in HFOAM data was a modification of the previously published SIR-SAFT

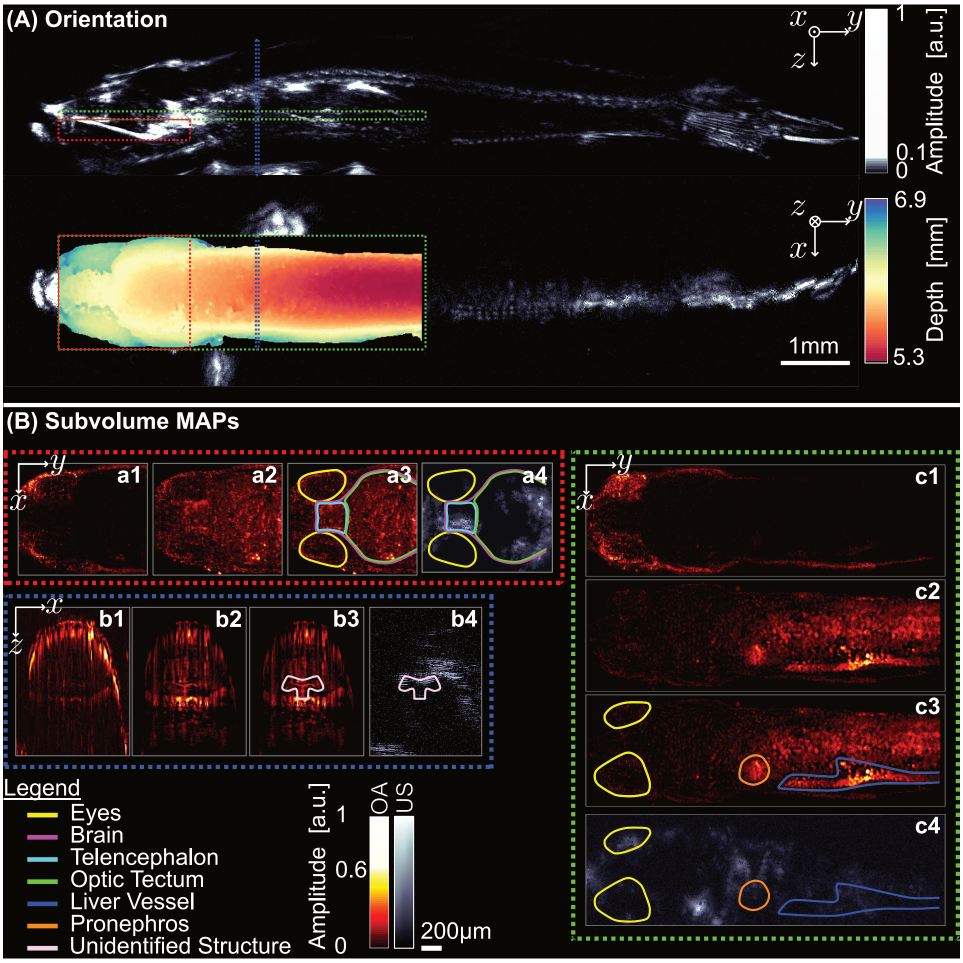
(A) Orientation
x y z
1
0.1
0
Amplitude [a.u.]
z y x
6.9
5.3
Depth [mm]
1mm
(B) Subvolume MAPs
a1
a2
a3
a4
b1
b2
b3
b4
c1
c2
c3
c4
Legend
Eyes
Brain
Telencephalon
Optic Tectum
Liver Vessel
Pronephros
Unidentified Structure
Amplitude [a.u.]
1
0.6
0
OA
US
200μm

Figure 10.5: (A): MAPs through signal volumes of ultrasound data x (above) and z (below); the surface depth mask is overlaid on the z-projection. The boundaries of three subvolumes (a-c) are shown as red, green and blue boxes respectively. MAPs of these subvolumes were made for the optoacoustic data, and are presented in (B). For each subvolume (a-c), MAPs are shown for (1) the signal volume, (2) the W-SAFT result, (3) the annotated W-SAFT result, and (4) the pulse-echo ultrasound signal volume, also annotated.

algorithm [67], where the weighting field employed was updated from the SIR alone to the include fluence-based spatial masking as per 10.14 . This was shown to be unsuccessful, thus illustrating the necessity of W-SAFT.

To form meaningful images of the OR data in Fig. 10.4, the volume was be first polarity-flipped in z about the acoustic focus, and then only one polarity of the volume used e.g. all negative values $\rightarrow 0$. This is necessary because the result of the W-SAFT method is still a bipolar ultrasound data set. Although one option here is to take MAPs of the absolute value of the Hilbert transform of the volume, there is no gain to be had. This is because where there are limited-contributions, namely in the OR-regime, the positive and negative peaks remain temporally discrete, and thus the Hilbert transform of the W-SAFT corrected result has two maxima. So although it would have been possible for the AR case, the one-sided volumes are presented for continuity. The polarity-flip about $z' = 0$ is necessary because in these data sets signals from beneath the focus will exhibit a negative-polarity bias, whereas those shallow of the focus exhibit a positive amplitude bias (see for example Fig. 10.3D).

One observation that must also be made for the AR phantom data (Fig. 10.4A) is that the 50 μm sutures appear to have a FWHM of around 300 μm in the W-SAFT output. This is because the system is detecting tilted cylindrical waves with a spherical surface, which results in significant low-pass filtering effects, which are detrimental to the frequency-dependent lateral resolution of the system. In the OR case in Fig. 10.4B, it can be observed that the amplitude correction is of significant advantage as all sutures are visible within a very close amplitude range. With respect to the lateral resolution, it can be observed that W-SAFT has little distorting effect (recall pixel dimension of 30 μm^2). One may still wonder as to why W-SAFT does not improve lateral resolution in the OR-regime. This is best explained by observations made in the AR-data where it was shown that, given all-possible lateral contributions, a suture phantom of this nature was only resolvable to a resolution of around 300 μm. As a result, the limited-contribution case of the OR data cannot be expected to outperform the broad-contribution AR case involving summation over large number of scanning positions. Indeed, the FWHM measures of the sutures in volumes A can be seen to, on average, be less than 300 μm. Thus, W-SAFT is performing exactly as desired with respect to its lateral resolution performance.

The brighter posterior region of the fish subvolume in Fig. 10.5B.c.2-3 is due to the presence of a region of low acoustic impedance, which acts as a partially-reflective plane. The presence of this region was confirmed from the pulse-echo ultrasound data presented in 10.5B.c.4. Namely, acoustic waves from optoacoustic sources very-close to (or at) this boundary, due to the immediate acoustic mismatch, undergo a more one-sided propagation e.g. hemispherical rather than spherical. This results in a considerably higher net signal amplitude detected for this region of the fish.

10.6 Conclusions

Data acquired from typical scanning optoacoustic microscopy systems is strongly affected by both the spatially varying sensitivity field of the detector and highly inhomogeneous light distribution across the imaged volume. Accurate image reconstruction thus implies accounting for both effects, which has been efficiently implemented here by means of the newly developed weighted synthetic aperture focusing technique, the W-SAFT. This lightweight and fast algorithm was showcased to simultaneously retain optical resolution characteristics at superficial tissue depths, improve the acoustic resolution performance whilst also compressing peak amplitudes to a tight dynamic range, without loss of context. Furthermore, W-SAFT has been shown to work on simulated data, phantom data, and ex-vivo biological data, and is the first optoacoustic algorithm to be applied successfully that accounts for moving, highly variant optical fluence. Future work may focus on further improvements through inclusion of a more dexterous scattered-beam model, making use of structural information from ultrasound data.

Part IV

Discussions and Future Directions

Developments Towards
High-Resolution Optoacoustic
In-Vivo Neuroimaging at Depth

Chapter 11

Future Work

11.1 Illumination - Fluence and the Limits of Single-path Optical Delivery

As reported here, the system developed largely aimed to achieve OR-OAM in the superficial regime, and AR-OAM in the scattered regime. The largest difficulty faced therein, is the trade off between optical fluence at great depths, and the per-pulse intensity at the optical focus. Due to the depth dependant attenuation of the illumination fluence in a scattering body, the intensity of the illumination at the surface required to sufficiently excite optoacoustic sources at depth can become too high and damage the target. Although at the acoustic focus AR-OAM is reasonably sensitive, for OA-SAFT to successfully restore signals from out-of-focus sources, said sources need to be sufficiently excited so as to generate detectable acoustic waves. That is not to say said waves need to be above the electrical noise floor when initially detected, but a lower limit does exist. This optimisation problem is exacerbated by the use of an optical focus as the sole delivery mechanism of illumination. Namely, because focusing illumination of a previously non-damaging level into a 20 μm spot greatly increases the heating efficiency at that spot.

The avenue of future work in this regard, which has already begun, should investigate a combined illumination delivery mechanism, whereby at and near to the scattering surface of the imaging target a small-diameter higher-energy spot provides OR data, whilst simultaneously delivering a powerful yet broad illumination for AR data acquisition. Such a development sadly cannot simply be a sequential firing system, due to the nature of the fast-scanning laser head i.e. the OR and AR signals would not fall at the same position for each acquisition.

A second important avenue of investigation also already underway is the implementation of multispectral illumination. Frequently used in optoacoustic tomography, illumination with many different wavelengths permits a distinction between chemical compounds in the optoacoustic data. With multispectral illumination and the subsequent spectral unmixing, another dimension of information is gained from a scan. For instance, multispectral HFOAM may be used to investigate the oxygenation of the brain under haemodynamic stress through localisation of oxygenated and deoxygenated haemoglobin.

11.2 Skull Correction - Approaches to Overcome a Significant Obstruction

As has been shown, the effects of the skull on optoacoustic data are significant. Although some groups have presented work apparently overcoming this barrier, they all used very young mice with far thinner skulls. An interesting avenue of investigation would be to continue the work presented here in obtaining a modelling framework for skull transmission, with an overall objective of creating a compensation. Such a compensation could be considered a form of spatio-temporal filtering, which when applied to HFOAM scan data could mitigate significant numbers of said effects. The immediate work necessary in this respect, is the ability to model the phase response of the skull, and the ability to confirm the model with experimental data.

11.3 W-SAFT - Fewer Bulk Assumptions of Target Properties

As presented in this thesis W-SAFT is an irrefutably useful tool in the improvement of OAM data sets acquired by the system. However, in it's current form the imaging target is assumed homogeneous in many of it's properties; for instance, speed of sound, optical scattering and optical attenuation. Future work in developing this algorithm should focus on implementation of non-bulk imaging target properties, because the algorithm itself doesn't necessitate it. Through use of the PE-US mode of the system it is, for example, already possible to determine boundaries of regions within an imaging target of different speed of sound. Therefore, by replacing the current assumption of $z \simeq c_0 t$ with a spatially varying map of c, and therefore z, the probability of correct constructive interference by which OA-SAFT works could be increased.

As for the spatially varying optical properties, some are more readily approached than others. Namely, scattering is currently estimated through the use of an iterative processes and manual observation. This process could be increased slightly in terms of complexity, by rather than using one measure of improvement and applying that degree of scattering to the whole volume, instead allow for scattering estimation to vary spatially. However, full fluence estimation remains a poorly posed problem in the absence of a confirmation method, and as such analytical and partially-analytical methods of estimation are best avoided. For example, in the example case of a simple experiment intralipid may be used to give a known degree of scattering to a phantom, and then a Monte Carlo simulation performed to estimate fluence inside the phantom. However, the optical properties of intralipid vary so greatly (also in the literature) that after several days of simulating for the simplest imaginable case, the fluence model will have no resemblance to the fluence inside the phantom.

Acknowledgements

I would like to thank Prof. Dr. Daniel Razansky and Prof. Dr. Vasillis Ntziachristos for providing me with the opportunity to perform my doctoral studies at the Institute for Biological and Medical Imaging; the facilities and support network with which to undertake my research; and, the guidance, critiquing and instruction provided throughout my time at the institute. Gratitude is due in particular to Dr. Héctor Estrada for his part in vital discussions on key aspects of the thesis, to Dr Moritz Kneipp as a valued contemporary and his assistance in experimental work, and to Christian Lutzweiler for his critical thinking during algorithm development. Lastly, thank you to all my fellow researchers and colleagues with whom I had the pleasure to learn from and work with.

Funding for this thesis and the research conducted during my studies has been contributed to from the European Research Council under grant agreement ERC-2010-StG-260991, and the German-Israeli Foundation (GIF) for Scientific Research and Development.

Appendices

Appendix A

List of Publications

- **Jake Turner**, Héctor Estrada, Moritz Kneipp, and Daniel Razansky – "*Universal weighted synthetic aperture focusing technique (W-SAFT) for scanning optoacoustic microscopy*", published in Optica, Vol. 4, Number 7, Pages 770–778 (2017) [70].
- Héctor Estrada, Johannes Rebling, **Jake Turner** and Daniel Razansky – "*Broadband acoustic properties of a murine skull*", published in Physics in medicine and biology, Vol. 61, Number 5, Pages 1932 (2016) [29].
- Moritz Kneipp, **Jake Turner**, Héctor Estrada, Johannes Rebling, Shy Shoham, and Daniel Razansky – "*Effects of the murine skull in optoacoustic brain microscopy*", published in Journal of Biophotonics, Vol. 9, Number 1-2, Pages 117–123 (2016) [20].
- Héctor Estrada, Johannes Rebling, **Jake Turner**, Moritz Kneipp, Shy Shoham, and Daniel Razansky – "*Estimation of the skull insertion loss using an optoacoustic point source*", published in SPIE BiOS, Pages 97080M–97080M (2016) [78].
- Moritz Kneipp, Héctor Estrada, Antonella Lauri, **Jake Turner**, Vasilis Ntziachristos, Gil G Westmeyer, and Daniel Razansky – "*Volumetric tracking of migratory melanophores during zebrafish development by optoacoustic microscopy*", published in Mechanisms of development (2015) [19].
- **Jake Turner**, Héctor Estrada, Moritz Kneipp, and Daniel Razansky – "*Improved optoacoustic microscopy through three-dimensional spatial impulse response synthetic aperture focusing technique*", published in Optics letters, Vol. 39, Number 12, Pages 3390–3393 (2014) [67].
- Moritz Kneipp*, **Jake Turner***, Sebastian Hambauer, Sandro M Krieg, Jens Lehmberg, Ute Lindauer, and Daniel Razansky – "*Functional*

real-time optoacoustic imaging of middle cerebral artery occlusion in mice", published in PloS one, Vol. 9, Number 4, Pages e96118 (2014) [79].

- Héctor Estrada, **Jake Turner**, Moritz Kneipp, and Daniel Razansky – "*Real-time optoacoustic brain microscopy with hybrid optical and acoustic resolution*", published in Laser Physics Letters, Vol. 11, Number 4, Pages 045601 (2014)[14].
- Luís X. Deán-Ben, Hector Estrada, Moritz Kneipp, **Jake Turner**, and Daniel Razansky – "*Three-dimensional modeling of the transducer shape in acoustic resolution optoacoustic microscopy*", published in SPIE BiOS, Pages 89434V–89434V (2014)[73].

List of Figures

1.1 Illustration of an incident wave, p_0 on a finite-width region with a different acoustic impedance. The five interface interactions are illustrated at time points t_0-t_4. 5

1.2 A qualitative illustration of (a) a plane wave incident on a circular speed of sound inhomogeneity and the resultant (b) transmission and (c) reflection. 6

3.1 The geometry for a raster scanning acquisition locus. 15

3.2 An ilustration of the 25 MHz piezo electric transducer and optical fibre assembly. 16

3.3 A schematic of the raster scanning optoacoustic microscope. VTS is the coarse large-range manual vertical position stage. The trigger signals from the oscilloscope (OSC - red) fired both the pump laser and started the data acquisition card on the PC. The $x-$, $y-$ and $z-$stages (red, yellow, pink) were controlled from inside the scanning routine on the PC. Detected ultrasound signals were passed to the PC via a preamplifier (purple). Water was necessary as the transducers are water-coupled. The inset figure shows how the field of view (FOV) of the transducer (purple) and a the excitation light emitted by, in this illustration, a photonic crystal fibre (PCF). 18

3.4 A: The 25 MHz piezoelectric transducer, with central 900 μm hole clearly visible; B: the custom plastic mount. 19

3.5 A: The electrical impulse response (EIR) of the 25 MHz piezoelectric detector, as measured with a 10 μm microsphere; B: the frequency response function (FRF) of the detector, as determined from the EIR, where red is the amplitude response and black is the phase. 20

3.6 The modelled spatial impulse response for the 25 MHz piezoelectric detector. 21

3.7 The PVDF transducer. 21

3.8 A: The electrical impulse response (EIR) of the PVDF detector, as measured from a 10 μm microsphere; B: the frequency response function (FRF) of the detector, as determined from the EIR, where red is the amplitude response and black is the phase. 22

3.9 The modelled spatial impulse response for the PVDF transducer. 22

3.10 A photograph of the output-tip of the photonic crystal fibre. 24

3.11 An illustration of how the radially varying refractive index, R, of a GRIN lens focuses light, where r and z are radius and depth, respectively. 24

3.12 A diagram of the combined PCF and GRIN lens assembly; SCD, OCD and CD are the single-core, outer-core, and coating core diameters, respectively. 25

3.13 A diagram of the hierarchy of the code and the order of commands to perform a raster scan. 26

3.14 Central slices for A: an AR data set of a 20 μm microsphere raster scan and B: the WSAFT result for the scan. 28

3.15 Maximum amplitude projections in z for an OR raster scan of a 50 μm suture, with **A**: a colourmap for amplitude and **B**: a colourmap for depth. 29

3.16 Maximum amplitude images in depth, z, for a series of raster scans performed to locate a 30 μm microsphere at the tip of a 20 μm diameter suture. Scans were performed over smaller regions and at higher resolution iteratively from A through D. 30

4.1 The locus for the fast-scanning regime. The linear stage scans slowly in the y-direction while the piezo stage scans rapidly in the x-direction; both stages are under constant motion during a scan. 34

4.2 A schematic of the fast scanning optoacoustic microscope. VTS is the coarse large-range manual vertical position stage. The trigger signals from the oscilloscope (OSC - red) fired both the pump laser and started the data acquisition cards on the PC. The $x-$, $y-$ and $z-$stages (red, yellow, pink) were controlled from inside the scanning routine on the PC; the signal from the laser distance sensor (brown - LDS) was used to calibrate the x-stage motion. Detected ultrasound signals were passed to the PC via a preamplifier (purple). Water was necessary as the transducers are water-coupled. The inset figure shows how the field of view (FOV) of the transducer (purple) and a the excitation light emitted by, in this illustration, a photonic crystal fibre (PCF). 36

4.3 An example laser power distribution for one scan. The red and green lines indicate the lower and upper thresholds as defined by the user. 37

4.4 An optical resolution optoacoustic microscopy image of a mouse ear (4.5x4.5 mm), with acquisitions used while the transducer-laser assembly moved from (a) left-to-right only, (b) right-to-left only, and (c) in both directions. 39

4.5 A: An optical resolution optoacoustic microscopy image of a mouse ear (4.5x4.5 mm), with acquisitions used while the transducer-laser assembly moved in both directions and fibre drift was corrected for via a cross-correlation algorithm; B: cross-correlation against lag τ at each y-position. 39

4.6 Time-domain optoacoustic signals from the previously presented mouse ear data. The optoacoustic signal from the one-way volume (blue) is annotated with an SNR of 27 dB, and the signal from the two-way volume (red) with an SNR of 28 dB. 40

4.7 Maximum amplitude images of mouse brain through a hole in the skull; (A) colour-coded for amplitude, (B) colour-coded for depth. 41

4.8 Maximum amplitude images of an *ex-vivo* juvenille zebrafish; (A) colour-coded for amplitude, (B) colour-coded for depth. . 41

5.1 A schematic of the ultrasound and optoacoustic scanning microscope. VTS is the coarse large-range manual vertical position stage. The trigger signals from the oscilloscope (OSC - red) fired both the pump laser and started the data acquisition cards on the PC. The $x-$, $y-$ and $z-$ stages (red, yellow, pink) were controlled from inside the scanning routine on the PC; the signal from the laser distance sensor (brown - LDS) was used to calibrate the x-stage motion. Detected ultrasound signals were passed to the PC via the ultrasound pulser (USP - purple); the pulser was also used to generate ultrasound waves from the transducer. Water was necessary as the transducers are water-coupled. The inset figure shows how the field of view (FOV) of the transducer (purple) and a the excitation light emitted by, in this illustration, a photonic crystal fibre (PCF). 46

5.2 Maximum amplitude projections for a pulse-echo ultrasound image of a mouse skull; projections through (A) z, (B) x and (C) z. Annotations are of (i) a hair (ii) the bregma, and (iii) the transparent foil. 48

5.3 Maximum intensity projections for a pulse-echo ultrasound image of a mouse skull; projections through (A) z, (B) x and (C) z. Annotations retain the convention of Figure 5.2, and are of (ii) the bregma, (iii) the transparent foil and (iV) the hole. 48

5.4 Maximum intensity projections for a pulse-echo ultrasound image of a mouse ear; projections through (A) z, (B) x and (C) y. 49

5.5 The top-down maximum amplitude projections for an OAM image and a PE-US image of a mouse ear overlaid. 50

5.6 MAPs of scanning a juvenile zebrafish with (top) the PE-US mode of the system and (bottom) the OR-OAM mode. The green rectangle illustrates the subvolume for which the OAM data is overlaid. 50

6.1 Schematics of the experimental approaches. (a) AR-OAM configuration using broad illumination. Optoacoustic sources located just above the skull generate ringing artifacts and shadow signals due to reflections at the skull surfaces (vertical line in the blue box denotes temporal position of the skull). Acoustic dispersion of the skull creates frequency dependent attenuation with higher frequency signals (generated by smaller objects) experiencing stronger attenuation compared to lower frequency content (generated by larger objects), see green box. (b) OR-OAM configuration using focused illumination. Focused light is scattered by the skull, broadening the excitation beam and affecting the lateral resolution performance. 56

6.2 Results of the microsphere experiments demonstrate acoustic dispersion and ringing effects of adult murine skull. (a) Normalised US frequency spectrum of the signal of a single 10 μm microsphere excited with a nanosecond laser pulse and measured with a ultrawideband PVdF transducer. (b) Optoacoustic signal traces generated in the presence and absence of the skull. The attenuated peak is lower in amplitude and broader when compared to the non-attenuated peak (marked by arrows). The signal shift is labeled Δt. (c) Simulated (black) and measured (red) frequency dependent attenuation (insertion loss) of the skull showing a strong increase with frequency. (d) Time domain signal of a microsphere placed in the immediate vicinity of the skull surface clearly shows signal ringing due to reflections at the skull-tissue interface. . 58

6.3 Effects of acoustic attenuation on imaging performance in the AR mode. (a) Three-dimensional optoacoustic image (color-coded for depth) of four absorbing sutures arbitrarily arranged inside tissue-mimicking scattering agar phantom. (b) The corresponding image acquired in the presence of skull. Scale bars correspond to 1.5 mm. Yellow arrows mark irregularities in the skull measurements. White arrows mark the position of FWHM measurements: 365 μm, 261 μm, 210 μm and 402 μm, 308 μm, 236 μm in (a) and (b) respectively. . . 60

6.4 Murine skull affects the effective lateral resolution performance in OR-OAM scans of biological targets. MAPs of OR images of the perfused brain recorded through an intact skull (a), thinned skull (c) and without presence of the skull (b). Dashed lines mark the area where the skull was thinned (c) or removed (b). (b) and (c) each show one hemisphere (LH: left hemisphere, RH: right hemisphere) of the whole brain depicted in (a). A two-dimensional slice of AR data of a perfused brain through the intact skull (e) and with the skull removed (f). Arrows in (f) denote the positions of FWHM measurements. A photograph of an excised mouse brain, perfused with a mixture of agarose and ink, is shown in (d). Scale bars are 375 μm. 61

7.1 Geometry of the proposed method for the measurement of the skull insertion loss. The space is divided into three regions. Broadband ultrasound waves generated by an optoacoustic point source impinge at the skull of thickness h and surface normal vector $\hat{\mathbf{n}}$. The transmitted wave reaches the detector's surface S. The acceptance solid angle of the spherically focused detector is indicated by dashed lines. 65

7.2 Diagram of the plane wave model of a fluid-loaded solid layer. ϕ_{1+} is the incident wave and ϕ_3 the transmitted wave. 66

7.3 Insertion loss as a function of the frequency (a) and transmission $|T(k_{||}, \omega)|^2$ dispersion calculated from the estimated parameters (b) for the glass cover-slip. The grey region surrounding the measured mean IL in (a) is limited by the minimum and maximum measured values. 70

7.4 Ultrasound images of mouse skull 1 in focus. (a) and (b) show maximum amplitude projections from the top whereas lateral panels depict cross sections taken at the positions of the dashed lines. The portion of the skull which falls inside of the transducer's acceptance cone is indicated by a circle. Blue lines indicate the position of the fitted plane. The inset in (a) shows a full mouse skull and the shadowed area represents the fragment used in the experiments. 71
7.5 Insertion loss as a function of the frequency (a), (c) and transmission $|T(k_{||},\omega)|^2$ dispersion (b), (d) calculated from the estimated parameters for two mouse skulls. The gray region surrounding the measured mean IL in (a), (c) is limited by the minimum and maximum measured values. 72
7.6 Transmission $|T(k_{||},\omega)|^2$ dispersion calculated from the estimated parameters of skull 1 assuming a fluid (a) and a solid (b) homogeneous layer. 75

8.1 How the arrival times for the wavefront of an out-of-focus acoustic source are spread compared to those of an in focus source. 79
8.2 An illustration of how delaying the arrivals of a spherical wave $P_0(t)$ to approximate a plane wave $P_0'(t)$ 80

9.1 A schematic of 5 acoustic sources at different depths from the focus, F, of the ultrasound detector, with lines of equal-delay marked for each source. Two detector positions, (x_0, y_0) and (x_n, y_0), are shown; position (x_n, y_0) has the acoustic sensitivity field of the detector overlaid. 82
9.2 A superposition image of the sinograms for simulations of 30 μm spheres at different depths, where 13 of 41 spheres are shown (a); and, (b-e) a superposition of the results of applying SAFT, SIRSAFT, CFSAFT, and CFSIRSAFT. The superposition of the acoustic signals at $x = 0$ is shown below as (f-h) sinogram, SAFT, and SIRSAFT. 84
9.3 The lateral FWHM (top) and the axial SNR (bottom) for all 41 simulated microspheres at many depths, as per Figure 9.2. 85
9.4 A volume rendering of experimental optoacoustic microscopy data of a loosely-knotted 30 μm suture, where (a) is the sinogram, and (b) is the results of CF-SAFT processing, and (c) is the results of CF-SIR-SAFT processing. 86
9.5 Maximum amplitude images with annotated measures of FWHM for a 30 μm suture orientated obliquely to the focal plane after different SAFT-based processing; a photograph of the suture phantom is annotated with the approximate ROI. 87

10.1 Illustrations of the extents of the axially symmetric fields of light fluence (blue) and ultrasound-transducer field-of-view (red) as functions of depth z and polar-radius (radius to the focal axis) $r_\perp$. (a) The acoustic resolution (AR) case with broad illumination and focused detection, (b) The optical resolution (OR) case with a focused illumination, (c) Hybrid resolution optoacoustic microscopy (HFOAM) uses both focused illumination and detection. An illustration of the 3D-SAFT operation in spherical coordinates is shown in (d). 92

10.2 A schematic illustration of the process of implementing W-SAFT. Each row of the figure corresponds to one line in (10.10). 96

10.3 (A) left: Depth profile of the optically-scattering surface $S(x, y)$, where grey is no-surface, right: the limits of $\gamma(r_\perp, \theta)$ (red) and $\psi(r_\perp, \theta)$ (blue) evaluated at z'. (B) MAPs through y and (C) MAPS through z, where (i) is the simulated data, $\boldsymbol{D}$, (ii) the results of modified SIR-SAFT, (iii) the intermediate result of W-SAFT using only limit function Γ (10.10) and (iv) the complete result of W-SAFT with all distortion corrections, $\boldsymbol{V}$ (10.10). (C) also shows annotations of FWHM for 3 of the spheres. (D) shows the composite time-domain centre shots for (i-iv) i.e. superpositions of the time-domain signals for the centre of each sphere. 100

10.4 MAPs for experimental AR data (A) and OR data (B). In both A and B the left column is the unprocessed scan volume and the right column is the W-SAFT result; the top row are conventional MAPs in depth, z, and the bottom row are the same MAPs with a depth-coded colour scale. The top row is annotated with suture numbers, and in the bottom row each suture is annotated with a measure of FWHM. 101

10.5 (A): MAPs through signal volumes of ultrasound data x (above) and z (below); the surface depth mask is overlaid on the z-projection. The boundaries of three subvolumes (a-c) are shown as red, green and blue boxes respectively. MAPs of these subvolumes were made for the optoacoustic data, and are presented in (B). For each subvolume (a-c), MAPs are shown for (1) the signal volume, (2) the W-SAFT result, (3) the annotated W-SAFT result, and (4) the pulse-echo ultrasound signal volume, also annotated. 103

List of Tables

7.1 Estimated parameters for the glass plate compared to [49]. . . 70
7.2 Estimated parameters for two mouse skulls 73

9.1 Qualitative measures of resolution and SNR performance for SAFT, SIR-SAFT, CF-SAFT, and CF-SIR-SAFT. The values are for sources 3 mm shallow of the focus, the focus (bold), and 3 mm deeper than the focus. Asterisks denote affected values. 86

Bibliography

[1] J. Schneider, J. Zahn, M. Maglione, S. J. Sigrist, J. Marquard, J. Chojnacki, H.-G. Krausslich, S. J. Sahl, J. Engelhardt, and S. W. Hell, "Ultrafast, temporally stochastic sted nanoscopy of millisecond dynamics," *Nat Meth*, vol. 12, pp. 827–830, 09 2015.

[2] D. S. Cohen and G. H. Handelman, "Scattering of a plane acoustical wave by a spherical obstacle," *The Journal of the Acoustical Society of America*, vol. 38, no. 5, pp. 827–834, 1965.

[3] M. A. A. Caballero, A. Rosenthal, A. Buehler, D. Razansky, and V. Ntziachristos, "Optoacoustic determination of spatio- temporal responses of ultrasound sensors," *IEEE Transactions on Ultrasonics, Ferroelectrics and Frequency Control*, vol. 60, no. 6, 2013.

[4] L. Cutrona, "Synthetic aperture radar," *Radar Handbook, second edition, ed. M. Skolnik, McGraw-Hill, New York*, 1990.

[5] A. Rosenthal, D. Razansky, and V. Ntziachristos, "Fast semi-analytical model-based acoustic inversion for quantitative optoacoustic tomography," *Medical Imaging, IEEE Transactions on*, vol. 29, no. 6, pp. 1275–1285, 2010.

[6] L. V. Wang, "Tutorial on photoacoustic microscopy and computed tomography," *Selected Topics in Quantum Electronics, IEEE Journal of*, vol. 14, no. 1, pp. 171–179, 2008.

[7] L. V. Wang and S. Hu, "Photoacoustic tomography: in vivo imaging from organelles to organs," *Science*, vol. 335, no. 6075, pp. 1458–1462, 2012.

[8] V. Ntziachristos and D. Razansky, "Revolutionizing biopharmaceutical development with quantitative multispectral optoacoustic tomography (msot)," *Modern Biopharmaceuticals: Recent Success Stories*, pp. 211–232, 2013.

[9] A. Chekkoury, J. Gateau, W. Driessen, P. Symvoulidis, N. Bézière, A. Feuchtinger, A. Walch, and V. Ntziachristos, "Optical mesoscopy

without the scatter: broadband multispectral optoacoustic mesoscopy," *Biomedical optics express*, vol. 6, no. 9, pp. 3134–3148, 2015.

[10] Y. Zhou, W. Xing, K. I. Maslov, L. A. Cornelius, and L. V. Wang, "Handheld photoacoustic microscopy to detect melanoma depth in vivo," *Optics letters*, vol. 39, no. 16, pp. 4731–4734, 2014.

[11] X. L. Deán-Ben, T. F. Fehm, M. Gostic, and D. Razansky, "Volumetric hand-held optoacoustic angiography as a tool for real-time screening of dense breast," *Journal of biophotonics*, 2015.

[12] L. V. Wang, "Multiscale photoacoustic microscopy and computed tomography," *Nature photonics*, vol. 3, no. 9, pp. 503–509, 2009.

[13] R. Ma, S. Söntges, S. Shoham, V. Ntziachristos, and D. Razansky, "Fast scanning coaxial optoacoustic microscopy," *Biomedical optics express*, vol. 3, no. 7, p. 1724, 2012.

[14] H. Estrada, J. Turner, M. Kneipp, and D. Razansky, "Real-time optoacoustic brain microscopy with hybrid optical and acoustic resolution," *Laser Physics Letters*, vol. 11, no. 4, p. 045601, 2014.

[15] K. Maslov, H. F. Zhang, S. Hu, and L. V. Wang, "Optical-resolution photoacoustic microscopy for in vivo imaging of single capillaries," *Opt. Lett.*, vol. 33, pp. 929–931, May 2008.

[16] S.-L. Chen, Z. Xie, L. J. Guo, and X. Wang, "A fiber-optic system for dual-modality photoacoustic microscopy and confocal fluorescence microscopy using miniature components," *Photoacoustics*, vol. 1, no. 2, pp. 30 – 35, 2013.

[17] M. Schwarz, M. Omar, A. Buehler, J. Aguirre, and V. Ntziachristos, "Implications of ultrasound frequency in optoacoustic mesoscopy of the skin," *Medical Imaging, IEEE Transactions on*, vol. 34, no. 2, pp. 672–677, 2015.

[18] J. A. Jensen, "Field: A program for simulating ultrasound systems," in *10th Nordicbaltic Conference on Biomedical Imaging*, vol. 4, pp. 351–353, Citeseer, 1996.

[19] M. Kneipp, H. Estrada, A. Lauri, J. Turner, V. Ntziachristos, G. G. Westmeyer, and D. Razansky, "Volumetric tracking of migratory melanophores during zebrafish development by optoacoustic microscopy," *Mechanisms of development*, 2015.

[20] M. Kneipp, J. Turner, H. Estrada, J. Rebling, S. Shoham, and D. Razansky, "Effects of the murine skull in optoacoustic brain microscopy," *Journal of Biophotonics*, vol. 9, no. 1-2, pp. 117–123, 2016.

[21] J. Gamelin, A. Maurudis, A. Aguirre, F. Huang, P. Guo, L. V. Wang, and Q. Zhu, “A real-time photoacoustic tomography system for small animals,” *Optics express*, vol. 17, no. 13, pp. 10489–10498, 2009.

[22] C. Stosiek, O. Garaschuk, K. Holthoff, and A. Konnerth, “In vivo two-photon calcium imaging of neuronal networks,” *Proceedings of the National Academy of Sciences*, vol. 100, no. 12, pp. 7319–7324, 2003.

[23] S. Hu, K. Maslov, and L. V. Wang, “Second-generation optical-resolution photoacoustic microscopy with improved sensitivity and speed,” *Optics letters*, vol. 36, no. 7, pp. 1134–1136, 2011.

[24] K. H. Song and L. V. Wang, “Deep reflection-mode photoacoustic imaging of biological tissue,” *Journal of biomedical optics*, vol. 12, no. 6, pp. 060503–060503, 2007.

[25] X. Wang, D. L. Chamberland, and G. Xi, “Noninvasive reflection mode photoacoustic imaging through infant skull toward imaging of neonatal brains,” *Journal of neuroscience methods*, vol. 168, no. 2, pp. 412–421, 2008.

[26] E. W. Stein, K. Maslov, and L. V. Wang, “Noninvasive, in vivo imaging of the mouse brain using photoacoustic microscopy,” *Journal of applied physics*, vol. 105, no. 10, p. 102027, 2009.

[27] T. Jianbin, H. Liang, H. Jufang, W. Hui, C. Dan, Z. Leping, Z. Jin, and L. Xuegang, “Improved method of ink-gelatin perfusion for visualising rat retinal microvessels,” *Acta histochemica et cytochemica*, vol. 41, no. 5, pp. 127–133, 2008.

[28] V. Igor’A, *Rayleigh and Lamb waves: physical theory and applications.* Plenum Press, 1967.

[29] H. Estrada, J. Rebling, J. Turner, and D. Razansky, “Broadband acoustic properties of a murine skull,” *Physics in medicine and biology*, vol. 61, no. 5, p. 1932, 2016.

[30] D. Coluccia, J. Fandino, L. Schwyzer, R. O’Gorman, L. Remonda, J. Anon, E. Martin, and B. Werner, “First noninvasive thermal ablation of a brain tumor with mr-guided focused ultrasound,” *Journal of Therapeutic Ultrasound*, vol. 2, p. 17, 2014.

[31] M. Aryal, C. D. Arvanitis, P. M. Alexander, and N. McDannold, “Ultrasound-mediated blood-brain barrier disruption for targeted drug delivery in the central nervous system,” *Advanced Drug Delivery Reviews*, vol. 72, pp. 94 – 109, 2014. Ultrasound triggered drug delivery.

[32] Y. Tufail, A. Matyushov, N. Baldwin, M. L. Tauchmann, J. Georges, A. Yoshihiro, S. I. H. Tillery, and W. J. Tyler, “Transcranial pulsed ultrasound stimulates intact brain circuits,” *Neuron*, vol. 66, no. 5, pp. 681 – 694, 2010.

[33] J. Yao and L. V. Wang, “Photoacoustic brain imaging: from microscopic to macroscopic scales,” *Neurophotonics*, vol. 1, no. 1, p. 011003, 2014.

[34] M. A. L. Bell, A. K. Ostrowski, K. Li, P. Kazanzides, and E. M. Boctor, “Localization of transcranial targets for photoacoustic-guided endonasal surgeries,” *Photoacoustics*, vol. 3, no. 2, pp. 78 – 87, 2015.

[35] F. J. Fry and J. E. Barger, “Acoustical properties of the human skull,” *The Journal of the Acoustical Society of America*, vol. 63, no. 5, pp. 1576–1590, 1978.

[36] G. T. Clement and K. Hynynen, “A non-invasive method for focusing ultrasound through the human skull,” *Physics in Medicine and Biology*, vol. 47, no. 8, p. 1219, 2002.

[37] G. Clement and K. Hynynen, “Correlation of ultrasound phase with physical skull properties,” *Ultrasound in Medicine & Biology*, vol. 28, no. 5, pp. 617 – 624, 2002.

[38] F. Marquet, M. Pernot, J.-F. Aubry, G. Montaldo, L. Marsac, M. Tanter, and M. Fink, “Non-invasive transcranial ultrasound therapy based on a 3d ct scan: protocol validation and in vitro results,” *Physics in Medicine and Biology*, vol. 54, no. 9, p. 2597, 2009.

[39] G. Pinton, J.-F. Aubry, E. Bossy, M. Muller, M. Pernot, and M. Tanter, “Attenuation, scattering, and absorption of ultrasound in the skull bone,” *Medical Physics*, vol. 39, no. 1, pp. 299–307, 2012.

[40] G. T. Clement, P. J. White, and K. Hynynen, “Enhanced ultrasound transmission through the human skull using shear mode conversion,” *The Journal of the Acoustical Society of America*, vol. 115, no. 3, pp. 1356–1364, 2004.

[41] D. Fei, D. E. Chimenti, and S. V. Teles, “Material property estimation in thin plates using focused, synthetic-aperture acoustic beams,” *J. Acoust. Soc. Am.*, vol. 113, no. 5, pp. 2599–2610, 2003.

[42] A. Wydra, E. Malyarenko, K. Shapoori, and R. G. Maev, “Development of a practical ultrasonic approach for simultaneous measurement of the thickness and the sound speed in human skull bones: a laboratory phantom study,” *Physics in Medicine and Biology*, vol. 58, no. 4, p. 1083, 2013.

[43] S. Pichardo, V. W. Sin, and K. Hynynen, "Multi-frequency characterization of the speed of sound and attenuation coefficient for longitudinal transmission of freshly excised human skulls," *Physics in Medicine and Biology*, vol. 56, no. 1, p. 219, 2011.

[44] I. A. Viktorov, *Rayleigh and Lamb Waves.* Plenum Press, New York, 1967.

[45] J. Yao and L. V. Wang, "Sensitivity of photoacoustic microscopy," *Photoacoustics*, vol. 2, no. 2, pp. 87 – 101, 2014.

[46] J. Gateau, L. Marsac, M. Pernot, J.-F. Aubry, M. Tanter, and M. Fink, "Transcranial ultrasonic therapy based on time reversal of acoustically induced cavitation bubble signature," *Biomedical Engineering, IEEE Transactions on*, vol. 57, pp. 134–144, Jan 2010.

[47] L. M. Brekhovskikh and O. A. Godin, *Acoustics of Layered Media*, vol. II of *Springer Series on Wave Phenomena.* Springer-Verlag Berlin Heidelberg, 2nd ed., 1999.

[48] E. G. Williams, *Fourier Acoustics : sound radiation and nearfield acoustical holography.* Academic Press, 1999.

[49] T. Kundu, *Ultrasonic Nondestructive Evaluation.* CRC Press LLC, 2004.

[50] L. M. Brekhovskikh and O. A. Godin, *Acoustics of Layered Media*, vol. I of *Springer Series on Wave Phenomena.* Springer-Verlag Berlin Heidelberg New York, 2nd ed., 1998.

[51] G. J. Diebold and T. Sun, "Properties of photoacoustic waves in one, two, and three dimensions," *Acta Acustica united with Acustica*, vol. 80, no. 4, pp. 339–351, 1994.

[52] H. Estrada, P. Candelas, F. Belmar, A. Uris, F. J. García de Abajo, and F. Meseguer, "Engineering surface waves in flat phononic plates," *Phys. Rev. B*, vol. 85, p. 174301, May 2012.

[53] D. E. Goldberg, *Genetic Algorithms in Search, Optimization, and Machine Learning.* Addison-Wesley Publishing Company, Inc., 1989.

[54] Y. Kurihara, "Numerical integration of the primitive equations on a spherical grid," *Mon. Wea. Rev.*, vol. 93, pp. 399–415, July 1965.

[55] X. Zeng and R. J. McGough, "Evaluation of the angular spectrum approach for simulations of near-field pressures," *The Journal of the Acoustical Society of America*, vol. 123, no. 1, pp. 68–76, 2008.

[56] M. O. Culjat, D. Goldenberg, P. Tewari, and R. S. Singh, "A review of tissue substitutes for ultrasound imaging," *Ultrasound in Medicine & Biology*, vol. 36, no. 6, pp. 861 – 873, 2010.

[57] P. White, G. Clement, and K. Hynynen, "Longitudinal and shear mode ultrasound propagation in human skull bone," *Ultrasound in Medicine and Biology*, vol. 32, no. 7, pp. 1085–1096, 2006.

[58] J. J. Choi, M. Pernot, T. R. Brown, S. A. Small, and E. E. Konofagou *Physics in Medicine and Biology*, vol. 52, no. 18, p. 5509, 2007.

[59] M. Guizar-Sicairos and J. C. Gutiérrez-Vega, "Computation of quasi-discrete hankel transforms of integer order for propagating optical wave fields," *J. Opt. Soc. Am. A*, vol. 21, pp. 53–58, Jan 2004.

[60] A. W. Norfolk and E. J. Grace, "Reconstruction of optical fields with the quasi-discrete hankel transform," *Opt. Express*, vol. 18, pp. 10551–10556, May 2010.

[61] M. Hayner and K. Hynynen, "Numerical analysis of ultrasonic transmission and absorption of oblique plane waves through the human skull," *The Journal of the Acoustical Society of America*, vol. 110, no. 6, pp. 3319–3330, 2001.

[62] Z. E. A. Fellah, N. Sebaa, M. Fellah, F. Mitri, E. Ogam, W. Lauriks, and C. Depollier, "Application of the biot model to ultrasound in bone: Direct problem," *Ultrasonics, Ferroelectrics, and Frequency Control, IEEE Transactions on*, vol. 55, pp. 1508–1515, July 2008.

[63] C. Frazier and W. O'Brien, "Synthetic aperture techniques with a virtual source element," *Ultrasonics, Ferroelectrics and Frequency Control, IEEE Transactions on*, vol. 45, no. 1, pp. 196–207, 1998.

[64] M.-L. Li, W.-J. Guan, and P.-C. Li, "Improved synthetic aperture focusing technique with applications in high-frequency ultrasound imaging," *Ultrasonics, Ferroelectrics and Frequency Control, IEEE Transactions on*, vol. 51, no. 1, pp. 63–70, 2004.

[65] Z. Deng, X. Yang, H. Gong, and Q. Luo, "Adaptive synthetic-aperture focusing technique for microvasculature imaging using photoacoustic microscopy," *Opt. Express*, vol. 20, pp. 7555–7563, Mar 2012.

[66] M.-L. Li, H. F. Zhang, K. Maslov, G. Stoica, and L. V. Wang, "Improved in vivo photoacoustic microscopy based on a virtual-detector concept," *Opt. Lett.*, vol. 31, pp. 474–476, Feb 2006.

[67] J. Turner, H. Estrada, M. Kneipp, and D. Razansky, "Improved optoacoustic microscopy through three-dimensional spatial impulse response synthetic aperture focusing technique," *Optics letters*, vol. 39, no. 12, pp. 3390–3393, 2014.

[68] C. Nilsen and S. Holm, "Wiener beamforming and the coherence factor in ultrasound imaging," *Ultrasonics, Ferroelectrics and Frequency Control, IEEE Transactions on*, vol. 57, no. 6, pp. 1329–1346, 2010.

[69] M.-L. Li, H. F. Zhang, K. Maslov, G. Stoica, and L. V. Wang, "Virtual-detector synthetic aperture focusing technique with application in in vivo photoacoustic microscopy," *Proc. SPIE*, vol. 6086, pp. 60861F–60861F–8, 2006.

[70] J. Turner, H. Estrada, M. Kneipp, and D. Razansky, "Universal weighted synthetic aperture focusing technique (w-saft) for scanning optoacoustic microscopy," *Optica*, vol. 4, pp. 770–778, Jul 2017.

[71] E. M. Strohm, M. J. Moore, and M. C. Kolios, "High resolution ultrasound and photoacoustic imaging of single cells ‘," *Photoacoustics*, 2016.

[72] M. Ángel Araque Caballero, A. Rosenthal, J. Gateau, D. Razansky, and V. Ntziachristos, "Model-based optoacoustic imaging using focused detector scanning," *Opt. Lett.*, vol. 37, pp. 4080–4082, Oct 2012.

[73] X. L. Deán-Ben, H. Estrada, M. Kneipp, J. Turner, and D. Razansky, "Three-dimensional modeling of the transducer shape in acoustic resolution optoacoustic microscopy," in *SPIE BiOS*, pp. 89434V–89434V, International Society for Optics and Photonics, 2014.

[74] R. Cao, J. P. Kilroy, B. Ning, T. Wang, J. A. Hossack, and S. Hu, "Multispectral photoacoustic microscopy based on an optical–acoustic objective," *Photoacoustics*, vol. 3, no. 2, pp. 55–59, 2015.

[75] A. E. Siegman, "How to (maybe) measure laser beam quality," in *DPSS (Diode Pumped Solid State) Lasers: Applications and Issues*, p. MQ1, Optical Society of America, 1998.

[76] F. Träger, *Springer Handbook of Lasers and Optics*. Springer, 2012.

[77] D. Salgado, C. Marcelle, P. D. Currie, and R. J. Bryson-Richardson, "The zebrafish anatomy portal: A novel integrated resource to facilitate zebrafish research," *Developmental biology*, vol. 372, no. 1, pp. 1–4, 2012.

[78] H. Estrada, J. Rebling, J. Turner, M. Kneipp, S. Shoham, and D. Razansky, “Estimation of the skull insertion loss using an optoacoustic point source,” in *SPIE BiOS*, pp. 97080M–97080M, International Society for Optics and Photonics, 2016.

[79] M. Kneipp, J. Turner, S. Hambauer, S. M. Krieg, J. Lehmberg, U. Lindauer, and D. Razansky, “Functional real-time optoacoustic imaging of middle cerebral artery occlusion in mice,” *PloS one*, vol. 9, no. 4, p. e96118, 2014.